Chiral and Active Colloids

Universiteit Utrecht

Cover: Skyline of Chiral(c)ity. Chiral architectures adorn the skyline of Chiral(c)ity. *The Helix*, a pedestrian bridge in Singapore, and *Chicago Spire* are featured on the back cover. *Cayan Tower* of Dubai decorates the front cover together with *Enspire*, a sculpture in Traverse City, which likens the space-filling structure of the microtubes.
Cover design: Nastasia Griffioen.

Printed by: Gildeprint

ISBN: 978-90-393-7078-0

Chiral and Active Colloids

Chirale en Actieve Colloïden

(met een samenvatting in het Nederlands)

Proefschrift

ter verkrijging van de graad van doctor aan de
Universiteit Utrecht op gezag van de rector magnificus,
prof. dr. H. R. B. M. Kummeling, ingevolge het besluit van
het college voor promoties in het openbaar te verdedigen
op woensdag 16 januari 2019 des middags te 2.30 uur

door

Samia Ouhajji

geboren op 12 februari 1991 te Gorinchem

Promotor: Prof. dr. A. P. Philipse

Copromotor: Dr. A. V. Petukhov

Dit proefschrift werd (mede) mogelijk gemaakt met financiële steun van de Nederlandse Organisatie voor Wetenschappelijk Onderzoek (NWO), projectnummer 712.014.002.

Voor mijn ouders

Contents

1

Introduction

The purpose of this Chapter is to introduce the three concepts embodied in the title of this Thesis: colloids, chirality and active matter. After this introduction, the scope and outline of the various Chapters in this Thesis are discussed.

1.1 Colloids and Soft Matter

Soft matter[I] is finely structured matter with length scales intermediate between atomic and macroscopic dimensions.[2] The adjective 'soft' refers to the circumstance that this type of matter is easily deformed by external forces. Soft matter systems exhibit Brownian motion; the irregular, thermal motion named after the botanist Brown[II] who was one of the first to observe this behaviour.[3] Brownian motion is the thermal 'vehicle' for self-assembly of soft matter into three-dimensional structures.[4]

Colloidal suspensions are a specific class of soft matter.[5] Colloidal particles have characteristic sizes between several nanometres to several micrometres and once dispersed in a continuous liquid phase of a different composition or state, form colloidal dispersions.[6,7] Compared with bulk materials, colloids have a large surface to volume ratio as a relatively large fraction of atoms is located at the surface. Colloids can be directly visualized using microscopy techniques and their slow dynamics (relative to molecules) allows the particulate matter to be followed in time.

To disperse colloidal particles, colloid stability has to be ensured. The stability of charged colloids in an electrolyte solution is described by the DLVO theory.[8] A charged

---

[I] According to one of the founding fathers of soft matter:[1] 'Americans prefer to call it *complex fluids*. This is a rather ugly name, which tends to discourage the young students. But it does indeed bring in two of the major features.'

[II] Initially, Brown thought that the particles were alive until he realized that the motion occurred for both organic and inorganic matter.[3]

colloid is surrounded by an excess of oppositely charged ions in solution forming an electric double layer that is diffusive because of thermal ion motion. Repulsions by overlapping double layers oppose the short-ranged attractive van der Waals forces which are induced by interactions between fluctuating dipoles. Uncharged colloids can be sterically stabilized by attachment of polymers to colloid surfaces.[9] As two colloids with anchored, non-ionic polymers approach, the steric hindrance of the chains leads to repulsive interactions as the chains lose configurational entropy.

Colloidal dispersions can be prepared following bottom-up or top-down approaches.[10] An example of the latter is the milling or fractionation of an insoluble substance in a solution of stabilizing surfactants or polymers. Conversely, a molecular solution can be precipitated into larger units. Starting from a supersaturated solution, nucleation and growth stages are separated, preventing heterogeneous condensation to allow more control over the size and shape of the colloids.[10]

An example of preparation by milling is gamboge, a pigment derived from a rubber tree which was used to paint ornamental letters and illustrations in the Middle Ages.[11] Rubbing natural gamboge granules by hand under a thin film of distilled water results in spherical gamboge colloids though with a large polydispersity.[12] At the same time, gamboge can also be prepared via a condensation method through treatment with methanol. Gamboge was famously used by Perrin to determine the Avogadro constant and to substantiate the existence of molecules.[12]

Other illustrative examples of colloidal systems include ink, ice cream and peacock feathers. Ink, a colloidal dispersion of stabilized carbon particles in water, was previously prepared by the ancient Egyptians by mixing candle soot with Arabic gum.[10] Ice cream is a mixture of water crystals, cream and sugar, and air. Since the solvent is non-polar, the stability of the dispersion is safeguarded using polymeric chains to separate the colloids.[13] Lastly, the colours of peacock feathers do not fade over time as they are not produced by pigments or dyes.[14] Instead, the observed structural colours rely on the interaction of light with the microscopic structure of the feathers.[15]

Functionalized Colloids. Although attached polymer chains provide steric stabilization, *e.g.* Arabic gum in ink, polymers can also be employed for tuning particle properties. Surface attachment of polymers proceeds via covalent or non-covalent interactions. In the latter case, the polymers are physically adsorbed unto the colloids; covalent linking of polymers can happen through the ‘grafting to’ or ‘grafting from’ approach.[9] The ‘grafting to’ method employs pre-existing polymers or molecules which are attached through coupling reactions resulting in a functionalized surface.

An example is the coating of Stöber silica particles with stearyl alcohol via an esterification reaction.[16] This is experimentally a relatively easy method resulting in effectively hard spheres in organic solvents.[7,16] Non-aqueous dispersions of charged silica spheres were realized in weakly polar organic solvents in a similar fashion using 3-methacryloxypropyltrimethoxysilane (TPM) coating.[17]

However, the number of attached polymers per surface area is typically much larger with the 'grafting from' method. Here, polymers are grown one monomer at a time from an anchor point at the colloid surface. This approach is often used in conjunction with atom transfer radical polymerization (ATRP). ATRP is one of the most widely used controlled or living radical polymerization reactions and is exploited in Part II (Chapters 3 and 4) of this Thesis.[18] Employing ATRP, complex polymer structures are produced, catalysed by metal complexes that add monomers to a growing polymer chain, see Figure 1.1. Alkyl halides are the initiators or dormant, inactive species that react reversibly with the activating metal complexes forming propagating radicals and deactivators. When the dormant species is a polymer chain attached to colloidal particles, the process is denoted 'surface-initiated ATRP' (SI-ATRP). Temperature and other reaction conditions can be varied to terminate the ATRP equilibrium at any given time resulting in well-defined polymers with controlled composition end-functionalized with initiator molecules for possible end-group modifications.

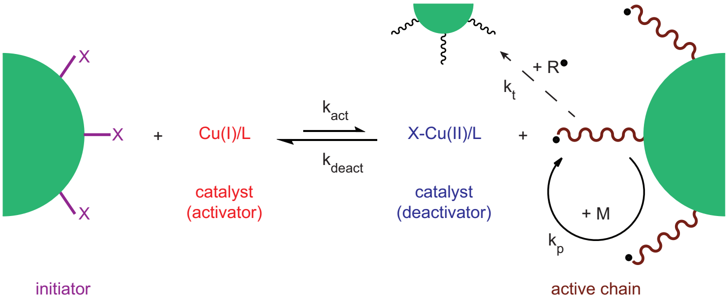

Figure 1.1: Schematic depiction of surface-initiated atom transfer radical polymerization. The propagating radicals (active chain) and dormant species (initiator) are in equilibrium, immobilized on a sphere's surface. The catalyst, generally a ligand coordinated copper based catalytic complex (Cu(I)/L), reacts with the dormant chain with reaction rate k_{act} forming a deactivator species. The chains undergo propagation reactions, with rate k_p, or termination reactions with reaction rate k_t. The dormant species and catalyst are regenerated in a reverse reaction of the deactivator with the propagating radical (rate k_{deact}).

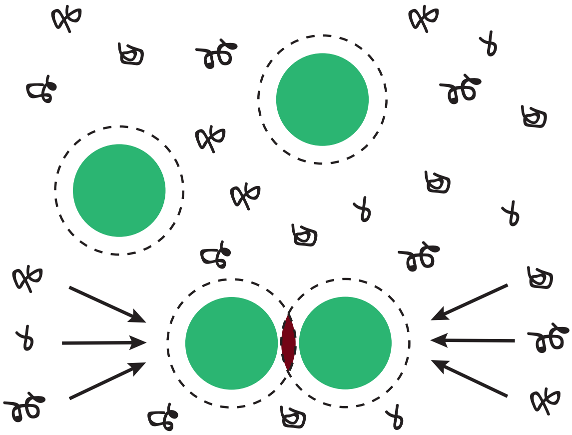

Figure 1.2: Schematic depiction of depletion interaction. In a mixture of colloidal spheres and non-adsorbing polymer, a depletion layer arises around the spheres as indicated by the dashed circles.[20] The centre of mass of the polymer is excluded (depleted) from this layer due to loss of configurational entropy. When two or more depletion layers overlap, the free volume available for the polymers increases. The polymers thus exert a net osmotic pressure on the colloids forcing the particles together.

Colloid-Polymer Mixtures. Whereas adsorbed or grafted polymers enhance the stability of colloids, the addition of non-adsorbing polymers can destabilize colloidal suspensions. Negative adsorption[III] of a polymer chain results in a loss of configurational entropy due to a depletion layer around the colloid which the centre of mass of the polymer cannot penetrate.[20] To minimize their free energy, the polymers exert a net osmotic pressure on the colloids forcing the particles together. This apparent attraction between the colloidal particles is named the depletion interaction, see Figure 1.2. It is an apparent attraction as depletion is entropically driven and arises as a result of purely repulsive colloid-colloid and colloid-polymer interactions. The range of the depletion potential is determined by the size of the depletant, whereas the attraction strength depends on the osmotic pressure and thus on the depletant concentration. Therefore, the strength and the range of the attraction between colloids can be modified independently using depletion forces, as shown in Chapter 6.

[III] Polymers that are depleted but are weakly adhesive result in a non-zero polymer concentration at the surface of colloidal particles. This weak adhesion sensitively affects depletion forces by shifting the phase stability of colloid-polymer mixtures to higher polymer concentrations. Weak adhesion arises, among others, in a system of silica spheres coated with stearyl alcohol, and polydimethylsiloxane in cyclohexane.[19]

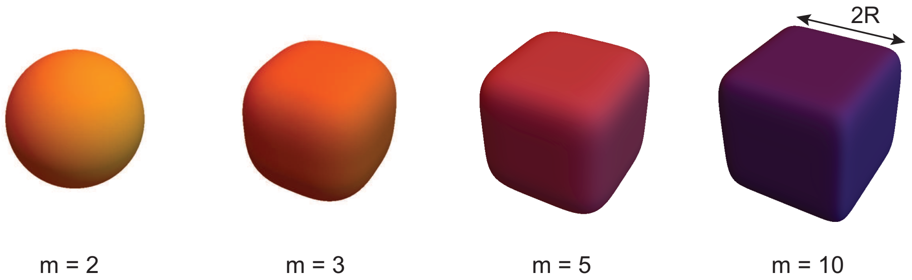

Figure 1.3: Superballs. Schematic depiction of superballs with different values of m.

Cubic Colloids. Thus far, the focus in this Introduction has been mainly on spherical particles. Spheres are thermodynamically the simplest shape and are relatively easily produced experimentally. However, over the past decades many other shapes of colloids have been realized experimentally, including cubic-shaped colloids.[21] Cubes with rounded edges can be described mathematically by superballs, symmetric particles defined by:[22]

$$|x|^m + |y|^m + |z|^m \leq R^m, \tag{1.1}$$

where x, y and z are the Cartesian coordinates and m is the shape parameter. m indicates the extent of deformation from a sphere ($m = 2$) with radius R. As m increases, the particles resemble a cube more as edges sharpen and faces flatten. Figure 1.3 shows superballs for different values of m. In Chapter 8 we use superball-shaped colloids to prepare novel cubic microswimmers.

Confined Colloids. In Chapter 5, the effect of cylindrical confinement on colloidal spheres is explored. The confinement is provided by microtubes which are formed from sugar and surfactant molecules. Mixtures of β-cyclodextrin (β-CD) and sodium dodecyl sulphate (SDS) form complexes in a 2:1 molar ratio at temperatures above 40 °C in water through incorporation of the hydrophobic tail of SDS inside the hydrophobic cavity of β-CD.[23] The resulting complexes have a completely hydrophilic exterior. Upon cooling to room temperature these SDS@2β-CD complexes self-assemble into hollow microtubes driven by hydrogen bond formation and mediated by electrostatic interactions, see Figure 1.4. Phases dominated by lamellae or vesicles are formed depending on the concentration of the SDS@2β-CD inclusion complexes. The microtubes are rigid, extend up to several tens of micrometres but have a well-defined diameter of about one micrometre; detailed characterization can be found in Chapter 2. Addition of colloids with varying geometries, materials and sizes results in various thermo-reversible supra-colloidal structures inside the 1D confinement of the microtubes.[24–26]

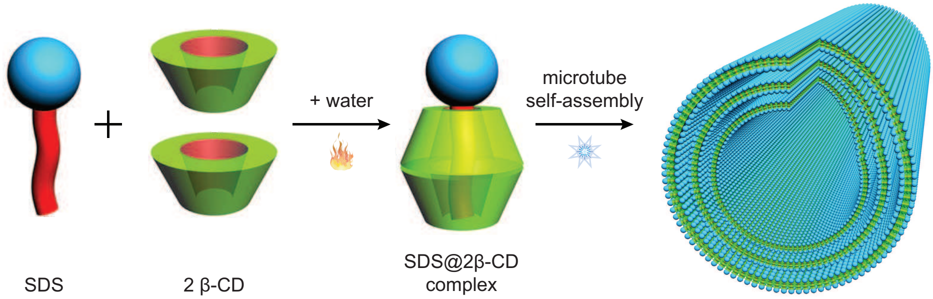

Figure 1.4: Self-assembly of SDS and β-CD into hollow microtubes. At elevated temperatures, one surfactant and two sugar molecules form host-guest inclusion complexes. Upon cooling the system down, hollow microtubes are formed. Image adapted from Jiang et al.[23]

1.2 Chirality

Chirality is a property of geometrical objects of which the mirror image is not superimposable with the original.[27] Lord Kelvin[IV] was the first to adopt the term chirality, from the Greek word χειρ for 'hand', perhaps the most familiar example of a chiral object.[29] While the physical properties such as melting temperature or colour, of left- and right-handed molecules are identical, the handedness of a molecule sensitively affects its odour, potency or toxicity.[27,29] Chiral isomers of the molecule limonene, for example, are responsible for the distinct aromas of lemons and oranges.[30]

The absence of inversion symmetry manifests itself over many length scales; from the double helix of DNA to the coiling of cucumber tendrils[31] and liquid crystals. Liquid crystals are the state of matter in between disordered liquids and ordered crystalline solids.[32,33] Whereas achiral rods form a nematic phase with long-range orientational order but no positional ordering, chiral rods can transform the nematic into a chiral nematic (or cholesteric) phase in which the orientation of the rods is rotated over

---

[IV] In Lord Kelvins words: 'I call any geometrical figure, or group of points, chiral, and say it has chirality if its image in a plane mirror, ideally realized, cannot be brought to coincide with itself.'[28]

a macroscopic distance. However, molecular chirality does not ensure macroscopic chiral structures. For instance, both the tobacco mosaic virus and *fd* virus are chiral with similar helical structures. While the former only forms a nematic phase, the latter exhibits a chiral nematic phase. Grelet and Fraden addressed this discrepancy 16 years ago in their seminal paper titled 'What is the origin of chirality in the cholesteric phase of virus suspensions?'[34] To this day, this question remains unanswered as the connection between microscopic and macroscopic chirality is not understood for many systems not only in virus suspensions.[35]

Two simple systems exhibiting spontaneous chiral symmetry breaking were studied theoretically by Pickett et al.[36] Close-packed isotropic spheres were found to form helical structures upon cylindrical confinement due to geometrical restrictions.[37,38] Macroscopically this can be visualized by filling a measuring cylinder with marbles of the proper size ratio. Microscopically this can be realized by the co-assembly of colloids and microtubes. The second system consists of unconfined dipolar spheres with an additional isotropic attraction. This system can be approximated by magnetic colloids aligned in an external magnetic field in the presence of depletants. The particles will arrange themselves in chiral chains to accommodate more neighbours, increasing the free volume available for the depletants and thus lowering the energy of the system. Both systems are studied experimentally in Chapters 5 and 6, respectively.

1.3 Active Matter

Although Brownian motion is a driving force for the self-assembly of soft matter, the erratic movement due to thermal fluctuations is a form of passive motion as particles do not have an active role in their motion.[3,39] Cells, birds and cars on the other hand exhibit active motion; motion that requires energy consumption from the environment and subsequent conversion into kinetic energy.[40,41]

The scallop theorem states that non-reciprocal motion is required for microscopic objects to self-propel in water due to the low Reynolds number at these length scales.[42,43] A scallop moves by opening its shell slowly and closing it fast; a microscopic scallop would have a net displacement of zero as it exactly reverses its trajectory and returns to its original position. Inspired by micro-organisms hunting for food propelled by flagella, artificial microswimmers were realized by Dreyfus and co-workers.[44] Magnetic particles were linked by DNA and attached to a red blood cell resulting in a controlled swimming motion in an oscillatory magnetic field.[45]

Non-equilibrium motion can also be achieved by combining phoretic effects with chemical reactions to create field gradients, *e.g.* in concentration.[46] For example, chemical energy can be converted into mechanical work by a spherical particle covered with an asymmetric distribution of catalyst. The chemical reaction taking place at the particle surface produces a concentration gradient that propels the particle by self-diffusiophoresis. A classic example is the catalytic dissociation of hydrogen peroxide into water and oxygen by platinum.[47–51] Typical behaviour of active particles consists of directed or ballistic motion at short times, while a random walk is observed at longer times be it with a significantly enhanced diffusion coefficient.[43]

1.4 Scope and Outline of This Thesis

The motivation for the bulk of this Thesis (Part I, II and III) is the development of a model system of chiral colloids suitable for studying the effects of microscopic chirality on thermodynamic and transport properties of colloidal dispersions.

In Part I, we characterize in detail the hierarchical self-assembly of sugar and surfactant molecules into hollow tubular microstructures (Chapter 2). Small-angle x-ray scattering was used to study the formation of microscale cylinders that are employed as confining environment for colloids in Part III.

Part II describes the synthesis of photo-responsive[I] colloids. SI-ATRP is employed to graft polymer hairs from the surface of the colloids for steric stabilization and for end-group modification with coumarin, a photo-responsive molecule. In Chapter 3, coumarin-modified polystyrene spheres are prepared that exhibit photo-induced aggregation in bulk, while Chapter 4 reports the synthesis of magnetic and photo-responsive silica spheres. The magnetic spheres form rodlike chains that can be manipulated with external magnetic fields.

Part III, combines the results of Part I and II to assemble chiral colloids from isotropic spheres. Photo-responsive polystyrene spheres are confined in the cylindrical environment of the microtubes in Chapter 5, forming a variety of structures including helical sphere chains. Chapter 6 reports the formation of chiral colloidal chains from magnetic and photo-responsive spheres induced by depletion interaction. In Chapter 7, we study the Brownian dynamics of a helical structure.

The remainder of this thesis, Part IV, discusses active matter. Whereas most research in the field of active matter focuses on spherical particles, in Chapter 8 we describe the realization of cubic microswimmers. The core-shell superballs exhibit

---

V. The first synthetic photo-reactive polymer was realized by Minsk and co-workers in the 1950s. The use of photo-reactions, however, can be traced back to the ancient Egyptians and Babylonians. Approximately 4000 years ago, they employed sunlight to photo-crosslink linens for mummification and to make papyrus boats waterproof.[52]

characteristic active motion, ballistic at short times and randomized motion at long time scales.

Acknowledgements

Álvaro González García is thanked for providing the schematic images of the superballs.

References

1. P. de Gennes. Soft matter, *Nobel Lecture* **1991**.
2. D. F. Evans & H. Wennerström. *The Colloidal Domain: Where Physics, Chemistry, Biology, and Technology Meet*, Wiley-VCH, **1999**.
3. A. P. Philipse. *Brownian Motion: Elements of Colloid Dynamics*, Springer Nature Switzerland AG, **2018**.
4. A. van Blaaderen. Materials science: Colloids get complex, *Nature* **2006**, *439*, 545–546.
5. K. Mysels. *Introduction to Colloid Chemistry*, Interscience Publishers, Inc., **1959**.
6. J. Lyklema. 'Introduction to Colloid Science' in *Fundamentals of Interface and Colloid Science, Vol. IV*, Elsevier, **2005**.
7. A. Vrij & R. Tuinier. 'Structure of Concentrated Colloidal Dispersions' in *Fundamentals of Interface and Colloid Science, Vol. IV*, Elsevier, **2005**.
8. E. J. W. Verwey & J. T. G. Overbeek. *Theory of the Stability of Lyophobic Colloids*, Dover Publications, **1999**.
9. D. H. Napper. Steric stabilization, *J. Colloid Interface Sci.* **1977**, *58*, 390–407.
10. A. P. Philipse. 'Particulate Colloids: Aspects of Preparation and Characterization' in *Fundamentals of Interface and Colloid Science, Vol. IV*, Elsevier, **2005**.
11. H. Skelton. A colour chemist's history of western art, *Rev. Prog. Color. Relat. Top.* **1999**, *29*, 43–64.
12. J. Perrin. Mouvement brownien et réalité moléculaire, *Ann. Chim. Phys.* **1909**, *18*, 1–114.
13. H. D. Goff. Colloidal aspects of ice cream - A review, *Int. Dairy J.* **1997**, *7*, 363–373.

14. J. Zi, X. Yu, Y. Li, X. Hu, C. Xu, X. Wang, X. Liu & R. Fu. Coloration strategies in peacock feathers, *Proc. Natl. Acad. Sci.* **2003**, *100*, 12576–12578.

15. A. van Blaaderen. Opals in a new light, *Science* **1998**, *282*, 887–888.

16. A. K. van Helden, J. W. Jansen & A. Vrij. Preparation and characterization of spherical monodisperse silica dispersions in nonaqueous solvents, *J. Colloid Interface Sci.* **1981**, *81*, 354–368.

17. A. P. Philipse & A. Vrij. Preparation and properties of nonaqueous model dispersions of chemically modified, charged silica spheres, *J. Colloid Interface Sci.* **1989**, *128*, 121–136.

18. K. Matyjaszewski & N. V. Tsarevsky. Nanostructured functional materials prepared by atom transfer radical polymerization, *Nat. Chem.* **2009**, *1*, 276–288.

19. R. Tuinier, S. Ouhajji & P. Linse. Phase behaviour of colloids plus weakly adhesive polymers, *Eur. Phys. J. E* **2016**, *39*, 115.

20. H. N. W. Lekkerkerker & R. Tuinier. *Colloids and the Depletion Interaction*, Springer Netherlands, **2011**.

21. L. Rossi, S. Sacanna, W. T. M. Irvine, P. M. Chaikin, D. J. Pine & A. P. Philipse. Cubic crystals from cubic colloids, *Soft Matter* **2011**, *7*, 4139–4142.

22. R. D. Batten, F. H. Stillinger & S. Torquato. Phase behavior of colloidal superballs: Shape interpolation from spheres to cubes, *Phys. Rev. E* **2010**, *81*, 061105.

23. L. Jiang, Y. Peng, Y. Yan, M. Deng, Y. Wang & J. Huang. “Annular Ring” microtubes formed by SDS@2β-CD complexes in aqueous solution, *Soft Matter* **2010**, *6*, 1731–1736.

24. L. Jiang, J. W. J. de Folter, J. Huang, A. P. Philipse, W. K. Kegel & A. V. Petukhov. Helical colloidal sphere structures through thermo-reversible co-assembly with molecular microtubes, *Angew. Chem. Int. Ed.* **2013**, *52*, 3364–3368.

25. J. W. J. de Folter, P. Liu, L. Jiang, A. Kuijk, H. E. Bakker, A. Imhof, A. van Blaaderen, J. Huang, W. K. Kegel, A. P. Philipse & A. V. Petukhov. Self-organization of anisotropic and binary colloids in thermo-switchable 1D microconfinement, *Part. Part. Syst. Charact.* **2015**, *32*, 313–320.

26. P. Liu, J. W. J. de Folter, A. V. Petukhov & A. P. Philipse. Reconfigurable assembly of superparamagnetic colloids confined in thermo-reversible microtubes, *Soft Matter* **2015**, *11*, 6201–6211.

27. W. Ma, L. Xu, A. F. de Moura, X. Wu, H. Kuang, C. Xu & N. A. Kotov. Chiral inorganic nanostructures, *Chem. Rev.* **2017**, *117*, 8041–8093.
28. W. T. Kelvin. *The Molecular Tactics of a Crystal*, Clarendon Press, **1894**.
29. A. B. Harris, R. D. Kamien & T. C. Lubensky. Molecular chirality and chiral parameters, *Rev. Mod. Phys.* **1999**, *71*, 1745–1757.
30. K. Nayani, Y.-K. Kim & N. L. Abbott. Chiral interactions in liquid crystals, *Nat. Mater.* **2018**, *17*, 14–15.
31. S. J. Gerbode, J. R. Puzey, A. G. McCormick & L. Mahadevan. How the cucumber tendril coils and overwinds, *Science* **2012**, *337*, 1087–1091.
32. E. Barry, Z. Hensel, Z. Dogic, M. Shribak & R. Oldenbourg. Entropy-driven formation of a chiral liquid-crystalline phase of helical filaments, *Phys. Rev. Lett.* **2006**, *96*, 018305.
33. H. H. Wensink & L. Morales-Anda. Chiral assembly of weakly curled hard rods: Effect of steric chirality and polarity, *J. Chem. Phys.* **2015**, *143*, 144907.
34. E. Grelet & S. Fraden. What is the origin of chirality in the cholesteric phase of virus suspensions?, *Phys. Rev. Lett.* **2003**, *90*, 198302.
35. S. Dussi, S. Belli, R. van Roij & M. Dijkstra. Cholesterics of colloidal helices: Predicting the macroscopic pitch from the particle shape and thermodynamic state, *J. Chem. Phys.* **2015**, *142*, 074905.
36. G. T. Pickett, M. Gross & H. Okuyama. Spontaneous chirality in simple systems, *Phys. Rev. Lett.* **2000**, *85*, 3652–3655.
37. A. Mughal, H. K. Chan & D. Weaire. Phyllotactic description of hard sphere packing in cylindrical channels, *Phys. Rev. Lett.* **2011**, *106*, 115704.
38. A. Mughal, H. K. Chan, D. Weaire & S. Hutzler. Dense packings of spheres in cylinders: Simulations, *Phys. Rev. E* **2012**, *85*, 051305.
39. U. Erdmann, W. Ebeling, L. Schimansky-Geier & F. Schweitzer. Brownian particles far from equilibrium, *Eur. Phys. J. B* **2000**, *15*, 105–113.
40. F. Schweitzer. *Brownian Agents and Active Particles: Collective Dynamics in the Natural and Social Sciences*, Springer, **2003**.
41. W. Poon. From Clarkia to Escherichia and Janus: The physics of natural and synthetic active colloids, *arXiv* **2013**.
42. E. M. Purcell. Life at low Reynolds number, *Am. J. Phys.* **1977**, *45*, 3–11.

43. J. R. Howse, R. A. L. Jones, A. J. Ryan, T. Gough, R. Vafabakhsh & R. Golestanian. Self-motile colloidal particles: From directed propulsion to random walk, *Phys. Rev. Lett.* **2007**, *99*, 048102.

44. C. Bechinger, R. Di Leonardo, H. Löwen, C. Reichhardt, G. Volpe & G. Volpe. Active particles in complex and crowded environments, *Rev. Mod. Phys.* **2016**, *88*, 045006.

45. R. Dreyfus, J. Baudry, M. L. Roper, M. Fermigier, H. A. Stone & J. Bibette. Microscopic artificial swimmers, *Nature* **2005**, *437*, 862–865.

46. J. Zhang & S. Granick. Natural selection in the colloid world: Active chiral spirals, *Faraday Discuss.* **2016**, *191*, 35–46.

47. J. G. Gibbs & Y.-P. Zhao. Autonomously motile catalytic nanomotors by bubble propulsion, *Appl. Phys. Lett.* **2009**, *94*, 163104.

48. H. Ke, S. Ye, R. L. Carroll & K. Showalter. Motion analysis of self-propelled Pt-silica particles in hydrogen peroxide solutions, *J. Phys. Chem. A* **2010**, *114*, 5462–5467.

49. L. Baraban, M. Tasinkevych, M. N. Popescu, S. Sanchez, S. Dietrich & O. G. Schmidt. Transport of cargo by catalytic Janus micro-motors, *Soft Matter* **2012**, *8*, 48–52.

50. L. Baraban, D. Makarov, R. Streubel, I. Mönch, D. Grimm & O. G. Schmidt. Catalytic Janus motors on microfluidic chip: Deterministic motion for targeted cargo delivery, *ACS Nano* **2012**, *6*, 3383–3389.

51. K. K. Dey & A. Sen. Chemically propelled molecules and machines, *J. Am. Chem. Soc.* **2017**, *139*, 7666–7676.

52. S. R. Trenor, A. R. Shultz, B. J. Love & T. E. Long. Coumarins in polymers: From light harvesting to photo-cross-linkable tissue scaffolds, *Chem. Rev.* **2004**, *104*, 3059–3077.

PART I

Microtubes

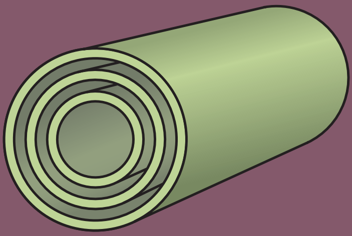

2

In Situ Observation of Self-Assembly of Sugars and Surfactants from Nanometres to Microns

Abstract

The hierarchical self-assembly of sugar and surfactant molecules into hollow tubular microstructures was characterized *in situ* with high resolution small-angle x-ray scattering spanning more than three orders of magnitude of spatial scales. Scattering profiles reveal that aqueous host-guest inclusion complexes self-assemble into multiple equally spaced curved bilayers forming a collection of concentric hollow cylinders. Scattering data can be described by a simple theoretical model of the microtubes. The interlamellar distance was found to be surprisingly large. Moreover, we report that the multi-walled structure of the microtubes swells as the concentration or the temperature is changed.

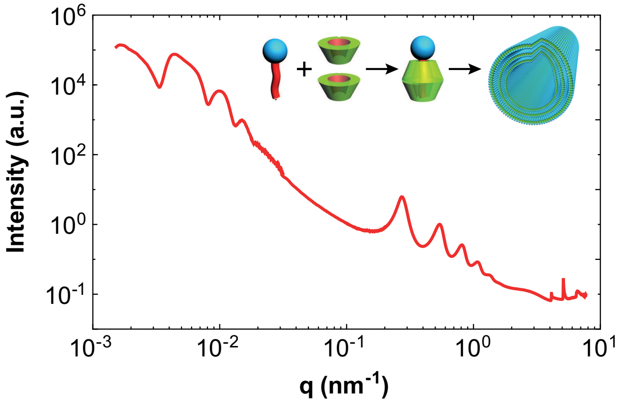

2.1 Introduction

The spontaneous formation of a complex ordered structure by self-assembly of disordered building blocks is a ubiquitous phenomenon in nature.[1] For instance, soap molecules self-organize into micelles, cell membranes are spontaneously formed by phospholipids, and virus capsids, the nanosized containers protecting viral DNA, self-assemble inside infected cells.[2] A more complex example is provided by the tobacco mosaic virus. This rodlike virus consists of thousands of protein units that are joined together by a single RNA chain.[3] This form of self-assembly, where several distinct spatial scales are involved, is known as hierarchical self-assembly. Highly ordered structures on the molecular, nanometre and micrometre scale can be formed by hierarchical self-assembly and could exhibit unique properties that are not inherent to the individual building blocks.[3] The mechanical strength and toughness of bone, for example, is related to its hierarchical structure.[4] Other examples include bamboo and nacre,[5] architected metamaterials,[6] hollow spherical micelles from rodlike block co-polymers,[7] supramolecular polyhedra from DNA[8] and responsive gels formed by peptides.[9] In most cases the hierarchical self-assembly takes place in heterogeneous systems, where multiple components are needed to ensure self-assembly at different structural levels.

Another interesting example is provided by cyclodextrins and surfactants that exhibit hierarchical self-assembly in amphiphilic systems spanning several orders of magnitude of spatial scales.[10–13] Cyclodextrins (CDs) are donut-like oligosaccharides with a hydrophilic outer surface and a hydrophobic cavity. CDs and surfactants can form aqueous host-guest inclusion complexes due to protection of the hydrophobic tail of the surfactants inside the hydrophobic cavity of CD. For example, two β-cyclodextrin (β-CD) molecules and one sodium dodecyl sulphate (SDS) molecule can spontaneously form host-guest complexes in water resulting in a SDS@2β-CD inclusion complex with a hydrophilic exterior. Depending on the concentration of the complexes in aqueous solutions, various structures can be formed, including vesicles, microtubes and lamellae.[10,13,14] The first two structures are formed due to bending of the lamellae in one or more directions presumably due to a trade-off between the energy required to curve the lamellae and the energy gained upon counterion condensation.[15] It is unique that in this system the hierarchical self-assembly occurs spontaneously by using a single building block, namely, the inclusion complex.

In this Chapter, we demonstrate that synchrotron small-angle x-ray scattering (SAXS) is able to clearly resolve *in situ* all relevant scales of structural organization of simple sugar and surfactant molecules spanning length scales over three orders of magnitude. It was possible to follow the self-assembly starting with the formation of two-dimensional bilayers which are subsequently curved into three-dimensional multi-walled tubular structures ordered in a space-filling arrangement. Furthermore, the melting and swelling in the system due to variations in temperature and concentration, respectively, were studied.

2.2 Experimental Methods

2.2.1 Materials. Sodium dodecyl sulphate (SDS, >97%), β-cyclodextrin (β-CD) and Nile Red (bioreagent for HPLC, >98 %) were purchased from Sigma-Aldrich. β-CD was dried before use to remove excess water. All water used in the experiments was purified by a Milli-Q system.

2.2.2 Sample Preparation. Desired amounts of SDS, β-CD and water were weighed to obtain a molar ratio of β-CD:SDS of 2:1 and a final concentration of SDS and β-CD of 10, 15 or 20 wt% in water. The mixture was heated in an oil bath to 60 °C while stirring with a magnetic stirrer until a transparent and isotropic solution was obtained. Upon cooling to room temperature the microtubes were formed and a viscous and turbid suspension is observed.

2.2.3 Small-Angle X-ray Scattering (SAXS). For SAXS measurements, microtubes suspensions were transferred to round quartz capillaries with a length of 80 mm, a diameter of 1 or 2 mm and wall thickness of 0.01 mm (Hilgenberg GmbH or Hampton research). Capillaries were sealed with epoxy glue (Bison kombi, two component glue). Samples were measured after 48 hours of incubation but within 5 days of sample preparation. SAXS measurements were performed at the high brilliance beamline ID02 at the ESRF (Grenoble, France).[16] X-rays with a wavelength of 0.0995 nm were employed and three different sample-detector distances LSD were used. For the smallest q-range the scattering data were recorded by FReLoN 16M detector with LSD = 30.7 metre. For mid-q and large-q range the Rayonix MX-170HS detector was operated with LSD = 12 and 1 metre respectively. This set-up made it possible to record scattering data from q = 0.0015 nm^{-1} to 8 nm^{-1}, where $q = (4\pi/\lambda)\sin(\theta)$ with 2θ the angle between the incident and scattered waves.

Background corrections were performed on all radial intensity profiles. Background was obtained from scattering recorded from capillaries filled with pure water. Scattered intensity was averaged over at least ten measurements.

2.2.4 Confocal Laser Scanning Microscopy (CLSM). Samples were dyed with Nile Red. A stock solution of 1 mg/mL Nile Red in acetone was made. 10 μL of the stock solution was added to 1 mL of microtubes heated to 60 °C. The sample was sonicated for 1 minute while cooling down and was allowed to equilibrate overnight. Microscope samples were made by sealing a drop of microtubes suspension between two glass slides (Menzel-Gläser, 0.17 mm thick). A Nikon TE2000U inverted microscope with a C1 confocal scan head and a 100× Nikon oil objective was used to perform CLSM experiments. A HeNe laser with a wavelength of 543.5 nm (Melles Griot) was used to excite the Nile Red dye.

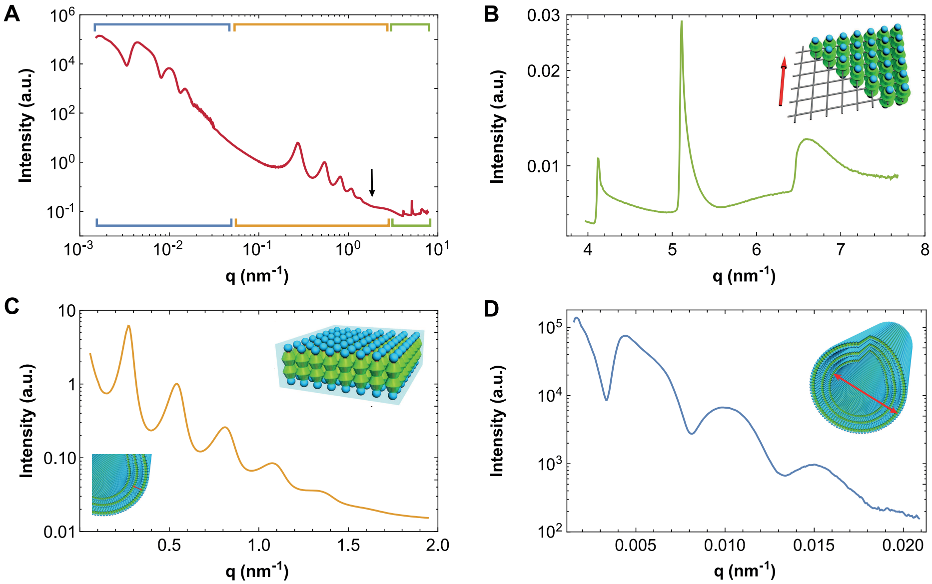

Figure 2.1: SAXS measurements of 10 wt% SDS@2β-CD complexes in water. (a) Radial intensity profile I as a function of wavevector q showing the complete set of data, measured using three sample-to-detector distances. The black arrow pinpoints the form factor minimum of the bilayers. (b) The saw-tooth shaped peak characteristic of 2D structures at high q. The inset shows the in-plane rhombic unit cell. (c) Inter- and intra-bilayer structure of the walls of the microtubes with a lamellar spacing of 23 nm. Insets show models of the bilayer and the multiwalled structure of the microtubes. The red arrows illustrate the bilayer thickness and interlamella distance. (d) At low q, the average diameter of the microtubes can be observed as indicated with the red arrow in the inset.

2.3 Results and Discussion

2.3.1 Hierarchical Self-Assembly. Figure 2.1a gives an overview of the radial intensity profile, $I(q)$, of aqueous solutions of 10 wt% SDS@2β-CD complexes measured at room temperature at a fixed position in the bulk. Various regions are shown in more detail in Figure 2.1b-d. The SDS@2β-CD complexes form 2D assemblies as revealed by the characteristic saw-tooth shaped peak in Figure 2.1b; *i.e.* a peak with a rapidly rising edge at low angles followed by a continuous decrease toward larger scattering angles.[17,18] At smaller angles, see Figure 2.1c, a form factor minimum appears. The position of this minimum corresponds to a thickness of 3.5 nm, which is comparable to twice the length of a SDS molecule. This suggests that the walls of the 2D assemblies are composed of bilayers. Strong equidistant peaks are observed at intermediate angles and are characteristic of 1D periodicity (see Figure 2.1c). These structure factor peaks are typically found in lamellar structures[19] implying that our 2D assemblies consist of multiple equally spaced bilayers. Remarkably, the bilayers are a distance of 23 nm apart as can be deduced from the distance between adjacent peaks. As there is no (extra) added salt in the system, the large distances between the evenly spaced bilayers is thought to be due to counterion condensation.[20] Preliminary experiments with additional added salt have shown that the inter-bilayer distance decreases as the ionic strength increases, further strengthening our hypothesis.

Figure 2.2 shows a 2D SAXS pattern recorded near the capillary wall. The tubular structures here are aligned parallel to each other due to anchoring at the wall of the capillary, making it possible to collect data from a single domain yielding an oriented scattering pattern. The positioning of the capillary results in horizontally aligned microtubes and bilayers that are rolled around the horizontal axis. The in-plane periodicity along the axis of the microtubes remains unaffected while the remaining diffraction peaks show broadening only in the vertical direction supporting the conclusion that the tubes are indeed rolled around the horizontal axis. The in-plane unit cell consistent with the 2D SAXS pattern can be indexed by a rhombus with a = b = 1.52 nm and $\gamma = 104°$. A schematic representation of the unit cell is given in the inset of Figure 2.1b. The average size of the tubes can be determined from the form factor minima observed at small angles as shown in Figure 2.1d. The distance between these minima corresponds to 2π divided by 1.3 μm, the latter manifesting in the presence of large objects on the order of a micrometre.

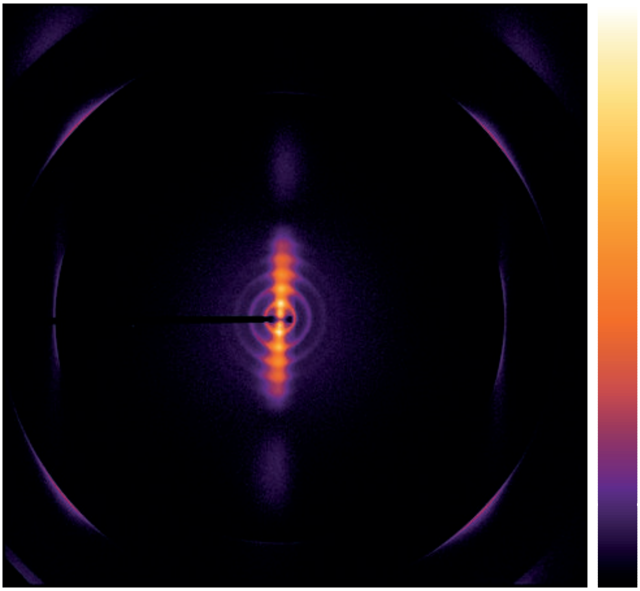

Figure 2.2: 2D SAXS pattern. Pattern was measured from a single domain near the capillary wall.

2.3.2 Concentric Cylinder Model. To further confirm that the microtubes consist of a multi-walled bilayer structure, the experimental scattering curve of the microtubes was fitted to the scattering of a hollow cylinder consisting of a number of evenly spaced concentric cylinders with wall thickness t and inter-bilayer periodicity s. The microtubes consist of n concentric cylinders with radius $R_j = R_0 + js$, with $0 \leq j \leq (n-1)$ and R_0 denoting the radius of the innermost cylinder. The orientationally averaged x-ray scattering intensity is then proportional to:[21]

$$I(q) \propto \frac{1}{q}\left(\sum_{j=0}^{n-1}(P_{R_j+t/2} - P_{R_j-t/2})\right)^2, \tag{2.1}$$

where P_R is the orientationally averaged scattering amplitude of a full cylinder with radius R, given by:

$$P_R(q) \propto \frac{RJ_1(qR)}{q}. \tag{2.2}$$

Here, J_1 is the first order cylindrical Bessel function and q is the wave vector. Equation 2.1 was used to fit the scattering data with the experimental parameters $t = 3.5$ nm and $s = 23$ nm. A reasonably accurate fit of the experiments was obtained using $n = 7$ concentric cylinders, $R_0 = 540$ nm and introducing polydispersity up to 10%. The experimental and theoretical scattering curves are shown in Figure 2.3. For small wavevectors q, the fit revealed that the distance between these minima is equal to 2π divided by the average diameter of the microtubes defined as $2R_0 + (n-1)s$, which is thus equal to 1.3 μm.

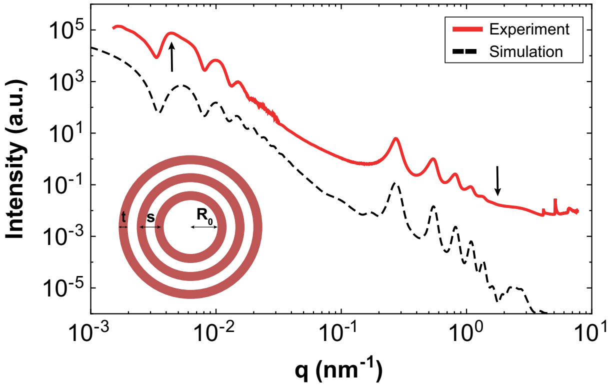

Figure 2.3: Experimental and calculated scattering curves of 10 wt% microtubes. The fit does not show the saw-tooth shaped peak as this peak is a result of the apparent change in the distance between the complexes in the bilayer which is not taken into account in the model. For this fit, $t = 3.5$ nm, $s = 23$ nm, $n = 7$ and $R_0 = 540$ nm were used. The black arrows indicate the structure factor correlation peak and form factor minimum. The calculated curve has been offset vertically for the sake of clarity. Geometrical parameters in the model are introduced in the inset.

The experimental and theoretical data deviate in two aspects. At the largest angles, the saw-tooth shaped peak is absent in the fit. This difference arises as a consequence of using homogeneous cylinders and not explicitly modelling the complexes composing the bilayers. In addition, a small but distinguishable peak can be seen at $q \cong 0.0044$ nm^{-1} in the experimental data only. Generally, the total scattering intensity is a combination of the form factor $P(q)$ and the structure factor $S(q)$ according to $I(q) \propto P(q) \times S(q)$. For dilute samples, the structure factor equals unity as structure correlations do not affect the scattering and equation 2.1 holds. In all other cases, additional structure factor peaks will appear in the scattering intensity curve. Here, the structure factor correlation peak at small angles corresponds to a centre-to-centre distance between the microtubes of approximately 1.6 μm. With a diameter of 1.4 μm, the spacing between the microtubes is negligible and a space-filling arrangement is formed.

2.3.3 Temperature and Concentration. Finally, the response of the system to variations in concentration and temperature was probed. Aqueous solutions of SDS@2β-CD complexes spontaneously self-assemble into hollow microtubes as long as the total concentration of β-CD and SDS is in the region between 6 and 25 wt%.[14] To investigate the effect of concentration on the microtubes, scattering curves were recorded from microtubes in suspension, well-aligned along the capillary wall, at varying concentrations. Figure 2.4a shows that upon dilution of the system, *i.e.* as the SDS@2β-CD complex concentration decreases from 20 to 10 wt%, swelling of the multiwall structure of the microtubes is observed. The periodicity between the bilayers making up the walls of the microtubes increases from 15 via 18 to 23 nm for 20, 15 and 10 wt% respectively as can be concluded from the shift of the equidistant structure factor peaks to larger angles. In addition, the overall diameter of the microtubes changes as was confirmed by confocal microscopy images, see Figure 2.5. The microtubes grow by incorporating more SDS and cyclodextrin molecules into the walls which in turn become more compact to accommodate for the additional complexes upon increasing concentration. It must be noted that while the overall diameter of the microtubes grows, the pore diameter of the hollow tubes shrinks. Furthermore, the form factor minimum corresponding with the bilayer thickness, becomes more pronounced at higher concentrations of host-guest inclusion complexes.

As the formation of complex structures from SDS@2β-CD complexes is thermo-reversible, it is thus possible to switch between assembly and disassembly of the microtubes by simply changing the temperature. Above the temperature of 40 °C, the microtubes tend to melt as is confirmed by the featureless scattering seen in Figure 2.4b. Below this threshold temperature, multiple oscillations can be observed. Initially, it was thought that these oscillations were due to formation of vesicles considering that Zhou and co-workers had previously shown that a reversible transition between vesicles and microtubes can be triggered by temperature.[22] In their work, however, vesicles are dominant only above a temperature of 43 °C. Between 40 °C and 43 °C, a phase transition from microtubes to vesicles takes place and a mixture of both entities is obtained. Finally, at temperatures lower than the threshold temperature of 40 °C, vesicles are not formed at all.

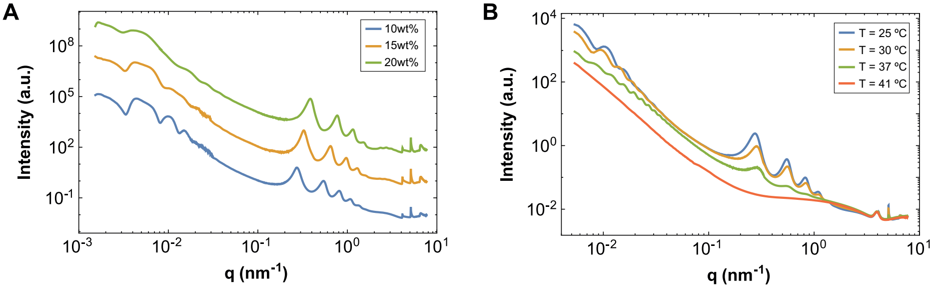

Figure 2.4: The response of the thermo-reversible microtubes to variations in concentration and temperature. (a) Upon dilution of the microtubes, swelling of the multiwall structure is observed. The structure factor peaks at intermediate angles shift to smaller wavevectors resulting from a larger inter-bilayer periodicity. The curves have been offset for the sake of clarity. (b) Above 40 °C, the characteristic features in the scattering curve disappear as the microtubes melt and fall apart. The broad peak around $q = 4\,\mathrm{nm}^{-1}$ originates from scattering of the polyimide film (Kapton) on the window of the heating stage used during the temperature measurements.

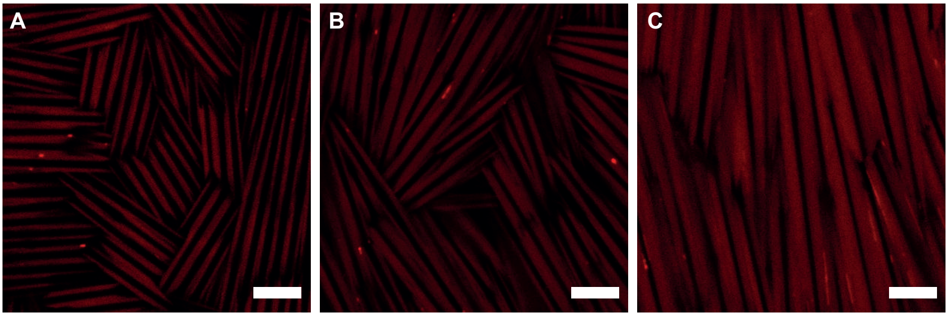

Figure 2.5: Confocal microscopy images. (a) 10, (b) 15 and (c) 20 wt% SDS@2β-CD complexes in aqueous solution. As the concentration is increased, the overall diameter of the microtubes increases. The walls of the microtubes become thicker as the pore diameter decreases in size. Scale bars are 5 μm.

On the other hand, the oscillations that are apparent in Figure 2.4b are only present below this threshold temperature and disappear above 40 °C. Furthermore, the reported size of vesicles is much smaller than the characteristic size obtained from the scattering. Whereas bidisperse mixtures of vesicles in the sizes 700 and 200 nm were reported,[10] here the oscillations are due to structures of approximately 1.7 μm. We hypothesize that these oscillations are due to radial enlargement of the microtubes upon heating, leading to monodisperse tubular structures with a well-defined radius.

2.4 Conclusions and Outlook

In conclusion, we have studied in detail the hierarchical and thermo-reversible self-assembly of mixtures of sugar and surfactant molecules into microtubes using synchrotron SAXS. The self-assembly of this complex system could be characterized *in situ*, covering a total of more than three orders of magnitude of spatial scales, with one characterization technique. The microtubes consist of multiple equally spaced curved bilayers forming a set of concentric hollow cylinders in a space-filing arrangement. Moreover, we find that the bilayers composing the walls of the tubes are equally spaced but that the inter-bilayer distance is much larger than expected as a consequence of the highly charged system. Upon dilution of the microtubes, swelling of the multi-walled structure of the microtubes occurs. Furthermore, the response of the system to variations in temperature was probed. The experimental data can be modelled with a simple concentric cylinder model. It is extraordinary that one technique, synchrotron SAXS, is capable of elucidating *in situ* the structure of a system while bridging so many orders of spatial scales. In the forthcoming studies the application of SAXS to the co-assembly of colloids and SDS@2β-CD microtubes will be investigated.

Acknowledgements

This work was supported by the Nederlandse Organisatie voor Wetenschappelijk Onderzoek (NWO) and the European Synchrotron Radiation Facility (ESRF). F. Chang and I. Rehor are thanked for their help during the SAXS measurements.

References

1. G. M. Whitesides & B. Grzybowski. Self-assembly at all scales. *Science* **2002**, *295*, 2418–2421.

2. W. H. Roos, R. Bruinsma & G. J. L. Wuite. Physical virology, *Nat. Phys.* **2010**, *6*, 733–743.
3. J. A. A. W. Elemans, A. E. Rowan & R. J. M. Nolte. Mastering molecular matter. Supramolecular architectures by hierarchical self-assembly, *J. Mater. Chem.* **2003**, *13*, 2661–2670.
4. Y. Liu, D. Luo & T. Wang. Hierarchical structures of bone and bioinspired bone tissue engineering, *Small* **2016**, *12*, 4611–4632.
5. U. G. K. Wegst, H. Bai, E. Saiz, A. P. Tomsia & R. O. Ritchie. Bioinspired structural materials, *Nat. Mater.* **2015**, *14*, 23–36.
6. L. R. Meza, A. J. Zelhofer, N. Clarke, A. J. Mateos, D. M. Kochmann & J. R. Greer. Resilient 3D hierarchical architected metamaterials, *Proc. Natl. Acad. Sci.* **2015**, *112*, 11502–11507.
7. S. A. Jenekhe & X. L. Chen. Self-assembly of ordered microporous materials from rod-coil block copolymers, *Science* **1999**, *283*, 372–375.
8. Y. He, T. Ye, M. Su, C. Zhang, A. E. Ribbe, W. Jiang & C. D. Mao. Hierarchical self-assembly of DNA into symmetric supramolecular polyhedra, *Nature* **2008**, *452*, 198–202.
9. A. Aggeli, M. Bell, N. Boden, J. N. Keen, P. F. Knowles, T. C. B. McLeish, M. Pitkeathly & S. E. Radford. Responsive gels formed by the spontaneous self-assembly of peptides into polymeric β-sheet tapes, *Nature* **1997**, *386*, 259–262.
10. L. Jiang, Y. Peng, Y. Yan & J. Huang. Aqueous self-assembly of SDS@2β-CD complexes: lamellae and vesicles, *Soft Matter* **2011**, *7*, 1726–1731.
11. Y. Yan, L. Jiang & J. Huang. Unveil the potential function of CD in surfactant systems, *Phys. Chem. Chem. Phys.* **2011**, *13*, 9074–9082.
12. L. Jiang, M. Deng, Y. Wang, D. Liang, Y. Yan & J. Huang. Special effect of β-cyclodextrin on the aggregation behavior of mixed cationic/anionic surfactant systems. *J. Phys. Chem. B* **2009**, *113*, 7498–7504.
13. L. Jiang, Y. Yan & J. Huang. Versatility of cyclodextrins in self-assembly systems of amphiphiles. *Adv. Colloid Interface Sci.* **2011**, *169*, 13–25.
14. L. Jiang, Y. Peng, Y. Yan, M. Deng, Y. Wang & J. Huang. "Annular Ring" microtubes formed by SDS@2β-CD complexes in aqueous solution, *Soft Matter* **2010**, *6*, 1731–1736.

15. F. Gobeaux, N. Fay, C. Tarabout, F. Meneau, C. Mériadec, C. Delvaux, J. Cintrat, C. Valéry, F. Artzner & M. Paternostre. Experimental observation of double-walled peptide nanotubes and monodispersity modeling of the number of walls, *Langmuir* **2013**, *29*, 2739–2745.

16. P. van Vaerenbergh, J. Leonardon, M. Sztucki, P. Boesecke, J. Gorini, L. Claustre, F. Sever, J. Morse & T. Narayanan. An upgrade beamline for combined wide, small and ultra small-angle x-ray scattering at the ESRF, *Proceedings of the 12th International Conference on Synchrotron Radiation Instrumentation (SRI2015)*, AIP Conference Proceedings **2016**, *1741*, 030034.

17. B. E. Warren. X-ray diffraction in random layer lattices, *Phys. Rev.* **1941**, *59*, 693–698.

18. J. K. Kjems, L. Passell & H. Taub. Neutron scattering study of nitrogen absorbed on basel-plane-oriented graphite, *Phys. Rev. B* **1976**, *13*, 1446–1462.

19. P. M. Chaikin & T. C. Lubensky. *Principles of Condensed Matter Physics*, Cambridge University Press, **2000**.

20. G. S. Manning. Counterion condensation on charged spheres, cylinders and planes, *J. Phys. Chem. B* **2007**, *111*, 8554–8559.

21. E. Paineau, M. M. Krapf, M. Amara, N. V. Matskova, I. Dozov, S. Rouziere, A. Thill, P. Launois & P. Davidson. A liquid-crystalline hexagonal columnar phase in higly-dliute suspensions of imogolite nanotubes, *Nat. Commun.* **2016**, *7*, 10271.

22. C. Zhou, X. Cheng, Y. Yan, J. Wang & J. Huang. Reversible transition between SDS@2β-CD microtubes and vesicles triggered by temperature. *Langmuir* **2014**, *30*, 3381–3386.

PART II

Photo-Responsive Colloids

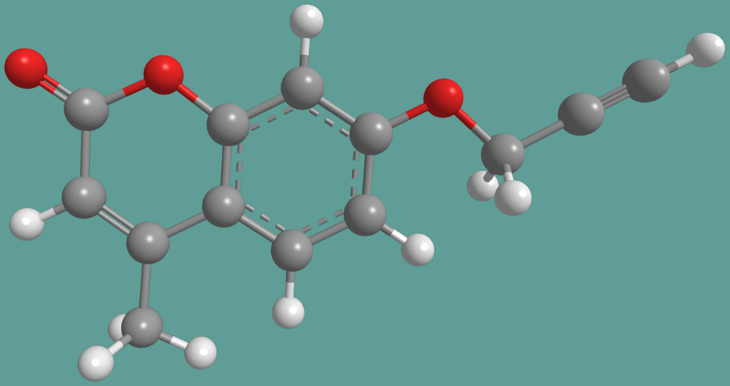

3

Reversible Flocculation of Coumarin-Modified Colloids via Switchable Photo-Crosslinking in Water

Abstract

In this Chapter the synthesis of coumarin-modified colloids that can photo-crosslink triggered by UV-light is disclosed. First, cross-linked polystyrene particles were prepared that were used as seeds to produce brominated colloidal initiators. Surface-initiated atom transfer radical polymerization (SI-ATRP) was then exploited to graft hydrophilic polymer hairs from the colloid surfaces. Photo-responsive coumarin moieties were finally introduced at the end of these hairs following a nucleophilic substitution and a Azide-Alkyne Huisgen cycloaddition reaction. Upon irradiation with UV-light, covalent clicking of single spheres results in the formation of clusters in aqueous dispersion.

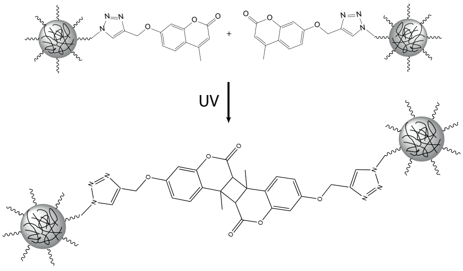

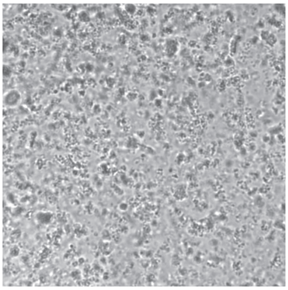

3.1 Introduction

Coumarin is a photo-responsive molecule that can reversibly photo-dimerize upon irradiation with UV-light. Coumarin was first isolated in 1820 by recrystallization of crystals from the tonka bean in ethanol.[1] The name coumarin is derived from the Caribbean word *coumarou* which means tonka tree.[1] It took nearly half a century before the structure of coumarin was elucidated and the molecular formula was known to be $C_9H_6O_2$,[1] see Figure 3.1a. The coumarin family consist of more than 1000 derivatives of which many also exhibit fluorescence and are thus often used as fluorescent dyes.[2] As almost all coumarin derivatives are oxygenated at the C-7 position, 7-hydroxycoumarin, also known as umbelliferone, is generally considered the parent of the more complex coumarins,[1,2] see Figure 3.1b.

Whereas the photo-dimerization reaction of coumarin was discovered in 1902 by Ciamician and Silber, the reverse reaction, photo-cleavage, was only discovered in 1960 by Schenck and co-workers.[2] Consequently, the photo-scission reaction has not been studied as extensively. A $[2\pi + 2\pi]$ cycloaddition reaction occurs when two coumarin molecules are irradiated with light from the UVA region (320-400 nm) of the electromagnetic spectrum.[3] The dimer consists of a cyclobutane ring that can be cleaved with light from the UVC region (200-280 nm).

Coumarins have been used to produce self-healing polymers,[4] to synthesize photo-responsive nanomaterials that function as drug carriers,[5] to strengthen silica aerogels,[6] to induce the reversible self-assembly of gold nanoparticles,[7] in polymeric liquid crystals,[8] to create photoactive surfaces,[9,10] and to stabilize polymer micelles,[11] to name a few examples.

In this Chapter, we report a synthetic strategy for photo-responsive colloidal spheres using coumarin. To this end, we first synthesized cross-linked polystyrene colloidal initiators from which hydrophilic polymer hairs could be grafted from the surface via surface-initiated atom transfer radical polymerization. After a nucleophilic substitution reaction, sterically stabilized spheres end-capped with azides are obtained. Finally, a Huisgen click reaction is performed to attach alkyne-coumarin, a synthesized coumarin derivative, onto the particles.

3.2 Experimental Methods

3.2.1 Materials. Styrene (St, 99%), divinylbenzene (DVB, 55% mixture of isomers, technical grade), 2-bromoisobutyryl bromide (BiBB, 98%), 2-hydroxyethyl acrylate (HEA, 96%, contains 200-650 ppm monomethyl ether hydroquinone as inhibitor),

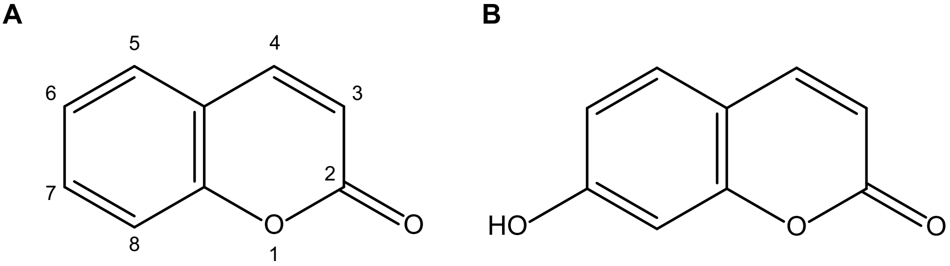

Figure 3.1: Structure of coumarin. (a) Coumarin with atoms numbered according to *IUPAC*. (b) 7-hydroxycoumarin or umbelliferone.

sodium sulphate (Na_2SO_4, ACS reagent, ≥99%, anhydrous), copper bromide (Cu(I)Br, 98%, stored under inert atmosphere), *N,N,N',N',N"*-pentamethyldiethylenetriamine (PMDTA, 99%), dimethylformamide (DMF, ≥99%), bromotris(triphenylphosphine) copper(I) ($Cu(PPh_3)_3Br$, 98%), *N,N*-diisopropyl-ethylamine (DIPEA, ≥98%), propargyl bromide (Prp-Br, 80 wt% solution in toluene) and sodium dodecyl sulphate (SDS, >97%) were obtained from Sigma Aldrich. Potassium persulphate (KPS, >99% for analysis), sodium bisulfite ($NaHSO_3$, ACS reagent), pyridine (>99%) and 7-hydroxy-4-methylcoumarin (97%) were purchased from Acros Organics. Methanol (MeOH, exceeds ACS specifications) was obtained from J.T. Baker, and dichloromethane (DCM, peptide synthesis) was obtained from Biosolve. Sodium azide (NaN_3, 99%) was obtained from VWR. All chemicals were used as received. The water used for all syntheses was purified using a Milli-Q water purification system.

3.2.2 Synthesis of 2-(2-bromoisobutyryloxy)ethyl acrylate (BIEA). The synthesis of BIEA was adapted from Matyjaszewski et al.[12] A solution of HEA (40 mL, 348 mmol) and pyridine (31 mL, 383 mmol) in DCM (250 mL) was stirred and cooled in an ice bath. Under nitrogen atmosphere, a solution of BiBB (36.45 mL, 348 mmol) in DCM (50 mL) was added dropwise over the course of 1 hour. During the addition a white precipitate was formed (HBr-pyridine). After complete addition of the BiBB solution, the reaction mixture was stirred an additional 3 hours at room temperature. The precipitate was filtered off and DCM was evaporated under reduced pressure. A yellow oil and additional precipitate was formed. The additional precipitate was filtered off and washed with DCM. The DCM from washing and the yellow oil were combined and washed with water (three times, 50 mL per washing step). The oil phase was dried over Na_2SO_4 and finally the DCM was evaporated under reduced pressure. The resulting yellow oil was distilled to complete the purification procedure yielding a colourless oil. ^{1}H-NMR (400 MHz, $CDCl_3$, δ): 6.43 (d, 1H), 6.14 (dd, 1H), 5.85 (d, 1H), 4.4 (s, 4H), 1.9 (s, 6H).

3.2.3 Synthesis of Brominated Colloidal Initiators (CPs-Br). Cross-linked polystyrene particles (CPs) were synthesized using a standard emulsion polymerization method described in literature.[13,14] A 250 mL round-bottom flask equipped with magnetic stir bar was placed in an oil bath at 80 °C. Water (100 mL) was charged into the reactor and allowed to reach the bath temperature. St (11.6 mL, 100 mmol), DVB (0.35 g, 2.4 mmol), and SDS (62.5 mg, 0.2 mmol) dissolved in water (25 mL) were added. The complete mixture was heated up to the temperature of the bath. Finally, the addition of KPS (0.39 g, 1.4 mmol dissolved in 18.8 mL water) initiated the polymerization. The reaction was allowed to continue for 24 hours at 80 °C. The resulting latex had a solid content of 6.7% (measured gravimetrically).

The synthesized particles were used as seeds in the second step, in which BIEA was polymerized onto the surface of the prepared CPs particles.[15] To this end, as-prepared seed dispersion (CPs, 12.5 mL) and water (12.5 mL) were introduced into a 50 mL round-bottom flask equipped with a magnetic stir bar. The dispersion was degassed with nitrogen for 30 minutes. Subsequently, a mixture consisting of St (0.5 mL, 4.4 mmol), DVB (10 μL, 0.07 mmol) and BIEA (0.4 g, 1.5 mmol) was injected under inert atmosphere. After 5 minutes of stirring, polymerization of the newly added monomers was initiated by the addition of a degassed, aqueous KPS solution (16 mg, 0.06 mmol in 2.5 mL water). The polymerization was allowed to run for 6 hours at 70 °C after which the reaction was quenched by removing the flask from the oil bath. The particles were washed with water three times by means of centrifugation and redispersion cycles.

3.2.4 Grafting of Poly(HEA) Brushes from CPs-Br using SI-ATRP (CPs-p(HEA)-Br). Cu(I)Br (6.9 mg, 0.05 mmol) and HEA (69 μL, 0.60 mmol) were mixed with a MeOH/H_2O mixture (7:3, v/v) (0.5 mL) in an oven-dried Schlenk flask, resulting in a light green mixture (note: the copper bromide salt does not completely dissolve in the reaction medium). The obtained mixture was degassed by evacuation and refilling with nitrogen (three cycles). Subsequently, PMDTA (29 μL, 0.14 mmol) was injected, resulting in the appearance of a blue/green colour and complete solubilization of the copper bromide salt. The degassing procedure was repeated once more to further exclude the presence of oxygen in the obtained catalyst/monomer reaction mixture.

In a separate Schlenk flask, the CPs-Br colloids dispersed in a 7:3 (v/v) MeOH/H_2O mixture (0.5 mL, 2 wt%) were degassed by evacuation and refilling with nitrogen (three cycles). After degassing, the dispersion was injected into the monomer/catalyst mixture under inert atmosphere. The resulting reaction mixture had a white/green appearance. The ATRP reaction was allowed to run for 40 minutes at room temperature, after which the reaction was terminated by exposure to air, yielding an intense blue colour. The particles were washed three times with the MeOH/H_2O mixture, 10 times with a 50 mM aqueous $NaHSO_3$ solution and finally three times with water. The $NaHSO_3$ solution was used to facilitate the removal of the copper catalyst. After the complete washing procedure, a stable colloidal dispersion was obtained.

3.2.5 Nucleophilic Substitution of Halogen Chain Ends of Grafted p(HEA) Hairs with Sodium Azide (CPs-p(HEA)-N_3). NaN_3 (4.5 mg, 0.07 mmol) was dissolved in DMF (0.5 mL). To this solution, a dispersion containing the p(HEA) grafted colloids in DMF was added (0.5 mL, 1 wt%). The obtained reaction mixture was allowed to stir for 24 hours at 70 °C. After this period, the particles were washed with DMF (three times) and water (three times) to remove excess NaN_3.

3.2.6 Synthesis of 4-Methyl-7-prop-2-ynoxychromen-2-one (Alkyne-Coumarin). The synthesis was adapted from Behl et al.[16] 4-methyl-7-hydroxy-coumarin (2.5 g, 14.3 mmol) and K_2CO_3 (8.18 g, 59 mmol) were transferred into a 100 mL Schlenk flask containing a magnetic stir bar. The flask was subsequently evacuated and refilled with nitrogen gas three times. A separate Schlenk flask containing dry DMF (stored over freshly regenerated mole sieves of 4 Å was evacuated and refilled with nitrogen (three cycles). Subsequently, the dried DMF (40 mL) was transferred to the flask containing coumarin and K_2CO_3, yielding a clear, yellow solution after stirring for 10 minutes. While stirring, propargyl bromide (2.6 mL, 23.3 mmol) was injected via a septum resulting in a slightly darker yellow reaction mixture. Stirring was continued for 72 hours at room temperature.

The obtained product was purified by precipitation of the crude mixture into water (100 mL). The solid was filtered and washed with water four times. The resulting solid was dried under vacuum for 2 hours at 40 °C and recrystallized from methanol. The product was stored in the freezer. ^{1}H-NMR (400 MHz, $CDCl_3$, δ): 7.5 (m, 1H), 6.9 (m, 2H), 6.2 (d, 1H), 4.8 (d, 2H), 2.6 (t, 1H), 2.4 (d, 3H). FT-IR: $\nu = 3300\,\text{cm}^{-1}$

(diagnostic signal used to confirm successful modification of coumarin precursor). UV-vis (ethanol): $\lambda_{max} = 320\,\text{nm}$.

3.2.7 Coupling of Alkyne-Coumarin to CPs-p(HEA)-N_3 using Click Chemistry (CPs-p(HEA)-coumarin). $Cu(PPh_3)_3Br$ (6.25 mg, 6.7 μmol) was introduced into a 10 mL round-bottom flask equipped with a magnetic stir bar. To this, DIPEA (13 μL, 75 μmol) and alkyne-coumarin (0.5 mL of a DMF stock solution, concentration = 4.9 mg/mL, 23 mmol/mL) were added. Finally, a dispersion containing CPs-p(HEA)-N_3 in DMF (0.25 mL, 1 wt%) was injected. The reaction was allowed to run for 24 hours under gentle stirring at 70 °C. After this period, the colloids were washed with DMF.

3.2.8 Irradiation Experiments. A 14 W low-pressure mercury lamp emitting UV-light with a wavelength of 365 nm was used to crosslink the photo-responsive colloids. Typically, samples were irradiated for 24 hours. Control samples were enclosed in aluminium foil to prevent the penetration of UV-light. A 6 W low-pressure mercury lamp emitting UV-light with a wavelength of 254 nm was used to cleave the crosslinked dimers. Samples were irradiated for a maximum of ten minutes.

3.2.9 Characterization. IR spectra were obtained using a Perkin Elmer FT-IR/FIR Frontier Spectrometer in attenuated total reflectance (ATR) mode. The measurements were carried out on powders (obtained by drying the corresponding particle dispersion).

Transmission electron microscopy (TEM) pictures were taken with a Philips Tecnai10 electron microscope typically operating at 100 kV. Bright field images were recorded using a SIS Megaview II CCD camera. The samples were prepared by drying a drop of diluted aqueous particle dispersion on top of polymer coated copper grids.

Scanning electron microscopy (SEM) pictures were taken with a FEI XL30 FEG scanning electron microscope operating at 5-15 kV. SEM samples were prepared by sticking a TEM grid coated with colloidal particles on a stub using a conductive carbon sticker, which was coated with a platinum layer of typically 6 nm.

Dynamic light scattering (DLS) was performed using a Malvern Zetasizer Nano instrument using highly diluted aqueous dispersions at 25 °C. The DLS measurements were taken in 10 runs of 10-15 individual measurements in backscatter mode (173°). The hydrodynamic particle dimensions are based on the number distributions with their corresponding polydispersity index (PdI). The dimensionless PdI is calculated from the mean μ and standard deviation σ in hydrodynamic diameter according to $\mathrm{PdI} = (\sigma/\mu)^2$.

^{1}H-NMR spectra were recorded using a Varian MRF400 400 MHz NMR machine. $CDCl_3$ was employed as solvent.

UV-vis spectra were recorded on a Perkin-Elmer Lambda-35 spectrophotometer from $\lambda = 450$ to $\lambda = 250$ nm with 1.0 nm intervals. Helma QS quartz cuvettes with a path length of 10 mm were used. Sample concentrations were chosen such that the maximum absorption remained below 2.5.

Optical microscopy images were obtained using a Nikon Eclipse Ti-E inverted microscope equipped with a Hamamatsu Orca Flash 4.0 V2 Digital Camera. A Nikon CFI Apo TIRF objective (100× magnification, N.A. 1.49) was used. Pictures were recorded in bright field mode. Samples were prepared by placing 5-10 μL dispersion between a microscope slide (76×26 mm, Menzel-Gläser) and a cover slip (22×22×0.17 mm, Menzel-Gläser) with two cover glasses as spacers (22×22×0.10 mm, VWR). Cells were sealed with glue (Norland optical adhesive 81) that was cured with UV-light (365 nm, 6 W UVP UVGL-58 lamp). Alternatively, hollow glass tubes (0.1×2×50 mm, VitroCom) were filled with particle dispersions by capillary action and also sealed with UV curing optical adhesive.

3.3 Results and Discussion

3.3.1 Photochemistry of Alkyne-Coumarin. Alkyne-coumarin was synthesized by treating 4-methyl-7-hydroxycoumarin with propargyl bromide. The coumarin precursor with a methyl group was chosen specifically as Chen et al.[17] had reported that the presence of the methyl group increases the speed of the photodimerization reaction up to 200 times. Unlike its precursor, alkyne-coumarin is hydrophobic in nature, which made it impossible to prepare an aqueous dispersion of pure alkyne-coumarin and thus to determine the photochemical properties in water, the solvent that was employed for the bulk experiments. Therefore, the photochemistry of alkyne-coumarin was studied in ethanol. Prior to irradiation, an absorption peak around 320 nm can be observed originating from the conjugated π-system[2,18,19] of the aromatic rings of coumarin (see Figure 3.2a). Upon irradiation with $\lambda = 365$ nm a significant decrease in this absorption peak can be seen. This is consistent with the disappearance of the double bonds of coumarin due to a $[2\pi + 2\pi]$ cycloaddition formation of a cyclobutane ring between two alkyne-coumarin molecules (see Figure 3.2b). The coumarin absorption band can be (partially) regenerated by irradiating with a wavelength of 254 nm for ten minutes, resulting in the photo-cleavage of the coumarin dimers. However, under

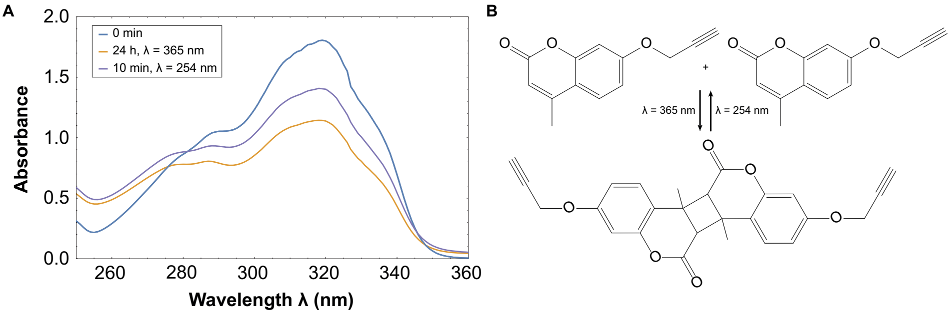

Figure 3.2: Photochemistry of alkyne-coumarin. (a) UV-vis spectra of alkyne-coumarin in ethanol. The synthesized coumarin derivative photo-dimerizes upon irradiation with long wavelengths of UV-light. Decrease in the peak around 320 nm indicates the formation of a cyclobutane ring between two coumarin molecules. The reverse process, *i.e.* photo-cleavage, occurs upon irradiation with short wavelengths of UV-light. (b) Schematic representation of photo-dimerization and photo-cleavage of coumarin molecules.

prolonged irradiation with short wavelengths of light, photodimerization occurs again leading to another decrease in the absorption band.[19]

3.3.2 Synthesis of Photo-Responsive Spheres. An overview of the synthesis route towards photo-responsive colloidal spheres can be found in Figure 3.3. Cross-linked polystyrene spheres were synthesized via a conventional emulsion polymerization method yielding spheres with a diameter of 386 nm with a polydispersity of 6.7% as determined with TEM (see Figure 3.5a). DLS measurements revealed an apparent hydrodynamic diameter of 406 nm with a corresponding polydispersity index of 0.036. Seeded emulsion polymerization of BIEA onto the surface of the synthesized CPs spheres resulted in brominated colloidal initiators with an apparent hydrodynamic diameter of 464 nm and a PdI of 0.095. SI-ATRP was then employed to graft well-defined hydrophilic polymeric hairs from the surface of the initiator particles, providing steric stabilization and spacers. The ATRP reaction was quenched to obtain polymer brushes of desired length, end-functionalized with bromine atoms. DLS showed a clear increase in apparent hydrodynamic diameter (529 nm), providing evidence for successful polymer grafting. The halogen atoms could then be substituted with azides to which alkyne-coumarin molecules could be attached via the efficient and robust click chemistry pathway.[20]

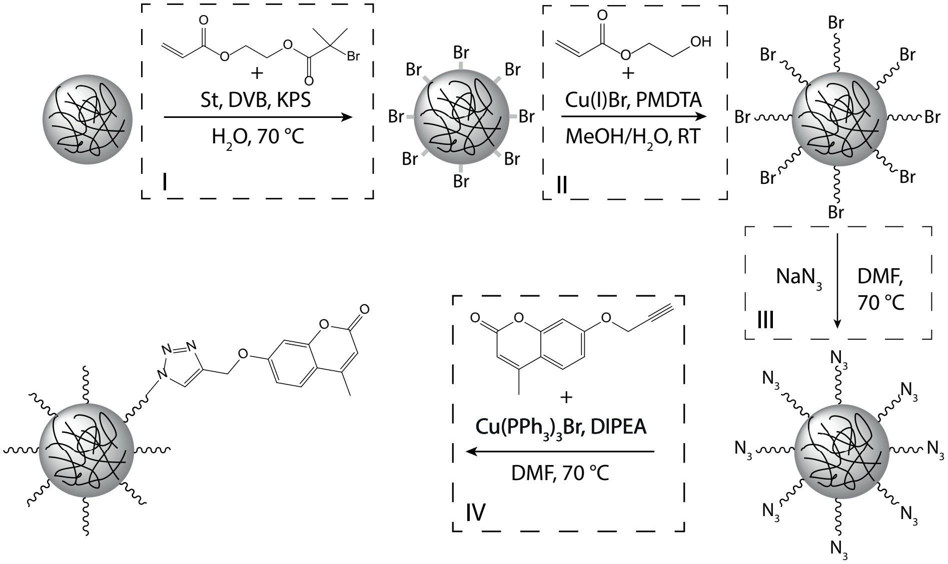

Figure 3.3: Schematic overview of the synthesis route towards photo-responsive colloidal particles. (I) Seeded emulsion polymerization of cross-linked polystyrene particles in the presence of BIEA, St and DVB. (II) Polymeric HEA hairs are grafted from the surface of brominated colloidal initiators using SI-ATRP. (III) Halogen chain ends of p(HEA) are substituted by azides via a nucleophilic substitution reaction. (IV) Alkyne-coumarin is coupled to the azide chain ends via the Huisgen click reaction.

Using IR spectroscopy, each step of the synthesis was verified, see Figure 3.3. Successful coupling of BIEA to the surface of the polystyrene particles was confirmed by the C=O vibration of BIEA at 1732 cm^{-1}. The presence of p(HEA) led to an increase in this vibration due to pending ester functionalities of grafted polymers and an additional band at 3200 cm^{-1} of the -OH groups. Azido-end-functionalized polymers were successfully formed as indicated by the free azide vibration at 2096 cm^{-1}. Finally, the disappearance of this signal confirmed the effectiveness of the coumarin coupling to the chain-ends of the grafted polymers.

TEM images revealed that the obtained photo-responsive polystyrene spheres were in fact hollow (see Figure 3.5b). The polystyrene spheres were cross-linked with DVB during the synthesis to make the particles resistant against organic solvents. Nevertheless, the cross-linking density appeared to be too low in the centre of the particles. After two functionalization steps in DMF, which is capable of dissolving

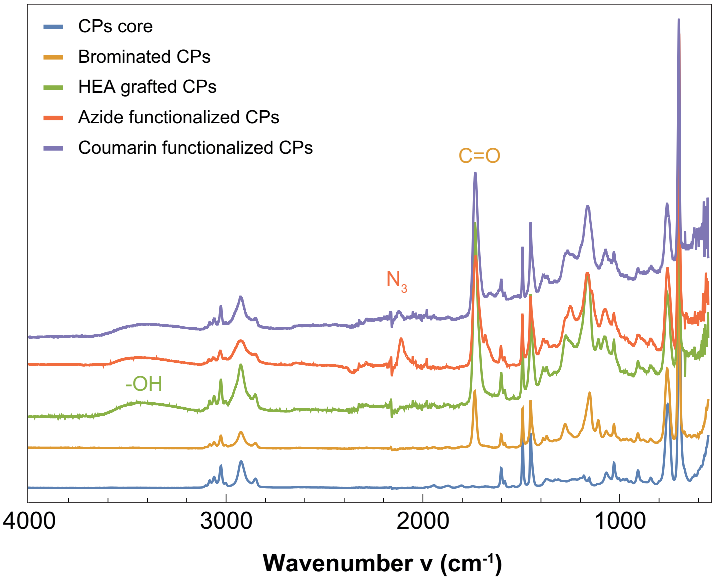

Figure 3.4: IR spectra of the synthesized particles. From bottom to top: cross-linked polystyrene core particles (blue), brominated core-shell polystyrene particles (yellow), HEA grafted polystyrene spheres (green), polystyrene spheres with azide terminated HEA hairs (orange) and the final coumarin-functionalized photo-responsive colloids (purple). Characteristic signals are labelled with the corresponding bond/functional group. All spectra are normalized to the polystyrene signal at 699 cm^{-1} and are offset vertically for the sake of clarity.

(linear) polystyrene, the synthesized photo-responsive colloids became hollow. We used this to our advantage as the partially hollow colloids tend to sediment slower and consequently allow for easier capturing in the cylindrically confining environment of the microtubes (see Chapter 5).

3.3.3 Bulk Behaviour. Having successfully synthesized coumarin-modified colloidal particles, the behaviour in bulk was investigated. Samples consisting of aqueous dispersions of the colloids with varying concentrations were prepared and irradiated for some time. Each sample was accompanied by a control sample, that was wrapped in aluminium foil to prevent UV-light from penetrating the sample. For 5 wt% colloidal particles in dispersion, aggregation can be observed within 24 hours of UV exposure whereas after 60 hours almost the entire sample is aggregated, see Figure 3.6. As

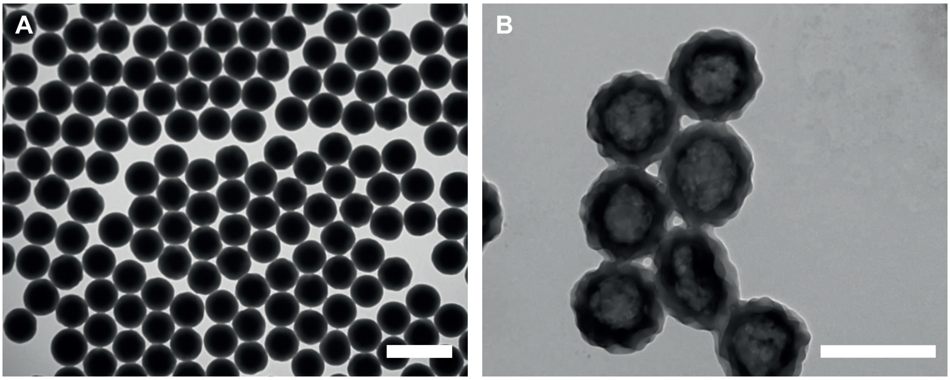

Figure 3.5: TEM images. (a) Cross-linked polystyrene particles before the functionalization steps in DMF (scale bar is 1 μm). (b) Two reactions of 24 hours in DMF led to hollow polystyrene particles that collapsed under the high vacuum in the TEM (scale bar is 0.5 μm).

expected, the control samples were unaffected. These bulk experiments prove that the synthesized colloids indeed are photo-responsive and that the surface-immobilized coumarin derivatives can still undergo photo-dimerization.

The photo-crosslinking of surface immobilized coumarin derivatives is reaction limited. Furthermore, it takes a significant amount of time for the particles to meet by diffusion and not every encounter ultimately leads to a covalent bond between particles. The frequency with which diffusing spheres A encounter a stationary sphere B, $J_{A\to B}$, is given by:[21]

$$J_{A\to B} = 4\pi r^2 D \frac{d\rho}{dr}. \tag{3.1}$$

Here, r is the centre-to-centre distance between the spheres, D is the translational diffusion coefficient of a sphere, and ρ is the particle number density. For stationary diffusion, $J_{A\to B}$ is constant and Equation 3.1 yields:

$$J_{A\to B} \int_{\infty}^{2R} \frac{dr}{r^2} = 4\pi D \int_{\rho_\infty}^{0} d\rho. \tag{3.2}$$

Here, the boundary condition is that at distance $r = 2R$, the concentration of free spheres is zero. Evaluating the integrals yields:

$$J_{A\to B} = 8\pi D R \rho_\infty, \tag{3.3}$$

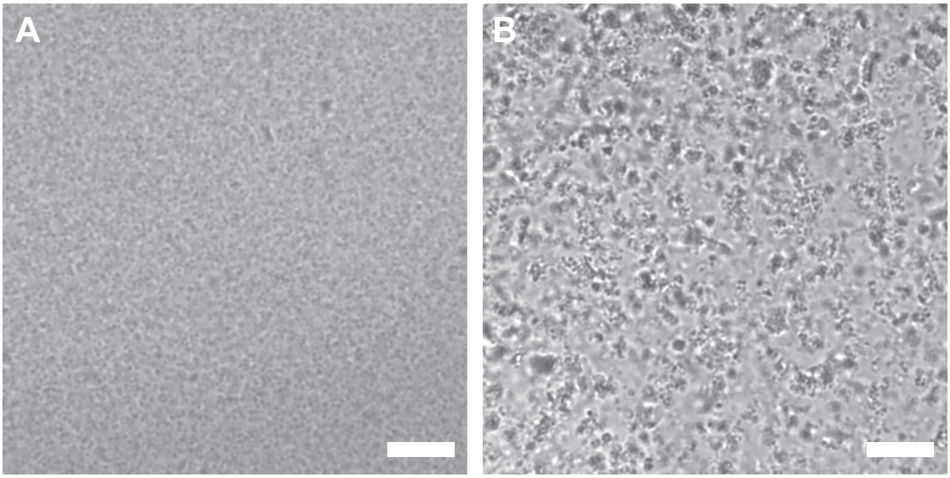

Figure 3.6: Polystyrene spheres with surface-immobilized coumarin derivatives in 5 wt% aqueous dispersion. (a) Well-dispersed particles were observed prior to UV irradiation. The particle stability was maintained over the course of months by storing the dispersions on a roller table to prevent sedimentation-induced aggregation. (b) After 60 hours of irradiation with UV-light ($\lambda = 365\,\text{nm}$), clusters are formed throughout the entire sample due to photo-dimerization of coumarin on neighbouring particles. Scale bars are $5\,\mu$m.

where ρ_∞ is the bulk particle number density. Using the Stokes-Einstein diffusion coefficient $D = k_\text{B}T/6\pi\eta R$ and the volume fraction $\phi = \frac{4}{3}\pi R^3 \rho$, we obtain:

$$J_{A\to B} = \frac{\phi k_\text{B} T}{\pi R^3 \eta}. \tag{3.4}$$

The corresponding time between two Brownian encounters is the inverse of $J_{A\to B}$ and is thus given by:

$$\tau_B = \frac{\pi R^3 \eta}{\phi k_\text{B} T}. \tag{3.5}$$

For spheres with a radius of $\approx 0.25\,\mu$m and a volume fraction of 1 % in water (as used throughout this Chapter), τ_B is on the order of 10^2 s. Equation 3.5 also shows that an increase in concentration of the particles or a decrease in the viscosity η of the solvent both lead to effectively more encounters and thus a decrease in the required UV exposure time.

3.4 Conclusions and Outlook

Photo-crosslinkable colloids were successfully synthesized as demonstrated via infrared spectroscopy, dynamic light scattering and microscopy techniques. Our synthesis route yields photo-responsive colloidal polystyrene spheres that are sterically stabilized with polymer hairs and end-functionalized with coumarin molecules. By exposure to UV-light covalent bonds between neighbouring colloids were evidently formed, as the photo-responsive colloids clearly showed the expected photo-induced aggregation in bulk. These particles can be incorporated inside microtubes where the coumarin molecules act as a chemical glue holding the spheres in place even after dissolution of confining tubes. The expectation is that bonds can form more easily inside the microtubes as the cylindrical confinement minimizes the distance between the colloidal spheres.

Acknowledgements

Bas van Ravensteijn is acknowledged for introducing us to SI-ATRP and Kanvaly Lacina for synthesizing alkyne-coumarin. Carla Fernández Rico is thanked for performing some of the experiments described here.

References

1. R. D. H. Murray, J. Méndez & S. A. Brown. *The Natural Coumarins: Occurrence, Chemistry and Biochemistry*, John Wiley & Sons Ltd, **1982**.
2. S. R. Trenor, A. R. Shultz, B. J. Love & T. E. Long. Coumarins in polymers: From light harvesting to photo-cross-linkable tissue scaffolds, *Chem. Rev.* **2004**, *104*, 3059–3077.
3. S. R. Trenor, T. E. Long & B. J. Love. Photoreversible chain extension of poly(ethylene glycol), *Macromol. Chem. Phys.* **2004**, *205*, 715–723.
4. M. Abdallh, M. T. W. Hearn, G. P. Simon & K. Saito. Light triggered self-healing of polyacrylate polymers crosslinked with 7-methacryloyoxycoumarin crosslinker, *Polym. Chem.* **2017**, *8*, 5875–5883.
5. J. W. Chung, K. Lee, C. Neikirk, C. M. Nelson & R. D. Priestley. Photoresponsive coumarin-stabilized polymeric nanoparticles as a detectable drug carrier, *Small* **2012**, *8*, 1693–1700.

6. K. M. Frederick, D. J. Boday, J. Unangst, R. J. Stover, Z. Li, S. Budy & D. A. Loy. Photochemical strengthening of silica aerogels modified with coumarin groups, *J. Non-Cryst. Solids* **2016**, *432*, 189–195.
7. H. Huibin, F. Miao, C. Qidi, Z. Xinqi & Z. Hongbing. Light-induced reversible self-assembly of gold nanoparticles surface-immobilized with coumarin ligands, *Angew. Chem. Int. Ed.* **2016**, *55*, 936–940.
8. F. P. La Mantia. *Thermotropic Liquid Crystal Polymer Blends*, CRC Press, **1993**.
9. W. Li, V. Lynch, H. Thompson & M. A. Fox. Self-assembled monolayers of 7-(10-thiodecoxy)coumarin on gold: Synthesis, characterization, and photodimerization, *J. Am. Chem. Soc.* **1997**, *119*, 7211–7217.
10. Y. Tian, E. Akiyama & Y. Nagase. Liquid crystalline cyclic tetramethyltetrasiloxanes containing coumarin moieties, *J. Mater. Chem.* **2003**, *13*, 1253–1258.
11. J. Jiang, B. Qi, M. Lepage & Y. Zhao. Polymer micelles stabilization on demand through reversible photo-cross-linking, *Macromolecules* **2007**, *40*, 790–792.
12. K. Matyjaszewski, S. G. Gaynor, A. Kulfan & M. Podwika. Preparation of hyperbranched polyacrylates by atom transfer radical polymerization. 1 Acrylic AB* monomers in “living” radical polymerizations, *Macromolecules* **1997**, *30*, 5192–5194.
13. D. J. Kraft, W. S. Vlug, C. M. van Kats, A. van Blaaderen, A. Imhof & W. K. Kegel. Self-assembly of colloids with liquid protrusions, *J. Am. Chem. Soc.* **2009**, *131*, 1182–1186.
14. B. G. P. van Ravensteijn, M. Kamp, A. van Blaaderen & W. K. Kegel. General route toward chemically anisotropic colloids, *Chem. Mater.* **2013**, *25*, 4348–4353.
15. B. G. P. van Ravensteijn & W. K. Kegel. Versatile procedure for site-specific grafting of polymer brushes on patchy particles via atom transfer radical polymerization (ATRP), *Polym. Chem.* **2016**, *7*, 2858–2869.
16. G. Behl, M. Sikka, A. Chhikara & M. Chopra. PEG-coumarin based biocompatible self-assembled fluorescent nanoaggregates synthesized via click reaction and study of their aggregation behaviour, *J. Colloid Interface Sci.* **2014**, *416*, 151–160.
17. Y. Chen & C. Chou. Reversible photodimerization of coumarin derivatives dispersed in poly(vinyl acetate), *J. Polym. Sci. Part A: Polym. Chem.* **1995**, *33*, 2705–2714.

18. C. Cardenas-Daw, A. Kroeger, W. Schaertl, P. Froimowicz & K. Landfester. Reversible photocycloadditions: A powerful tool for tailoring (nano)materials, *Macromol. Chem. Phys.* **2012**, *213*, 144–156.
19. N. W. Mal, M. Fujiwara & Y. Tanaka. Photocontrolled reversible release of guest molecules from coumarin-modified mesoporous silica, *Nature* **2003**, *421*, 350–353.
20. H. C. Kolb, M. G. Finn & K. B. Sharpless. Click chemistry: Diverse chemical function from a few good reactions, *Angew. Chem. Int. Ed.* **2001**, *40*, 2004–2021.
21. A. P. Philipse. *Brownian Motion: Elements of Colloid Dynamics*, Springer Nature Switzerland AG, **2018**.

4

Magnetisable Chains of Coumarin-Modified Spheres

Abstract

A method is presented for the synthesis of rodlike chains of superparamagnetic silica spheres. Silica particles are functionalized with coumarin molecules following an adaptation of the synthetic methodology outlined in Chapter 3 for polystyrene spheres. An external magnetic field is applied to align the photo-responsive and superparamagnetic silica spheres, leading to the formation of linear sphere chains. Upon UV-irradiation, covalent linking of adjacent spheres results in permanent magnetisable sphere chains in bulk. To avoid clustering of spheres due to a gradient in particle concentration, a Helmholtz cube was developed that produced a homogeneous magnetic field.

4.1 Introduction

Dia- and paramagnetic materials are generally considered to be nonmagnetic due to, respectively, a very small negative or positive magnetic susceptibility.[I] Diamagnetic objects oppose the applied field and under the right conditions this repulsion can balance gravity.[1] Seemingly[II] nonmagnetic materials can thus be levitated in a magnetic field.[2] It is even possible to levitate living creatures as Geim and co-workers have famously shown using a frog.[3] Levitation of paramagnets is not possible as these materials have a net magnetic moment per atom and align, however weakly, parallel to the direction of the magnetic field.

The phrase ‘magnetic materials’ is typically used to refer to ferromagnetic solids in which the magnetic states within domains are ordered and the magnetic susceptibility is positive and much larger than one. A superparamagnetic particle has a size equal to or smaller than a single domain of a ferromagnetic solid and thus has a permanent dipole moment. Superparamagnetic nanoparticles can be suspended in liquid media to form ferrofluids but can also be incorporated in a matrix of ‘nonmagnetic’ material such as polystyrene or silica to prepare magnetic colloids.[4,5] In the absence of an external magnetic field these hybrid colloids have no net magnetization as the ordering of the dipole moments of the nanoparticles is lost due to thermal fluctuations.[6]

Numerous applications exist for colloidal suspensions of superparamagnetic nanoparticles. In liquid media, ferrofluids are employed in the separation of ores.[7] By applying a magnetic field to heavy, ‘nonmagnetic’ particles in a ferrofluid, flotation of ores with a specific density occurs at different magnetic field strengths. Biological entities such as DNA and cells can be separated from their native environment by labelling these with magnetic colloids.[8] Tuneable photonic crystals were fabricated from magnetic polymer beads.[9,10] Biomedical applications of magnetic colloids include, but are not limited to, enhancing contrast in magnetic resonance imaging (MRI),[11] drug delivery,[12] and hyperthermia treatment of cancer.[13]

In Chapter 3 we disclosed a synthesis method for photo-responsive polystyrene colloids. Here, the same methodology is applied to prepare photo-responsive and superparamagnetic silica colloids. By applying an external magnetic field, linear chains of spheres are formed. Upon irradiation with UV-light and subsequent removal of the magnetic field, permanent rodlike chains of spheres are obtained. To avoid the formation of particle aggregates, a homogeneous magnetic field is required.

[I] Magnetic susceptibility is a measure of the extent of magnetization of a material in an applied magnetic field.[1]

[II] In fact, all materials are magnetic.[2,3]

We developed a magnetic set-up consisting of parallel and coaxial coils of copper, separated by a distance equal to the radius of the coils, to generate a uniform magnetic field. These coils are known as Helmholtz coils as the German physicist Hermann von Helmholtz from the 19th century is credited[III] for their invention.[15]

4.2 Experimental Methods

4.2.1 Materials. (3-aminopropyl)triethoxysilane (APTES, ≥98%), 2-bromoisobutyryl bromide (BiBB, ≥99.5%), methanol, 2-hydroxyethyl acrylate (HEA, 96%, contains 200-650 ppm monomethyl ether hydroquinone as inhibitor), copper bromide (Cu(I)Br, 98%, stored under inert atmosphere), *N*,*N*,*N*',*N*',*N*"-pentamethyldiethylenetriamine (PMDTA, 99%), dimethylformamide (DMF, ≥99%), bromotris(triphenylphosphine) copper(I) ($Cu(PPh_3)_3Br$, 98%), and *N*,*N*-diisopropylethylamine (DIPEA, ≥ 98%) were obtained from Sigma Aldrich. Ammonia (25% solution in water) and sodium azide (NaN_3, 99%) were purchased from Fisher. Tetrahydrofuran (THF, stabilized with 0.025% BHT) and sodium bisulfite were from Acros Organics and triethylamine (TEA, ≥99.5%) from VWR. Superparamagnetic silica colloids in water with a specified diameter of 0.51 μm ± 0.03 μm and 0.96 μm ± 0.05 μm with an iron oxide content ≥30% were purchased from microParticles GmbH. All chemicals were used as received. The water used for all syntheses was purified using a Milli-Q water purification system. Alkyne-coumarin was synthesized as described in Chapter 3.

4.2.2 Synthesis of Brominated Colloidal Initiators (SPS-Br). The protocol for the coating of silica particles with a layer of amino-functionalized silica followed by attachment of bromine molecules was adapted from Wu et al.[16] and Jiang et al.[17] A dispersion of superparamagnetic silica particles (0.4 mL SPS, 2.5 wt%) in ethanol was heated to 60 °C in an oil bath. Ammonia (6 μL) was added, followed by the drop wise addition of APTES solution in ethanol (0.5 mL, 10 V%). The reaction continued for 20 hours while agitated by a magnetic stirrer. The particles were washed three times with ethanol and three times with water.

The amine-functionalized particles were dispersed in THF by centrifugation and redispersion cycles. 1 mL of the dispersion (1 wt%) was transferred to a Schlenk flask and cooled to 0 °C in an ice bath. While stirring with a magnetic stirrer, TEA (30.4 μL, 0.22 mmol) and BiBB (23.5 μL, 0.19 mmol) were added. The reaction

---

[III] It has been disputed that Helmholtz actually is the inventor of these coils; he might have only improved upon a device developed by Gaugain or Neumann.[14]

mixture was stirred for 30 minutes after which the ice bath was removed, and the reaction continued for an additional 20 hours at room temperature. The bromine-functionalized silica particles were washed three times with THF and twice with water.

4.2.3 Grafting of Poly(HEA) Brushes from SPS-Br using SI-ATRP (SPS-p(HEA)-Br). Cu(I)Br (6.9 mg, 0.05 mmol) and HEA (69 μL, 0.60 mmol) were mixed with a MeOH/H_2O mixture (7:3, v/v) (0.5 mL) in an oven-dried Schlenk flask, resulting in a light green mixture even though the copper bromide salt does not completely dissolve in the reaction medium. The obtained mixture was degassed by evacuation and refilling with nitrogen (three cycles). Subsequently, PMDTA (29 μL, 0.14 mmol) was injected, resulting in the appearance of a blue/green colour and complete solubilization of the copper bromide salt. The degassing procedure was repeated once more to further exclude the presence of oxygen in the obtained catalyst/monomer reaction mixture.

In a separate Schlenk flask, the SPS-Br colloids dispersed in a 7:3 (v/v) MeOH/H_2O mixture (0.5 mL, 2 wt%), were degassed by evacuation and refilling with nitrogen (three cycles). After degassing, the dispersion was injected into the monomer/catalyst mixture under inert atmosphere. The ATRP reaction continued for 1 hour at room temperature, after which the reaction was terminated by exposure to air. The particles were washed three times with the MeOH/H_2O mixture, ten times with a 50 mM aqueous $NaHSO_3$ solution, two times with ethanol and finally three times with water. The $NaHSO_3$ solution was used to facilitate the removal of the copper catalyst. After the complete washing procedure, a stable colloidal dispersion was obtained.

4.2.4 Nucleophilic Substitution of Halogen Chain Ends of Grafted p(HEA) Hairs with Sodium Azide (SPS-p(HEA)-N_3). NaN_3 (9 mg, 0.14 mmol) was dissolved in DMF (1.5 mL). To this solution, a dispersion containing the p(HEA) grafted magnetic colloids in DMF was added (1 mL, 1 wt%). The obtained reaction mixture was allowed to stir for 24 hours at 70 °C, after which the particles were washed with DMF (3 times) and water (3 times) to remove excess NaN_3.

4.2.5 Coupling of Alkyne-Coumarin to SPS-p(HEA)-N_3 using Click Chemistry (SPS-p(HEA)-coumarin). $Cu(PPh_3)_3Br$ (25 mg, 26.8 μmol) was introduced into a 10 mL round-bottom flask equipped with a magnetic stir bar. To this, DIPEA (52 μL, 0.3 mol) and alkyne-coumarin (2 mL of a DMF stock solution, concentration of 4.9 mg/mL, 23 mmol/mL) were added. Finally, a dispersion containing SPS-p(HEA)-

N_3 in DMF (1 mL, 1 wt%) was injected. The reaction continued for 24 hours under gentle stirring at 70 °C, after which the colloids were washed with DMF.

4.2.6 Magnetic Field. An external horizontal magnetic field was induced by two permanent magnets (Geomag) placed equidistantly from the sample contained in a capillary. The distance between the magnets was chosen such that the strength of the magnetic field in the sample was about 3 mT as determined with a gaussmeter. However, this magnetic field was rather inhomogeneous leading to a strong gradient of particle concentration. To induce a homogeneous magnetic field of 3 mT, a Helmholtz cube was developed (see Section 4.3.3). A magnetic field of 3 mT results in an interaction strength on the order of 65 k_BT which is sufficiently large to induce chain formation of superparamagnetic silica spheres.

4.2.7 Irradiation Experiments. A 14 W low-pressure mercury lamp emitting UV-light with a wavelength of 365 nm was used to cross-link the photo-responsive colloids. Typically, samples were irradiated for 24 hours.

4.2.8 Characterization. IR spectra were obtained using a Perkin Elmer FT-IR/FIR Frontier Spectrometer in attenuated total reflectance (ATR) mode. The measurements were carried out on powders (obtained by drying the corresponding particle dispersion).

Transmission electron microscopy (TEM) pictures were taken with a Philips Tecnai10 electron microscope typically operating at 100 kV. Bright field images were recorded using a SIS Megaview II CCD camera. The samples were prepared by drying a drop of diluted aqueous particle dispersion on top of polymer coated copper grids.

Optical microscopy images were obtained using a Nikon Eclipse Ti-E inverted microscope equipped with a Hamamatsu Orca Flash 4.0 V2 Digital Camera. A Nikon CFI Apo TIRF objective (100× magnification, N.A. 1.49) was used. Pictures were recorded in bright field mode. Samples were prepared by filling hollow glass tubes (0.1×2×50 mm, VitroCom) with particle dispersions by capillary action. The tubes were sealed with optical adhesive (Norland 81) that was cured with UV-light (wavelength of 365 nm, 6 W UVP UVGL-58 lamp).

4.3 Results and Discussion

4.3.1 Synthesis of Magnetic and Photo-Responsive Silica Spheres. An overview of the synthetic strategy towards magnetic and photo-responsive silica spheres is given in Figure 4.1. Compared to the synthesis route for photo-responsive polystyrene colloids as described in Chapter 3, one additional step is required: the amine functionalization of the bare silica colloids. Two batches of commercial superparamagnetic silica spheres were used with diameters of 566 ± 18 nm and 548 ± 14 nm as determined with TEM. A representative TEM image can be found in figure 4.2a. In the absence of an external magnetic field, well-dispersed spheres can be observed in water, see Figure 4.2b.

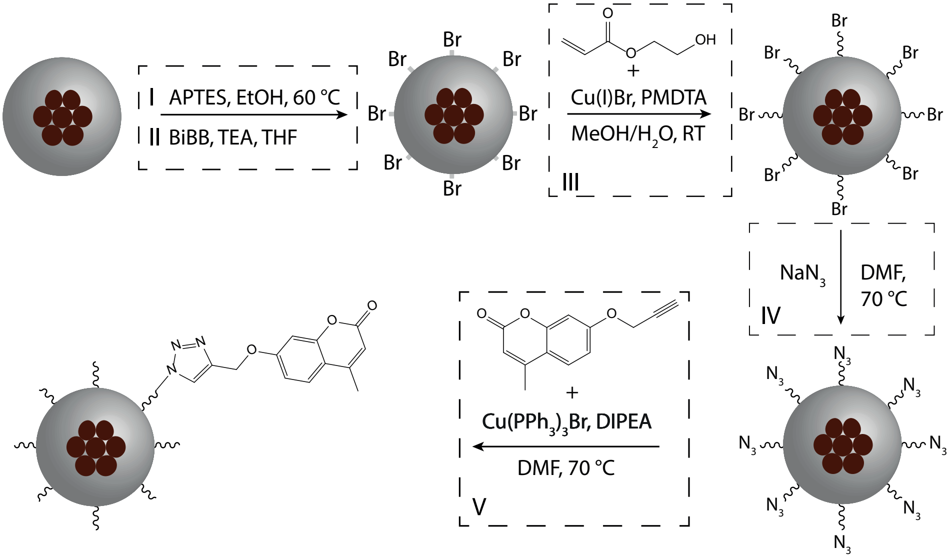

Figure 4.1: Schematic overview of the synthesis route towards magnetic and photo-responsive silica spheres. The small, brown spheres indicate the iron oxide nanoparticles randomly distributed throughout the silica matrix of the particles. (I) Seeded growth of core-shell amino-functionalized magnetic silica spheres. (II) Initiator-functionalized magnetic particles are obtained in the presence of BiBB, THF and TEA. (III) Polymeric HEA hairs are grafted from the surface of brominated colloidal initiators using SI-ATRP. (IV) The halogen chain ends of p(HEA) are substituted by azides via a nucleophilic substitution reaction. (V) Alkyne-coumarin is coupled to the azide chain ends via the Huisgen click reaction.

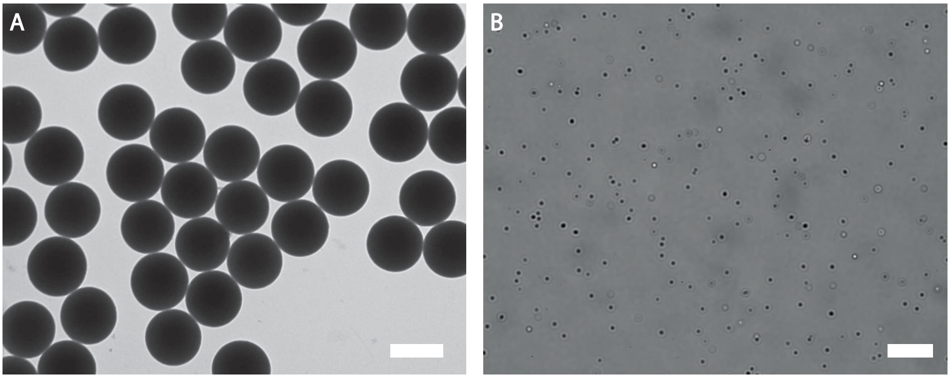

Figure 4.2: Superparamagnetic silica spheres. Representative (a) TEM and (b) optical microscopy images in the absence of an external magnetic field. Scale bars are 0.5 μm and 20 μm respectively.

IR spectra were recorded to confirm the successful coupling of alkyne-coumarin to the silica colloids, see Figure 4.3. Successful coupling of azides to the surface of the magnetic particles was confirmed by the free azide vibration at 2096 cm^{-1}. The subsequent disappearance of this signal confirmed the effectiveness of the coumarin coupling to the chain ends of the grafted polymers.

4.3.2 Inhomogeneous Magnetic Field. Figure 4.4a shows the chains of spheres that arise as an external magnetic field is applied to a dispersion of photo-responsive and superparamagnetic particles. In this particular case, two permanent magnets were used to induce a horizontal magnetic field. As this field is inhomogeneous, over time, the chains of spheres accumulate on one side of the sample and large aggregates are formed, see Figure 4.4b. Upon irradiation of this sample with UV-light for 24 hours and subsequent removal of the magnetic field, large clusters of spheres are obtained, see Figure 4.4c.

4.3.3 Helmholtz Cube. A Helmholtz cube was developed for *in situ* observation of colloids in a homogeneous magnetic field, see Figure 4.5. Three pairs of Helmholtz coils were arranged orthogonally producing a three-dimensional magnetic field. Two circular coils form the inner Helmholtz pair that provides the magnetic field in the z-direction (vertically). This circular geometry was chosen to minimize the diameter (and consequently maximize the field strength), and to ensure that the cylindrical microscope objective can fit inside the Helmholtz cube. The cylindrical coils are

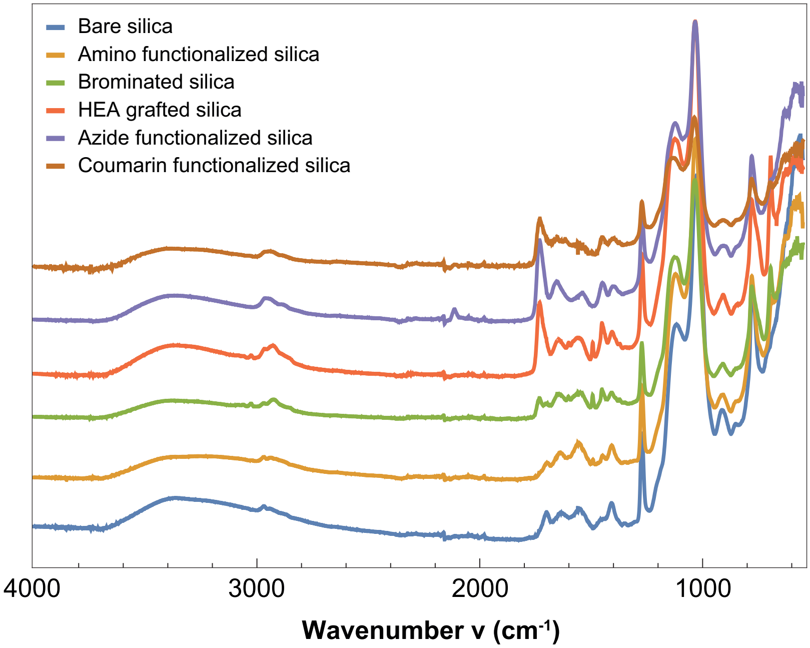

Figure 4.3: IR spectra of the surface-functionalized particles. From bottom to top: superparamagnetic silica spheres prior to functionalization (blue), amino-functionalized silica spheres (yellow), brominated core-shell silica particles (green), HEA grafted silica spheres (orange), silica spheres with azide terminated HEA hairs (purple) and the coumarin-functionalized photo-responsive and magnetic colloids (brown). The characteristic free azide vibration at 2096 cm^{-1} is indicated. Spectra have been offset vertically for the sake of clarity.

positioned concentrically on the optical axis of the microscope, at a distance $d = R$, with R the radius of the coils. The magnetic field B at this distance, is given by:[18]

$$B = \frac{8\mu_0 N}{5\sqrt{5}R} I, \tag{4.1}$$

where μ_0 is the permeability of free space ($4\pi \cdot 10^{-7}$ Tm/A), N is the number of turns of copper wire and I is the current running over the coils. The gradient of the field $\partial B/\partial z$ and the second derivative of the magnetic field $\partial^2 B/\partial z^2$ both equal zero exactly in between the coils.

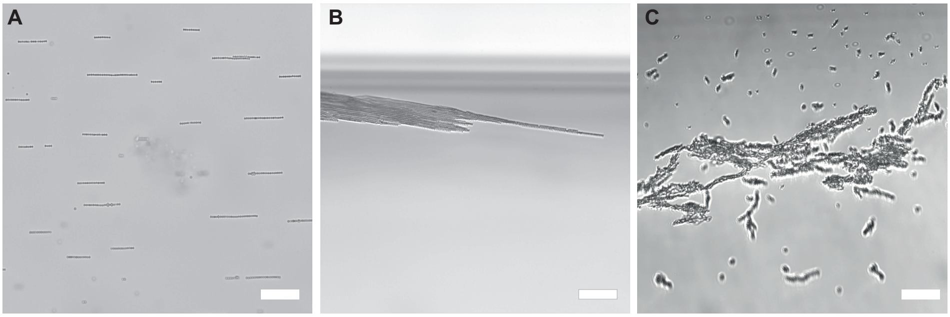

Figure 4.4: Superparamagnetic and photo-responsive silica spheres in an inhomogeneous magnetic field. (a) Particles align in a horizontal magnetic field induced by two permanent magnets. (b) Due to inhomogeneity of the generated magnetic field, chains of particles tend to accumulate at one side of the sample. (c) Upon irradiation with UV-light and removal of the field, large clusters are obtained. Scale bars are 15 μm.

Two sets of square coils form the middle and outer Helmholtz pairs. The distance d between each set of coils is equal to 0.5445 times the length of the square sides.[19,20] As with the circular coils, both the gradient and the second derivative of the magnetic field are equal to zero exactly in between the coils. For the square coils, the magnetic field $\vec{B}$ can be calculated using the Biot-Savart law:[18,21]

$$\vec{B}(r) = \frac{\mu_0}{4\pi} I \oint \frac{d\vec{l} \times \vec{r}}{r^3}. \tag{4.2}$$

The integration is over the length $\vec{l}$ of the sides of the squares carrying the steady current I and $\vec{r}$ is the distance from the coils. The homogeneity or uniformity of the field induced by the square Helmholtz coils can be expressed by a contour plot, see Figure 4.5b. The fluctuations of the magnetic field are on the order of 0.5%.

An xy translation stage was designed to place a microscope sample in the field of view of the microscope and in the centre of the Helmholtz cube. The Helmholtz frame and the sample holder were printed by a 3D printer. Copper wires were wound on the coils by the company Wikkelbedrijf Rijswijk B.V. in Driebruggen, the Netherlands. The diameter of the round wires is 0.71 mm, allowing a DC current of maximum 1.55 A in the absence of external cooling. The nominal current generates a quasi-static magnetic field in air of at least 3 mT in the x- and y-directions and 6 mT in the z-direction. The properties of the Helmholtz coils are summarized in Table 4.1.

Table 4.1: Properties of the three pairs of Helmholtz coils.

Coil pair	Field direction	Geometry	Turns	Field (mT)
Inside	Z	Circular	170	6.2
Middle	Y	Square	140	3.2
Outside	X	Square	170	3.2

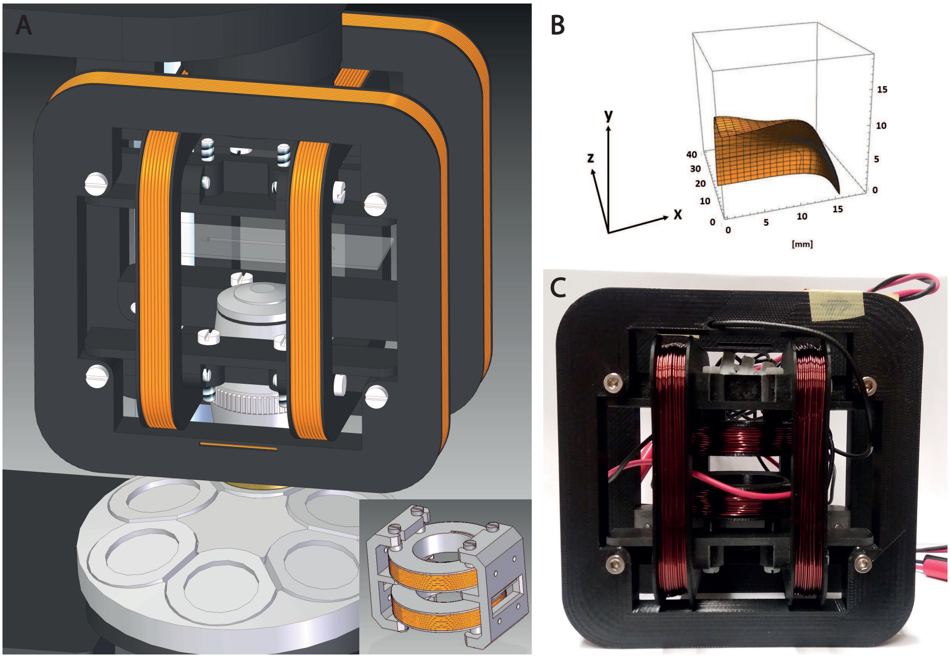

Figure 4.5: Helmholtz cube. (a) Schematic representation of two pairs of square Helmholtz coils encompassing a microscope sample and objective, coaxial to the optical axis of an inverted microscope. The midpoint of the three orthogonal coils is positioned at the focal point of the microscope. Inset shows a schematic of the inner Helmholtz pair formed by two circular coils. (b) Contour plot of homogeneity of the magnetic field $\vec{B}$ in the centre of the cube (0,0,0). The two square coils can be found on the positions $x = -24\,\text{mm}$ and $x = +24\,\text{mm}$, respectively. (c) Photo of the realised Helmholtz cube.

4.3.4 Homogeneous Magnetic Field. Figure 4.6a shows superparamagnetic and photo-responsive silica spheres aligned in the homogeneous magnetic field inside the Helmholtz cube. Upon irradiation with UV-light and removal of the field, permanent magnetisable chains of silica spheres are obtained, see Figure 4.6b. For this particular particle concentration, a chain is composed of 14 spheres on average. On applying a vertical field, shorter and more monodisperse chains in length are formed. Longer chains can be obtained by increasing the concentration of spheres, see Figure 4.6c. Typically, the magnetic field is applied for approximately two hours before the growth of the chains appears stagnated and saturation of mean chain length is observed.[22] By employing spheres with another diameter, the thickness of these rodlike particles can easily be tuned, see Figure 4.6d.

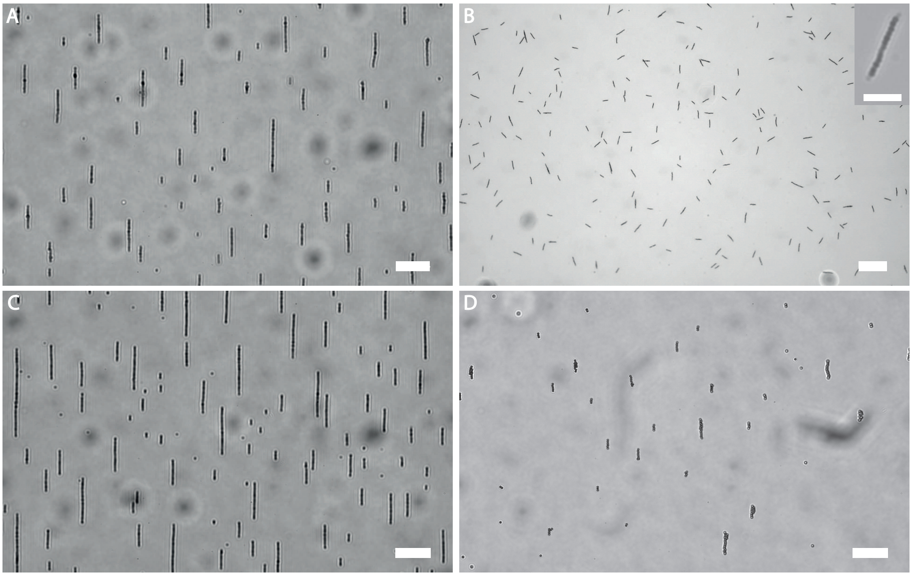

Figure 4.6: Superparamagnetic and photo-responsive silica spheres in a homogeneous magnetic field. (a) Linear chains of spheres are obtained in a magnetic field induced by Helmholtz coils. Particle concentration of 0.005 wt% was used; scale bar is 20 μm. (b) Upon irradiation with UV-light and removal of the field, permanent magnetisable chains of spheres are obtained. Scale bar is 50 μm. Inset shows one magnetic chain that is composed of 14 silica spheres (scale bar is 5 μm). (c) An increase in the mean chain length is observed when utilizing a higher particle concentration (0.007 wt%). Scale bar is 20 μm. (d) Spheres with a larger diameter (0.96 μm) form rodlike chains with an increased diameter. Scale bar is 20 μm.

4.4 Conclusions and Outlook

Permanent chains of photo-responsive and superparamagnetic silica colloids were synthesized. By utilizing a modified version of our synthesis route towards photo-crosslinkable polystyrene colloids, silica spheres were functionalized with coumarin molecules. Upon irradiation with UV-light, the colloids crosslinked, and magnetisable sphere chains were realized in bulk. The aspect ratio of these rods can easily be varied by changing the particle concentration and thus controlling the length of the chains. The development of a Helmholtz cube was required to induce a homogeneous magnetic field that produced linear sphere chains instead of particle aggregates. The rodlike chains are susceptible to external magnetic fields and might be employed in future studies to produce liquid crystalline structures.

Acknowledgements

Sandrine Heijnen and Patrick van Vliet are thanked for performing some of the experiments described here. Bonny Kuipers is acknowledged for designing the Helmholtz setup. We thank Marcel van Asselen of the Engineering group of the Scientific Instrumentation department for the mechanical design and Manfred van den Berg, Helge Veltman and co-workers of the Production group for the realization of the Helmholtz setup.

References

1. D. Jiles. *Introduction to Magnetism and Magnetic Materials*, Chapman & Hall, **1991**.
2. M. V. Berry & A. K. Geim. Of flying frogs and levitrons, *Eur. J. Phys.* **1997**, *18*, 307–313.
3. A. K. Geim. Everyone's magnetism, *Phys. Today* **1998**, *51*, 36–39.
4. A. Darras, E. Opsomer, N. Vandewalle & G. Lumay. Superparamagnetic colloids in viscous fluids, *Sci. Rep.* **2017**, *7*, 7778.
5. E. M. Claesson & A. P. Philipse. Monodisperse magnetizable composite silica spheres with tunable dipolar interactions, *Langmuir* **2005**, *21*, 9412–9419.
6. U. Jeong, X. Teng, Y. Wang, H. Yang & Y. Xia. Superparamagnetic colloids: Controlled synthesis and niche applications, *Adv. Mater.* **2007**, *19*, 33–60.

7. C. T. Yavuz, J. T. Mayo, W. W. Yu, A. Prakash, J. C. Falkner, S. Yean, L. Cong, H. J. Shipley, A. Kan, M. Tomson, D. Natelson & V. L. Colvin. Low-field magnetic separation of monodisperse Fe_3O_4 nanocrystals, *Science* **2006**, *314*, 964–967.
8. L. R. Moore, A. R. Rodriguez, P. S. Williams, K. McCloskey, B. J. Bolwell, M. Nakamura, J. J. Chalmers & M. Zborowski. Progenitor cell isolation with a high-capacity quadrupole magnetic flow sorter, *J. Magn. Magn. Mater.* **2001**, *225*, 277–284.
9. J. Ge, Y. Hu & Y. Yin. Highly tunable superparamagnetic colloidal photonic crystals, *Angew. Chem. Int. Ed.* **2007**, *119*, 7572–7575.
10. J. Ge & Y. Yin. Magnetically tunable colloidal photonic structures in alkanol solutions, *Adv. Mater.* **2008**, *20*, 3485–3491.
11. C. Lok. Picture perfect, *Nature* **2001**, *412*, 372–374.
12. T. Neuberger, B. Schöpf, H. Hofmann, M. Hofmann & B. von Rechenberg. Superparamagnetic nanoparticles for biomedical applications: Possibilities and limitations of a new drug delivery system, *J. Magn. Magn. Mater.* **2005**, *293*, 483–496.
13. Q. A. Pankhurst, J. Connolly, S. K. Jones & J. Dobson. Applications of magnetic nanoparticles in biomedicine, *J. Phys. D: Appl. Phys.* **2003**, *36*, R167.
14. L. W. McKeehan. Gaugain-Helmholtz (?) coils for uniform magnetic fields, *Nature* **1934**, 833–834.
15. M. S. Crosser, S. Scott, A. Clark & P. M. Wilt. On the magnetic field near the center of Helmholtz coils, *Rev. Sci. Instrum.* **2010**, *81*, 084701.
16. T. Wu, Y. Zhang, X. Wang & S. Liu. Fabrication of hybrid silica nanoparticles densely grafted with thermoresponsive poly(n-isopropylacrylamide) brushes of controlled thickness via surface-initiated atom transfer radical polymerization, *Chem. Mater.* **2008**, *20*, 101–109.
17. L. Jiang, H. Bagan, T. Kamra, T. Zhou & L. Ye. Nanohybrid polymer brushes on silica for bioseparation, *J. Mater. Chem. B* **2016**, *4*, 3247–3256.
18. D. J. Griffiths. *Introduction to Electrodynamics*, Prentice Hall, **1999**.
19. J. J. Abbott. Parametric design of tri-axial nested Helmholtz coils, *Rev. Sci. Instrum.* **2015**, *86*, 054701.
20. M. E. Rudd & J. R. Craig. Optimum spacing of square and circular coil pairs, *Rev. Sci. Instrum.* **1968**, *39*, 1372–1374.

21. J. D. Jackson. *Classical Electrodynamics*, Wiley, **1999**.

22. A. Darras, J. Fiscina, M. Pakpour, N. Vandewalle & G. Lumay. Ribbons of superparamagnetic colloids in magnetic field, *Eur. Phys. J. E* **2016**, *39*, 47.

PART III

Chiral Colloids

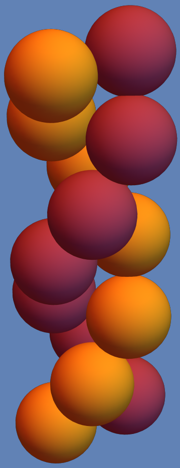

5

Helical, Zigzag and Zipper Chains from Photo-Responsive Colloids

Abstract

We disclose a method for the synthesis of helical chains from spontaneously formed hollow sugar-surfactant microtubes with internally confined mobile colloidal spheres. These spheres are surface-functionalized with photo-responsive coumarin moieties, which allow for UV-induced, covalent clicking of colloids into permanent chains, with morphologies set by the colloid-to-tube diameter ratio. Subsequent dissolution of tube confinement yields aqueous suspensions that comprise bulk quantities of a variety of linear chains, including single helical chains of polystyrene colloids. These colloidal equivalents of chiral (DNA) molecules are intended for microscopic study of chiral dynamics on a single-particle level.

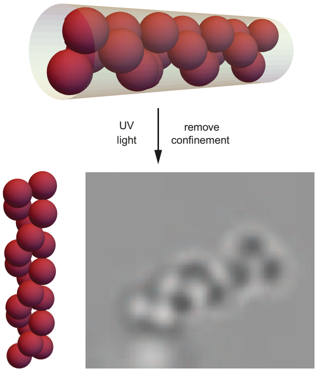

5.1 Introduction

Among the captivating consequences of symmetry-breaking chirality is the coupling of rotational and translational degrees of freedom manifested in the Baranova and Zel'dovich propeller effect.[1–4] Since it is not viable to visualize this intriguing coupling, and other phenomena such as chiral liquid crystal formation, on a single-particle level for chiral molecules, we set out to synthesize chiral colloids. Colloids are similar to molecules in that they are sufficiently small to exhibit Brownian motion, but unlike their molecular counterparts they are *in situ* observable by optical microscopy.[5,6]

A drawback of reported synthesis methods of chiral colloids is the need for complex, anisotropic building blocks with directional interactions. For example, colloidal helical structures that mimic the DNA helix have been assembled from anisotropic magnetic colloids[7] and amphiphilic Janus spheres.[8] Furthermore, template-based (*e.g.* DNA) and lithographic techniques are often employed.[2,9–11] These methods have several downsides such as a low yield,[2,9] fragile helical products prone to dissociation,[8] clusters subsisting only in an external magnetic field,[7] or the need for expensive chemicals and multiple purification steps.[10]

Inspired by a computational study of Pickett et al.,[12–14] predicting that spheres can assemble into helical chains upon cylindrical confinement, spherical particles have been used as building blocks for complex structures.[15,16] Yin and Xia,[17] for example, experimentally explored the preparation of helical chains from simple colloidal spheres confined in V-grooves by capillary forces. However, the obtained structures are immobile and produced in low yield with only a limited number of particles available through slow and batch processes.

In this Chapter, we report a new synthetic strategy for chiral colloids that is not limited to certain materials or particle properties and that does not require DNA, anisotropic particle shapes or directional interactions. Robust colloids have been prepared with an unprecedented yield not attainable with conventional (lithography) techniques. Our method exploits the co-assembly of microtubes and colloidal particles, developed in our group, to synthesize helical, zigzag and zipper colloidal chains in bulk.[18–20] To this end, we designed photo-responsive colloids that form covalent bonds upon irradiation with UV-light inside the cylindrically confining environment created by the microtubes. Upon removal of the template, a variety in assemblies is obtained in aqueous suspension. The resulting colloidal chains depend sensitively on the colloid-to-tube diameter ratio.

5.2 Experimental Methods

5.2.1 Materials. Sodium dodecyl sulphate (SDS, >97%) and β-cyclodextrin (β-CD, $\geq$ 97%) were obtained from Sigma Aldrich. SDS was used as received while β-CD was dried under a heat lamp prior to use to remove excess water. The water used in all experiments was purified using a Milli-Q water purification system.

5.2.2 Co-assembly of Colloids and Microtubes. SDS and β-CD were weighed and mixed as to obtain a molar ratio of β-CD:SDS of 2:1 and a total concentration of SDS and β-CD of 10 wt% in water (typically 1.72 g or 1.5 mmol β-CD and 0.22 g or 0.8 mmol SDS in 17.5 g H_2O). While being magnetically stirred, the mixture was heated to 60 °C in an oil bath until a transparent and isotropic solution was obtained. The microtubes were formed upon cooling to room temperature; a turbid and viscous suspension was obtained. Photo-responsive colloidal polystyrene spheres (see Chapter 3) were incorporated inside the microtubes by centrifuging aqueous colloidal dispersions and replacing the supernatant by microtube suspension. Typically, the mixture of colloids and microtubes contained 10 wt% colloidal particles. The mixture was heated to approximately 60 °C to melt the microtubes, sonicated and then vortexed to disperse the particles inside the microtubes. Upon cooling to room temperature, the sample was gently rotated to avoid sedimentation of the colloids.

5.2.3 Irradiation Experiments. A 14 W low-pressure mercury lamp emitting UV-light with a wavelength of 365 nm was used to crosslink the photo-responsive colloids. Samples consisting of colloids incorporated inside microtubes in cuvettes were placed in a water bath to prevent the temperature increasing above 40 °C; the melting temperature of the microtubes. Typically, samples were irradiated for 24 hours. Water was then added to dissolve the microtubes. Control samples were enclosed in aluminium foil to prevent the penetration of UV-light.

5.2.4 Characterization. Scanning emission electron microscopy (SEM) pictures were taken with a FEI XL30 FEG scanning electron microscope operating at 5-15 kV. SEM samples were prepared by drying a drop of diluted aqueous particle dispersion on top of polymer coated copper grids and sticking these grids on a stub using a conductive carbon sticker, which was coated with a platinum layer of typically 6 nm.

Optical microscopy images were obtained using a Nikon Eclipse Ti-E inverted microscope equipped with a Hamamatsu Orca Flash 4.0 V2 Digital Camera. A Nikon CFI Apo TIRF objective (100× magnification, N.A. 1.49) was used. Pictures were recorded in bright field mode. Samples were prepared by placing 5-10 μL dispersion between a microscope slide (76×26 mm, Menzel-Gläser) and a cover slip (22×22×0.17 mm, Menzel-Gläser) with two cover glasses as spacers (22×22×0.10 mm, VWR). Cells were sealed with glue (Norland optical adhesive 81) that was cured with UV-light (365 nm, 6 W UVP UVGL-58 lamp). Alternatively, hollow glass tubes (0.1×2×50 mm, VitroCom) were filled with particle dispersions by capillary action and also sealed with UV curing optical adhesive.

5.3 Results

5.3.1 Co-Assembly of Colloids and Microtubes. Cyclodextrins (CDs) are donut-like sugar molecules with a hydrophilic exterior and a hydrophobic interior.[21] In water, the cavities of CDs can minimize undesirable interactions by incorporating the hydrophobic tails of surfactants. Mixtures of β-CD and SDS thus form host-guest inclusion complexes in a 2:1 molar ratio at temperatures above 40 °C in aqueous media. Upon cooling to room temperature these SDS@2β-CD complexes self-assemble into multiple equally spaced curved bilayers forming a set of concentric hollow cylinders.[22] These cylinders are straight and rigid tubes that can be several tens of micrometres long with a pore diameter of 0.9 μm ± 10%. On addition of colloidal spheres, the tubular structures act as a cylindrically confining environment and ordered, chain-like colloid-in-tube assemblies are obtained. As the microtubes form a space-filling structure, all colloidal particles with a size smaller than the microtube diameter appear confined in the tubes. Depending on the size ratio of the colloid-to-tube diameters, various structures, including helical sphere chains, are formed. Upon removal of the confinement, the formed colloid-in-tube assemblies dissociate. To secure the morphology of colloid structures prior to dissociation, we designed photo-responsive polystyrene spheres for UV-induced crosslinking, see Figure 5.1.

5.3.2 Assembly into Sphere Chains. Polystyrene spheres with surface-immobilized coumarin derivatives were assembled inside the microtubes with a particle loading of 10 wt%. Upon irradiation of the photo-responsive colloids inside the microtubes with UV-light with a wavelength of 365 nm, coumarin molecules on adjacent particles photo-dimerized and the colloid-in-tube assemblies were affixed. The cylindrical confinement was subsequently removed by dilution of the system with water, causing the microtubes to disassemble (see Figure 5.2). The obtained structures exhibit

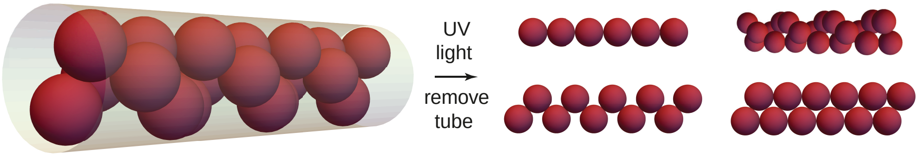

Figure 5.1: Schematic representation of the assembly of spheres into chains. Photo-responsive colloidal spheres are confined in (thermo-reversible) microtubes with a colloid-to-tube diameter ratio of about 0.5. Due to geometric restrictions, the colloids assemble in a variety of structures including helical sphere chains. Upon irradiation with UV-light the colloids are covalently bound together inside the microtubes. By diluting the system with water, the microtubes dissolve and stable colloidal structures, including chiral chains, in bulk are obtained.

Brownian motion and are mechanically robust as the assemblies can withstand hours of exposure to ultra-sonication without disintegrating.

5.3.3 Analysis of Formed Structures. The size ratio of the colloid-to-tube diameters ultimately determines the structures that can be formed. To investigate the effect of the size ratio on the assemblies, we employed colloids of different sizes. Figure 5.3 shows the distribution of structures that are obtained as a function of the colloid-to-tube diameter size ratio. As the particle diameter approaches that of the microtubes (colloid-to-tube diameter ratio of about one), a clear preference for assembly in linear, rodlike chains is observed. Particles that are much smaller than the microtube diameter, do not feel the confinement and are thus randomly distributed throughout the cylindrical tubes forming small and random aggregates. Conversely, particles that are much larger than one micrometre cannot be incorporated inside the tubes. The structures in bulk resulting from particles that have a colloid-to-tube diameter ratio of about 0.5 vary from linear chains, zigzag and zipper chains to helical assemblies, see Figure 5.4. Typically, a racemic mixture is formed and the chain lengths vary from two (dimers) to 30 spheres per chain. The average length of the chains can be varied by changing the weight percentage of particles inside the microtubes. An increase in the particle concentration leads to an increase in the number of spheres per chain, but the length is ultimately limited by the extent of the tubes, typically in the range of tens of microns.

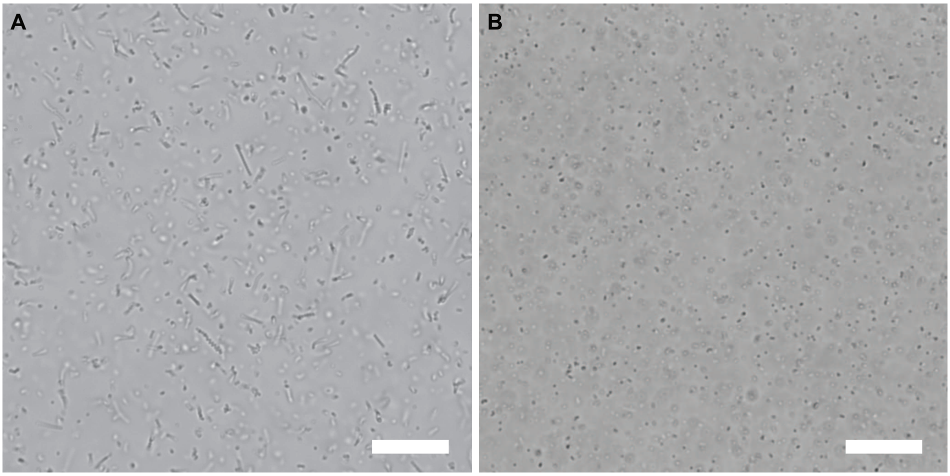

Figure 5.2: Optical microscopy images of colloidal dispersions upon UV irradiation and dissolution of microtubes. (a) A large number of colloidal chains in aqueous suspension. Field of view is 123 μm×123 μm. See Supporting Video at DOI:10.1021/acsnano.8b05065. (b) Control sample that was enclosed in aluminium foil to prevent the penetration of UV-light; no assemblies are formed. Scale bars are 10 μm.

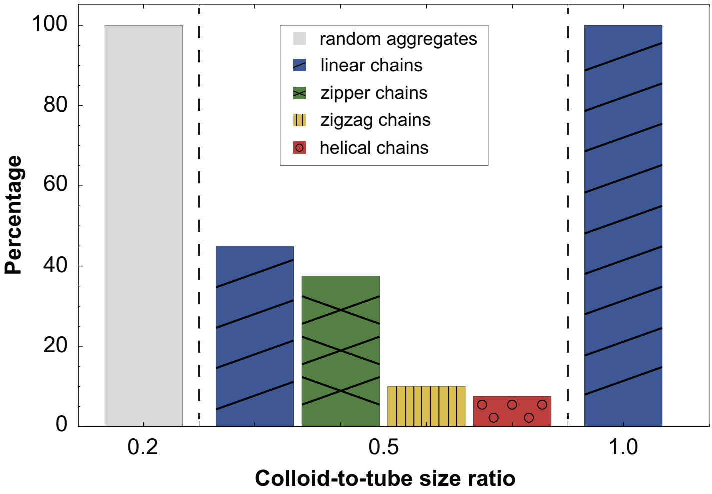

Figure 5.3: Probability to find a cluster of a certain shape. Distribution of linear, zigzag, zipper, and helical chains as a function of the colloid-to-tube diameter size ratio. The percentages were determined by counting at least 100 assemblies per size ratio as found in representative microscopy images.

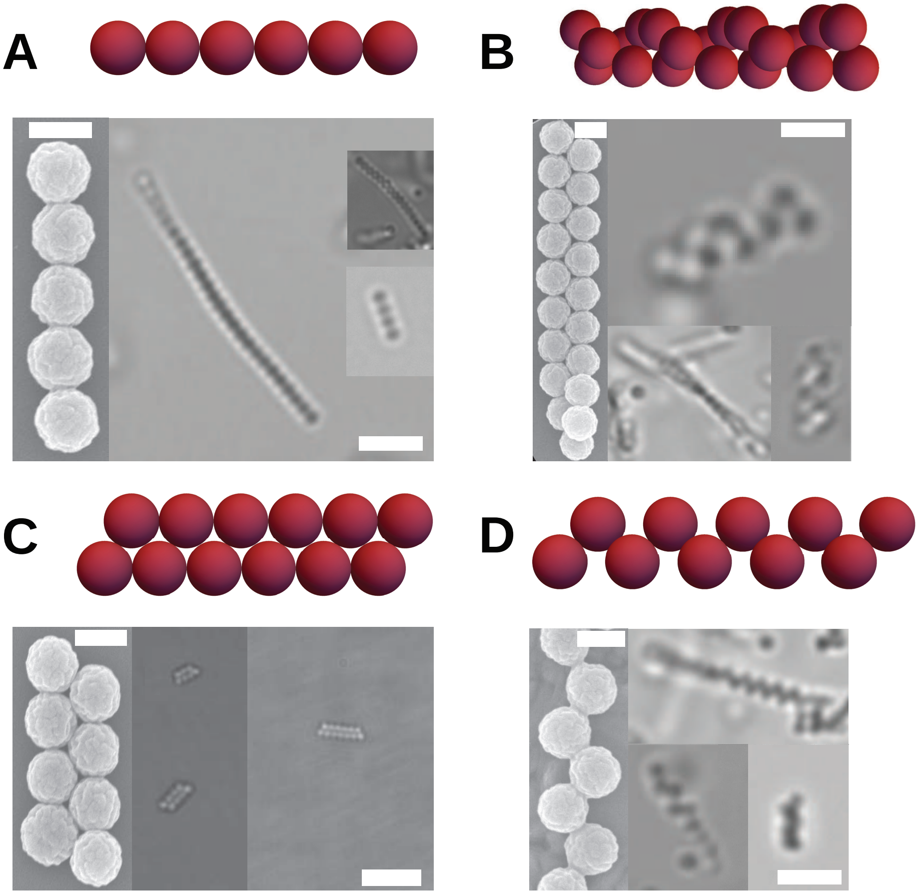

Figure 5.4: Optical microscopy images. (a) Linear sphere chain, (b) helical chain, (c) zipper chain, and (d) zigzag sphere chain. Scale bars are 10 μm. Insets show models and scanning electron microscopy images (scale bars are 0.5 μm) of the obtained structures. See Supporting Videos at DOI:10.1021/acsnano.8b05065.

5.3.4 Estimation of Yield. As we employ a wet synthesis method to produce sphere chains, our yield is unattainable for two-dimensional techniques such as lithography. A quantification of the yield is obtained as follows. Each step of the synthesis is performed with 1 wt% of particle dispersion. Considering that the density of polystyrene is almost equal to that of water, we can approximate the volume fraction of particles to be 1%. The final step of the synthesis is typically performed with 0.25 mL dispersion. This then contains 2.5 μL particles which corresponds to 2.5 mm^3 or 2.5×10^9 $\mu\mathrm{m}^3$. Assuming that a chain on average consists of 10 spheres, the volume of an assembly is equal to $10\pi/6d^3$. With the diameter d of the particles being about 0.5 μm, the volume of a cluster is approximately 0.7 $\mu\mathrm{m}^3$. Considering that typically 20% of particles are present as single spheres, we find an estimated yield of 10^9 chains after one synthesis round. As our bulk method can be performed on larger scales, the yield can easily be further increased.

5.4 Discussion

By utilizing microtubes and photo-responsive polystyrene spheres, freely dispersed complex structures in bulk are obtained. As microtubes tend to be sensitive to changes in concentration, pH and ionic strength, among others, we developed photo-responsive colloids since light is an external and non-disruptive trigger towards the confinement. The advantage of employing coumarin as the photo-responsive glue is that no photo-initiator was required. However, coumarin is hydrophobic and grafting densities had to be kept to a minimum to safeguard colloidal stability and to prevent intra-particle coumarin crosslinking. On the other hand, the surface number density of coumarin molecules had to be sufficiently high to induce colloid attachment.

A wide range of structures is produced for a colloid-to-tube diameter ratio of about 0.5. According to theory, the yield of each species and the pitch of the chiral chains could be controlled by fine-tuning the ratio of the colloid-to-tube diameters.[12–14] As a consequence of the inherent polydispersity in particle size and microtube diameter, however, it is difficult to fall within these narrow ranges experimentally. Therefore, post-synthesis separation techniques were explored. Established chiral separation methods for molecules, such as chromatography and capillary electrophoresis, are not suitable for colloidal particles as they utilize chirality specific chemical interactions.[23] We employed density gradient centrifugation (DGC) to successfully separate small clusters and single particles from the desired chains. Unfortunately, DGC cannot distinguish between a linear or helical chain composed of 10 spheres. Our chiral colloids might be isolated in a helical flow field; Aristov et al. demonstrated the separation of left- and right-handed micron-sized chiral particles in a helical fluid flow inside a microfluidic device.[24]

Since the colloidal assemblies show variations in size, geometry and type of enantiomers, they are ideal for single-particle studies of the dynamics and Brownian motion of colloids with chiral and other geometries, which is currently ongoing work. Furthermore, preliminary results have shown that the synthesis procedure as outlined in this Chapter is not limited by the chemical nature of the colloids. Photo-responsive silica spheres have been prepared in a similar fashion yielding colloidal silica assemblies. By using metallic functionalization, chiral plasmonic properties can be achieved for the fabrication of optically active media.[25] In addition, our wet synthesis method can easily be performed on larger scales further increasing the yield. Finally, the chiral structure of the microtubes, as a result of the constituent chiral cyclodextrin molecules, could be exploited to synthesize homo-chiral chains. However, the chiral coupling is currently too weak to influence the confined colloids. If the chirality on the nanoscale could be enhanced, this might lead to homo-chiral chains, but this is a topic for future research.

5.5 Conclusions and Outlook

In conclusion, we have developed a synthesis method to produce robust colloidal assemblies, including chiral colloids, in high yield. Employing the co-assembly of colloidal particles and microtubes, colloidal helices can be assembled from spherical building blocks. Our synthesis route yields photo-crosslinkable colloidal polystyrene spheres that are sterically stabilized with polymer hairs and end-functionalized with coumarin molecules. By exposure to UV-light, the coumarin molecules act as a chemical glue holding the spheres in place even after dissolution of confining tubes. Eventually, a library of ordered structures, such as linear chiral assemblies, zigzag and zipper configurations of isotropic colloidal spheres, has become available in bulk. These colloidal analogues of chiral molecules are a promising model system to study the role of chirality in the self-assembly and the diffusion of biological macromolecules, such as the DNA helix. Further insight into the functionality of chirality on the molecular scale could aid in the design of novel chiral materials.

Acknowledgements

Rumen Georgiev is thanked for the drawing of a (confined) double helical sphere chain. Kanvaly Lacina is acknowledged for performing SEM and for help with optimizing the synthesis procedure. Carla Fernández Rico, Florian van der Stap and Rebecca Costello are thanked for performing some of the experiments described here.

Appendix 5.A Colloids at Microtubes

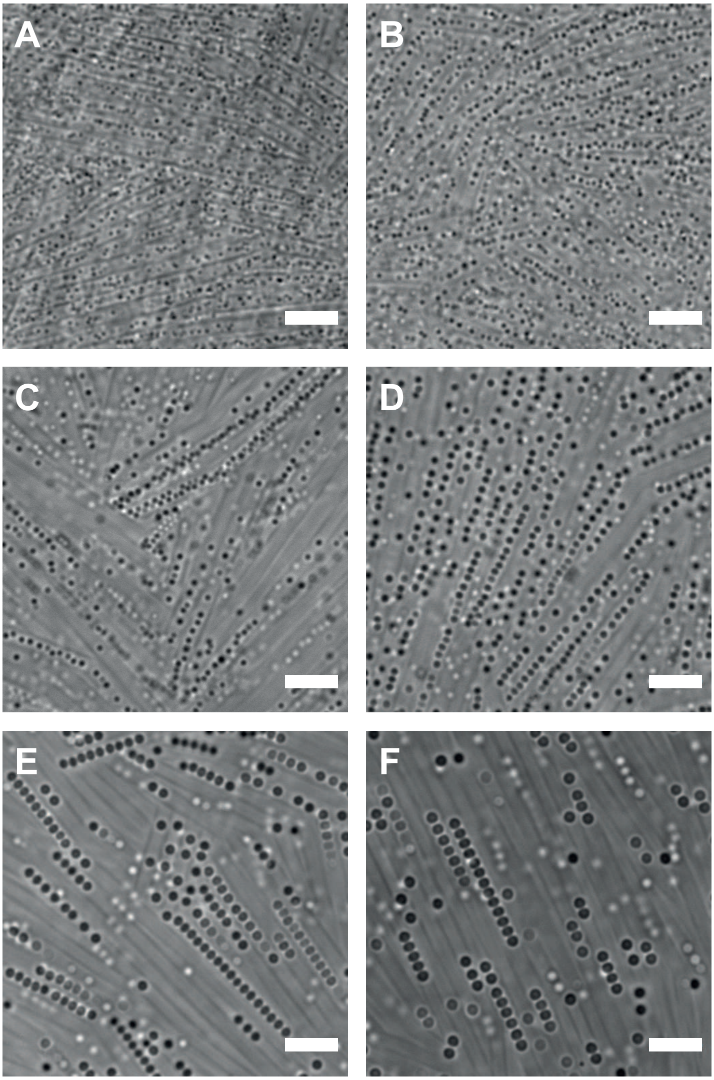

Appendix Figure 5.1: Silica spheres in microtubes. 10 wt% silica spheres of various sizes (polydispersity <3%) were incorporated in SDS@2β-CD microtubes with a uniform pore diameter of ≈1 μm. Silica spheres with a diameter of (a) 267 nm and (b) 407 nm form random distributions inside the microtubes. (c) Silica spheres with a diameter of 495 nm arrange into zigzag, zipper, helical and linear sphere chains. (d-f) Silica spheres with a diameter above 0.6 μm (619 nm, 832 nm and 935 nm respectively) arrange into linear chains. Scale bars are 5 μm.

References

1. N. B. Baranova & B. Y. Zel'dovich. Separation of mirror isomeric molecules by radio-frequency electric field of rotating polarization, *Chem. Phys. Lett* **1978**, *57*, 435–437.
2. D. Schamel, M. Pfeifer, J. G. Gibbs, B. Miksch, A. G. Mark & P. Fischer. Chiral colloidal molecules and observation of the propeller effect, *J. Am. Chem. Soc.* **2013**, *135*, 12353–12359.
3. D. J. Kraft, R. Wittkowski, B. ten Hagen, K. V. Edmond, D. J. Pine & H. Löwen. Brownian motion and the hydrodynamic friction tensor for colloidal particles of complex shape, *Phys. Rev. E* **2013**, *88*, 050301.
4. Y. Han, A. M. Alsayed, M. Nobili, J. Zhang, T. C. Lubensky & A. G. Yodh. Brownian motion of an ellipsoid, *Science* **2006**, *314*, 626–630.
5. V. Manoharan. Colloidal matter: Packing, geometry, and entropy, *Science* **2015**, *349*, 125375.
6. W. Poon. Colloids as big atoms, *Science* **2004**, *304*, 830–831.
7. D. Zerrouki, J. Baudry, D. J. Pine, P. Chaikin & J. Bibette. Chiral colloidal clusters, *Nature* **2008**, *455*, 380–382.
8. Q. Chen, J. K. Whitmer, S. Jiang, S. C. Bae, E. Luijten & S. Granick. Supracolloidal reaction kinetics of Janus spheres, *Science* **2011**, *331*, 199–202.
9. W. Feng, J. Y. Kim, X. Wang, H. A. Calcaterra, Z. Qu, L. Meshi & N. A. Kotov. Assembly of mesoscale helices with near-unity enantiomeric excess and light-matter interactions for chiral semiconductors, *Sci. Adv.* **2017**, *3*, 1601159.
10. M. Siavashpouri, C. H. Wachauf, M. J. Zakhary, F. Praetorius, H. Dietz & Z. Dogic. Molecular engineering of chiral colloidal liquid crystals using dna origami, *Nat. Mater.* **2017**, *16*, 849–856.
11. J. Yeom, U. S. Santos, M. Chekini, M. Cha, A. F. de Moura & N. A. Kotov. Chiromagnetic nanoparticles and gels, *Science* **2018**, *359*, 309–314.
12. G. T. Pickett, M. Gross & H. Okuyama. Spontaneous chirality in simple systems, *Phys. Rev. Lett.* **2000**, *85*, 3652–3655.
13. A. Mughal, H. K. Chan & D. Weaire. Phyllotactic description of hard sphere packing in cylindrical channels, *Phys. Rev. Lett.* **2011**, *106*, 115704.
14. A. Mughal, H. K. Chan, D. Weaire & S. Hutzler. Dense packings of spheres in cylinders: Simulations, *Phys. Rev. E* **2012**, *85*, 051305.

15. L. Fu, C. Bian, C. W. Shields IV, D. F. Cruz, G. P. López & P. Charbonneau. Assembly of hard spheres in a cylinder: A computational and experimental study, *Soft Matter* **2017**, *13*, 3296–3306.
16. F. Li, X. Badel, J. Linnros & J. B. Wiley. Fabrication of colloidal crystals with tubular-like packings, *J. Am. Chem. Soc.* **2005**, *127*, 3268–3269.
17. Y. Yin & Y. Xia. Self-assembly of spherical colloids into helical chains with well-controlled handedness, *J. Am. Chem. Soc.* **2003**, *125*, 2048–2049.
18. L. Jiang, J. W. J. de Folter, J. Huang, A. P. Philipse, W. K. Kegel & A. V. Petukhov. Helical colloidal sphere structures through thermo-reversible co-assembly with molecular microtubes, *Angew. Chem. Int. Ed.* **2013**, *52*, 3364–3368.
19. J. W. J. de Folter, P. Liu, L. Jiang, A. Kuijk, H. E. Bakker, A. Imhof, A. van Blaaderen, J. Huang, W. K. Kegel, A. P. Philipse & A. V. Petukhov. Self-organization of anisotropic and binary colloids in thermo-switchable 1D microconfinement, *Part. Part. Syst. Charact.* **2015**, *32*, 313–320.
20. P. Liu, J. W. J. de Folter, A. V. Petukhov & A. P. Philipse. Reconfigurable assembly of superparamagnetic colloids confined in thermo-reversible microtubes, *Soft Matter* **2015**, *11*, 6201–6211.
21. L. Jiang, Y. Peng, Y. Yan, M. Deng, Y. Wang & J. Huang. “Annular Ring” microtubes formed by SDS@2β-CD complexes in aqueous solution, *Soft Matter* **2010**, *6*, 1731–1736.
22. S. Ouhajji, J. Landman, S. Prévost, L. Jiang, A. P. Philipse & A. V. Petukhov. In situ observation of self-assembly of sugars and surfactants from nanometres to microns, *Soft Matter* **2017**, *13*, 2421–2425.
23. G. Gübitz & M. G. Schmid. Chiral separation by chromatographic and electromigration techniques. a review, *Biopharm. Drug Dispos.* **2001**, *22*, 291–336.
24. M. Aristov, R. Eichhorn & C. Bechinger. Separation of chiral colloidal particles in a helical flow field, *Soft Matter* **2013**, *9*, 2525–2530.
25. C. Noguez & I. L. Garzón. Optically active metal nanoparticles, *Chem. Soc. Rev.* **2009**, *38*, 757–771.

6

Depletion-Induced Chiral Chain Formation of Magnetic Spheres in an External Field

Abstract

The theoretical prediction that dipolar hard spheres with additional isotropic attraction form chiral configurations, is experimentally tested employing magnetic colloids and depleting polymers. An external magnetic field aligns superparamagnetic silica spheres in the presence of poly(ethylene oxide) polymers. For specific depletant concentrations, chains of spheres are found to wind around each other forming helical structures. These structures maximize overlap of exclusion zones between neighbouring spheres and, hence, lower the free energy of the system.

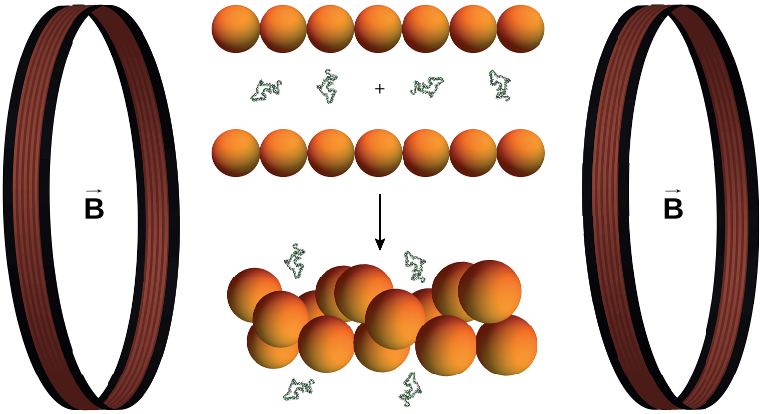

6.1 Introduction

In Chapter 5, we outlined a synthetic strategy for the assembly of chiral colloids by confining isotropic photo-responsive spheres in microtubes. Upon irradiation with UV-light and removal of the confining tubes, a library of structures was obtained, including helical sphere chains. Our results confirmed the prediction that isotropic spheres can form helical structures upon cylindrical confinement.[1]

Another example of spontaneous chiral symmetry breaking exists; dipolar hard spheres with an additional attractive interaction are predicted to exhibit chiral ground states.[1] Numerical simulations have been performed with 15 aligned spheres with embedded dipole moments, resulting in the phase diagram in Figure 6.1. For certain values of ϵ and R, the strength and range of the attractive interaction respectively, helical structures are formed. The observed chiral states mainly consist of three chains winding around each other. In a helical arrangement, each sphere has more neighbours compared to a linear achiral chain, thus lowering the system's free energy.

In this Chapter, we probe experimentally if unconfined dipolar particles with an isotropic attraction indeed arrange into helical chains. To this end, we employ negatively charged superparamagnetic silica spheres as dipolar spheres. Salt is added to diminish the Debye length and to effectively obtain dipolar hard spheres. Addition of the polymer poly(ethylene oxide) generates an additional attraction between the particles in the form of depletion interaction. An external magnetic field is applied to align the magnetic particles in a sea of depletants with varying concentrations.

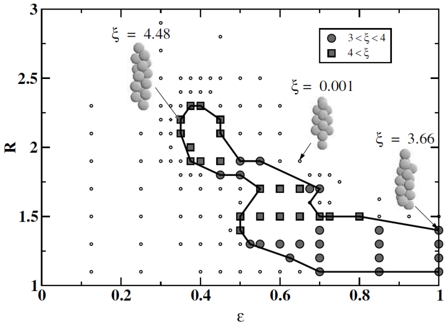

Figure 6.1: Phase diagram of unconfined dipolar spheres. The bold line contains all chiral ground states as a function of strength ϵ and range R of the attraction. The open circles indicate achiral ground states. ξ indicates the chiral order parameter. Reprinted with permission from Pickett et al.[1] Copyright 2000 by the American Physical Society.

6.2 Experimental Methods

6.2.1 Materials. Superparamagnetic silica colloids in water with a specified diameter of 0.51 μm ± 0.03 μm and iron oxide content $\geq$30% were purchased from microParticles GmbH. Poly(ethylene oxide) (PEO, 600 kDa) was purchased from Sigma-Aldrich, sodium chloride (p.a.) from Merck and sodium azide ($\geq$99%) from Fisher Scientific. All chemicals were used as received. The water used for all syntheses was purified using a Milli-Q water purification system.

6.2.2 Magnetic Field. An external horizontal magnetic field was induced by two permanent magnets (Geomag) placed equidistantly from the sample contained in a capillary. The distance between the magnets was chosen such that the strength of the magnetic field in the sample was about 3 mT as determined with a gaussmeter. To induce a homogeneous magnetic field of 3 mT or 1.4 mT, a Helmholtz cube was used (see Section 4.3.3). A magnetic field of 3 mT results in an interaction strength on the order of 65 $k_B T$; sufficiently large to induce chain formation of superparamagnetic silica spheres.

6.2.3 Optical Microscopy. Optical microscopy images were obtained using a Nikon Eclipse Ti-E inverted microscope equipped with a *the Imaging Source* DMK 23UX174 Digital Camera. A Nikon CFI Plan Fluor objective (60× magnification, N.A. 0.85) or Nikon CFI Apo TIRF objective (100× magnification, N.A. 1.49) was used. The images in Figures 6.3 and 6.4 were obtained with a Nikon Ti-U inverted microscope equipped with a Nikon Plan Apo VC objective (100× magnification, N.A. 1.40) and a Lumenera Infinity X camera. Pictures were recorded in bright field mode. Samples were prepared by filling hollow glass tubes (0.1×2×50 mm, VitroCom) by capillary action. The tubes were sealed with optical adhesive (Norland 81) that was cured with UV-light (wavelength of 365 nm, 6 W UVP UVGL-58 lamp). Samples consisted of varying concentrations superparamagnetic colloids and PEO, and 10 mM salt. Sodium azide was added, if necessary, to prevent interference from bacteria.

6.3 Results and Discussion

6.3.1 Model System. Two batches of commercial superparamagnetic silica spheres were used with diameters ($2R_c$) of 566 ± 18 nm and 548 ± 14 nm, see Section 4.3.1. 10 mM salt was added to reduce the Debye screening length to 3 nm (see Appendix 6.A). At this ionic strength, colloidal stability was maintained while the

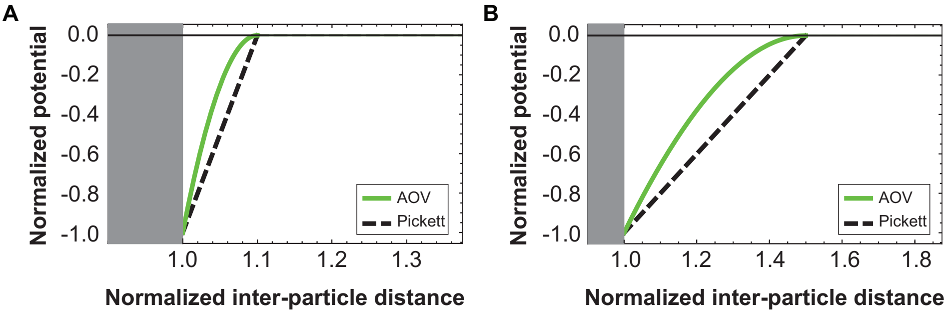

Figure 6.2: Comparison of potentials. AOV potential and the potential as given in Equation 6.1 (denoted here as Pickett potential) normalized to the contact potential as a function of normalized inter-particle distance for (a) q = 0.1 and (b) q = 0.5. For small q, the two potentials are fairly similar.

double-layer interactions were considerably screened. PEO with a molecular weight of 600 kDa that was employed as depletant is consistent with a (calculated) radius of gyration R_g of 50 nm (see Appendix 6.A).[2] The size ratio q of the depletion interaction is thus equal to $R_g/R_c = 0.18$.

In the numerical simulations by Pickett et al., the applied pairwise attractive potential was modelled by:[1]

$$U_{\text{attr}}(r) = \begin{cases} -\epsilon \frac{R-r}{R-2R_c} & 2R_c \leq r \leq R \\ 0 & \text{otherwise} \end{cases}, \tag{6.1}$$

as a function of the distance r between two spheres. Here, ϵ defines the strength and R the range of the attraction. In Figure 6.2 it is shown that in the limit of small q, the Asakura-Oosawa-Vrij (AOV) depletion potential[3,4] approximates the potential given in Equation 6.1 reasonably well. To compare the two potentials, the following conversion was applied: $R = q + 1$.

6.3.2 Inhomogeneous Magnetic Field. Two permanent magnets were used to induce a horizontal magnetic field. Samples were studied containing 50 mg/mL superparamagnetic silica particles, 10 mM sodium chloride and PEO concentrations ranging from 0.1 mg/mL to 1 mg/mL (corresponding depletion potential of 0.5 to 6 k_BT). Mostly linear chains of spheres were observed and occasionally chains formed ribbons with widths larger than one particle diameter by (reversible) lateral aggregation,[5] see Figure 6.3. For two specific PEO concentrations helical structures were observed, see Figure 6.4. These long chains of entwined spherical particles did not form in the absence of depletant.

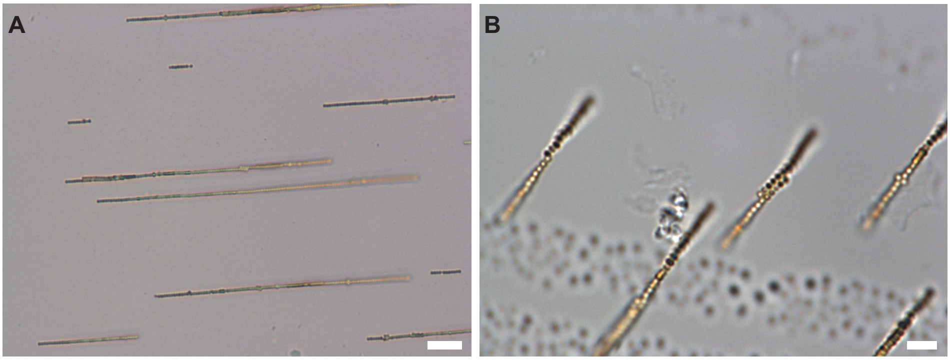

Figure 6.3: Linear sphere chains. Linear chains of magnetic spheres were formed for most concentrations of PEO. Lateral aggregation of different chains was observed occasionally. (a) 0.13 mg/mL PEO; scale bar is 5 μm. (b) 1 mg/mL PEO; scale bar is 3 μm.

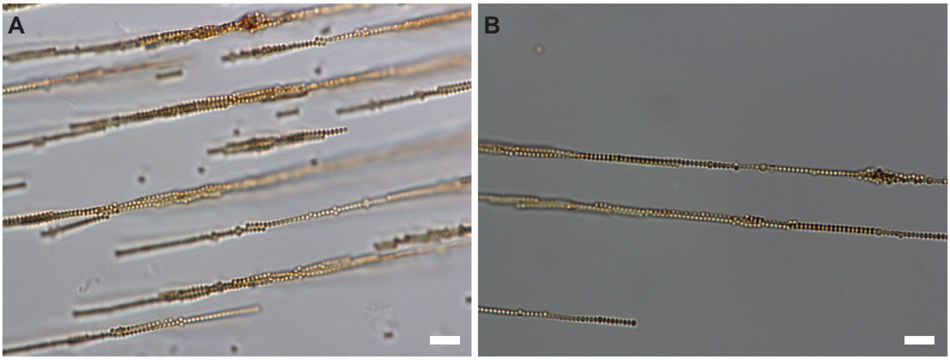

Figure 6.4: Helical sphere chains. At two concentrations of PEO, (a) 0.14 mg/mL and (b) 0.16 mg/mL, linear chains of spheres were found to wind around each other. Scale bars are 3 μm.

6.3.3 Homogeneous Magnetic Field. In a homogeneous magnetic field of 3 mT, mixtures of magnetic silica spheres, salt and depletant do not form chiral structures, see Figure 6.5. By lowering the magnetic field strength to 1.4 mT, two adjacent linear sphere chains wind around each other at three depletant concentrations, see Figure

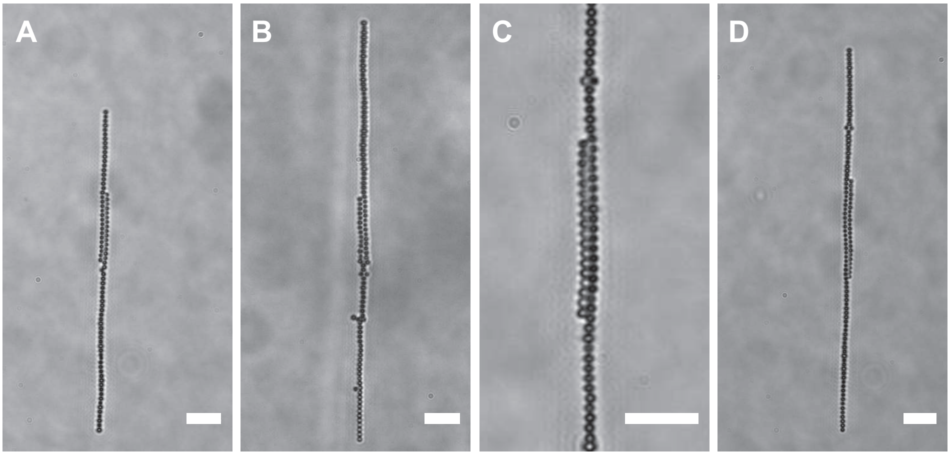

Figure 6.5: Linear sphere chains. In a homogeneous magnetic field of 3 mT linear sphere chains are formed for all studied concentrations of PEO. (a) 0 mg/mL, (b) 0.10 mg/mL, (c) 0.14 mg/mL and (d) 0.16 mg/mL PEO. Scale bars are 5 μm.

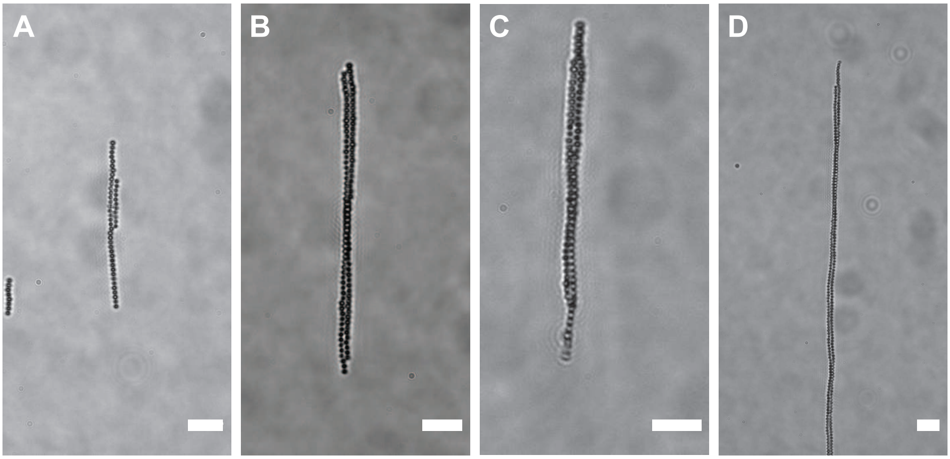

Figure 6.6: Helical sphere chains. In a homogeneous magnetic field of 1.4 mT, long chains of spheres wind around each other forming helical chains in the presence of depletant. (a) 0 mg/mL, (b) 0.10 mg/mL, (c) 0.14 mg/mL and (d) 0.16 mg/mL PEO. Scale bars are 5 μm.

6.6. The dipole-dipole interaction is weaker at 1.4 mT compared to 3 mT allowing the particles to move more freely and explore more configurations. However, this does not explain why helical chains do form in an inhomogeneous field of 3 mT. Perhaps the gradient in particle concentration as a consequence of the inhomogeneity in magnetic field strength affects the configurations of the chains.

6.4 Conclusions and Outlook

The theoretical prediction that unconfined dipolar spheres can form helical structures was experimentally tested. Superparamagnetic silica spheres were aligned in a magnetic field in the presence of depletion polymer. Helical structures consisting of linear sphere chains winding around each other were observed in homogeneous and inhomogeneous magnetic fields. More experiments are needed to definitively confirm the prediction and to determine the concentration range in which helical configurations are formed. Furthermore, the range of the interaction can be tuned by varying the size of the depletant. As the depletion interaction between spheres and walls is twice as large as between spheres, the wall of the glass capillary should be coated with the depletant to eliminate possible wall effects. Finally, the silica spheres could be functionalized with photo-responsive coumarin molecules to obtain permanent helical structures in the absence of a magnetic field.

6.5 Acknowledgements

Sandrine Heijnen and Patrick van Vliet are acknowledged for performing most of the experiments described here and Álvaro González García is thanked for the comparison of the AOV and Pickett potentials and useful discussions. Bonny Kuipers is acknowledged for designing the Helmholtz setup. We thank Marcel van Asselen of the Engineering group of the Scientific Instrumentation department for the mechanical design and Manfred van den Berg, Helge Veltman and co-workers of the Production group for the realization of the Helmholtz setup.

Appendix 6.A Calculations

Debye Screening Length. The electric potential profile surrounding a colloidal particle approaches zero at a distance of several times the Debye screening length κ^{-1} given by:

$$\kappa^{-1} = \sqrt{\frac{\epsilon_0 \epsilon_r k_\mathrm{B} T}{2e^2 n_0}}. \tag{6.1}$$

Here, ϵ_0 is the vacuum permittivity, ϵ_r is the dielectric constant of the medium, k_B is the Boltzmann constant, T is the absolute temperature, e is the elementary charge and n_0 the particle density at the point where the field is zero. In water at 25 °C, Equation 6.1 reduces to:

$$\kappa^{-1} = \frac{0.30}{\sqrt{c}}\ \mathrm{nm}, \tag{6.2}$$

with c the salt concentration in mol/L.[6]

Radius of Gyration. Devanand and Selser studied the behaviour of PEO in water with static and dynamic light scattering measurements.[2] In a good solvent, the following relation holds between the radius of gyration R_g and molecular weight M_w (in g/mol):

$$R_g = 0.215 M_w^{0.583 \pm 0.031}\ \text{Å} \tag{6.3}$$

Depletion Potential. The depletion potential between two spheres $W(h)$ due to ideal polymers is, in the Derjaguin approximation, given by:[4]

$$W(h) = -n_b k_\mathrm{B} T R_c R_g^2 (4\pi \ln 2 - 4\sqrt{\pi}\frac{h}{R_g} + \frac{\pi}{2}\frac{h^2}{R_g^2}). \tag{6.4}$$

Here, n_b is the bulk number density of ideal polymers, R_c is the radius of the spheres, R_g is the radius of gyration of the polymer and h is the separation between two spheres. The strength of the interaction or the depth of the potential ϵ at contact ($h = 0$) is thus:

$$\epsilon = \frac{W(h)}{k_\mathrm{B} T} = -n_b R_c R_g^2 4\pi \ln 2 \tag{6.5}$$

References

1. G. T. Pickett, M. Gross & H. Okuyama. Spontaneous chirality in simple systems, *Phys. Rev. Lett.* **2000**, *85*, 3652–3655.
2. K. Devanand & J. C. Selser. Asymptotic behavior and long-range interactions in aqueous solutions of poly(ethylene oxide), *Macromolecules* **1991**, *24*, 5943–5947.

3. S. Asakura & F. Oosawa. On interaction between two bodies immersed in a solution of macromolecules, *J. Chem. Phys.* **1954**, *22*, 1255–1256.
4. H. N. W. Lekkerkerker & R. Tuinier. *Colloids and the Depletion Interaction*, Springer Netherlands, **2011**.
5. A. Darras, J. Fiscina, M. Pakpour, N. Vandewalle & G. Lumay. Ribbons of superparamagnetic colloids in magnetic field, *Eur. Phys. J. E* **2016**, *39*, 47.
6. J. N. Israelachvili. *Intermolecular and Surface Forces (Third Edition)*, Academic Press, **2011**.

7

Observation of the Brownian Motion of a Colloidal Helix

Abstract

Mapping the Brownian motion of non-spherical particles is more complex than for spheres due to coupling between translational and rotational degrees of freedom. Here, we show how digital holographic microscopy, confocal microscopy and optical tweezers are employed to observe the Brownian motion of non-spherical particles that were prepared in Chapter 5. In particular, linear, zigzag and helical sphere chains are investigated.

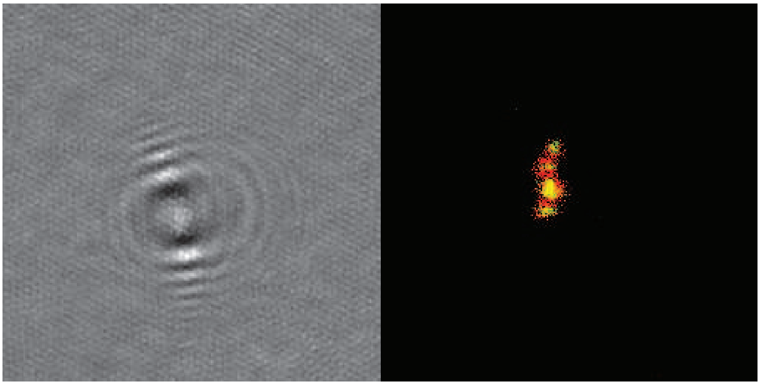

7.1 Introduction

Brownian motion has been extensively studied using spherical colloids as model systems. For spheres at low Reynolds number, the translational diffusion coefficient is related to the Stokes friction factor via the Stokes-Einstein equation.[1–3] Whereas the translation and rotation of spheres is uncorrelated and decoupled,[4] the dynamics of non-spherical colloids is more complex; coupling between translational and rotational degrees of freedom arises since particles exhibit translations due to rotations and vice versa.

Han et al.,[5] for example, investigated the 2D Brownian motion of an ellipsoid in water. The translational diffusion of an ellipsoid is characterized by two hydrodynamic friction coefficients for motion parallel and perpendicular to its long axis, respectively. A crossover from short-time anisotropic to long-time isotropic diffusion was found. Kraft et al.[6] extracted the hydrodynamic friction tensor for colloidal particles with various anisotropic shapes using confocal microscopy. Their results showed coupling between translation and rotation for irregular, asymmetric particles. The Brownian motion of a chiral bacteria was quantitatively studied in 3D with confocal microscopy.[7] Translational and rotational diffusion coefficients of the circular helical microorganism were determined, but their coupling was not explored. Finally, chiral colloidal molecules were synthesized by Schamel et al.[8] to demonstrate the propeller effect. By applying a rotating magnetic field, a racemic mixture of helices can be separated due to shape-induced rotation-translation coupling.

To characterize Brownian motion in 3D, usually confocal microscopy is utilized.[9] Confocal microscopy allows for precise determination of particle locations, but requires fluorescently labelled particles. Furthermore, this technique relies on scanning through a volume and is thus limited to studying processes occurring at time scales slower than the acquisition times which is on the order of a second.[10] Digital holographic microscopy is an alternative technique capable of resolving the positions and orientations of particles in three dimensions.[10] Laser light scatters off a particle and the interference pattern between the scattered and unscattered light is recorded by a camera, see Figure 7.1a. The recorded image is called a hologram and consists of circular fringes encoding particle positions in x, y and z.[11] One of the advantages of digital holographic microscopy is that it does not require labelling of particles; the major disadvantage is that the reconstruction of 3D images is computationally very expensive.

Here, we study the dynamics of some of the assemblies described in Chapter 5. A combination of confocal laser scanning microscopy (CLSM), digital holographic

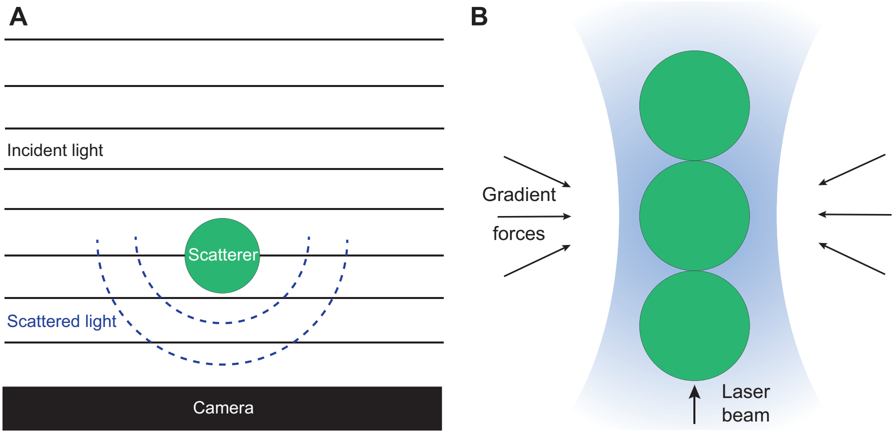

Figure 7.1: Schematic overview of digital holographic microscopy and an optical trap. (a) A coherent plane wave is scattered by a particle. The interference pattern between the scattered and unscattered light, the hologram, is recorded by a camera. (b) The radiation pressure of a highly focused laser beam traps colloidal dielectric objects. The produced gradient forces align a chain of spheres with the optical axis.

microscopy (DHM) and optical traps are used to record the Brownian motion of linear, zipper and helical sphere chains, among others. Optical traps[12] are used to physically and non-destructively hold and move particles, see Figure 7.1b.

7.2 Experimental Methods

7.2.1 Materials. Glycerol (≥ 99.5%) was purchased from Sigma-Aldrich and Cyanine3 NHS ester (Cy3, ≥ 95%) from Lumiprobe. All chemicals were used as received. Cy3 was stored in the dark at −20 °C. The water used in all experiments was purified using a Millipore Direct-Q purification system.

7.2.2 Fluorescent Polystyrene Particles. Dispersions containing linear, zigzag, zipper and helical sphere chains, synthesized as described in Chapter 5, were fluorescently labelled with Cy3. A stock solution of Cy3 in water was prepared with a concentration of 0.4 g/L. In an Eppendorf tube (1.5 mL), 40 μL dye solution, 210 μL water and 250 μL particle dispersion (1 wt%) were mixed and the tube was placed on a tube roller for 24 hours. The particles were washed with water three times by means of centrifugation and redispersion cycles to remove unabsorbed dye.

7.2.3 Microscopy. An Olympus inverted microscope with a Thorlabs system, a piezo scanner and a 60× apochromat oil objective was used to obtain CLSM images. A laser with a wavelength of 532 nm excited the Cy3 dye. The fluorescence emitted and the light scattered by the particles were collected separately on two photomultipliers. Typically, 500 z-stacks were recorded in a volume of 27.5×27.5×5—10 μm (xyz) with a resolution of 0.1 μm/pixel in xy and a step size of 0.1 μm in z. Particles were imaged in glycerol/water mixtures (9:1, w/w) to slow down the Brownian dynamics.

For simultaneous in-line digital holographic microscopy with 405 nm laser trans-illumination and optical trapping, the set-up as described by Curran et al.[13] was used. Videos were recorded with 250 fps for the duration of 1000-10000 frames and were normalised by the median of all frames. Aqueous dispersions were imaged to maximize the optical contrast mismatch between particles and solvent.

Samples were prepared by placing 5-10 μL dispersion between a microscope slide (76×26 mm, Menzel-Gläser) and a 0.17 mm cover slip (22×22 mm, Menzel-Gläser) with two 0.10 mm cover glasses as spacers (22×22 mm, VWR). Cells were sealed with glue (Norland optical adhesive 81) that was cured with UV-light. Very dilute particle dispersions were employed to study single-particle behaviour.

7.3 Results and Discussion

7.3.1 Fluorescent Polystyrene Particles. As polystyrene particle surfaces do not contain any functional groups, it is not trivial to fluorescently label polystyrene. Fluorescent monomers could be added during the dispersion polymerization of styrene, but these monomers are generally not commercially available.[14] Furthermore, addition of fluorescent monomers easily results in aggregation of the particles during synthesis. Another option is the reaction of fluorescent molecules with surface-initiated polystyrene, but this leads to hydrophobic surfaces and fluorescence confined to the surface. Growing a layer of bare polystyrene could solve this problem, though core-shell particles are relatively large.

Therefore, we have chosen to physically adsorb dye in our particles. Cy3 dye was selected due to its strong fluorescence and hydrophobicity. The dye thus has more affinity for the hydrophobic matrix of polystyrene instead of the aqueous solvent. The advantage of this approach is the ease with which particles can be labelled. The obvious disadvantage is the fact that the dye is not covalently bound and can leak out of the particles.

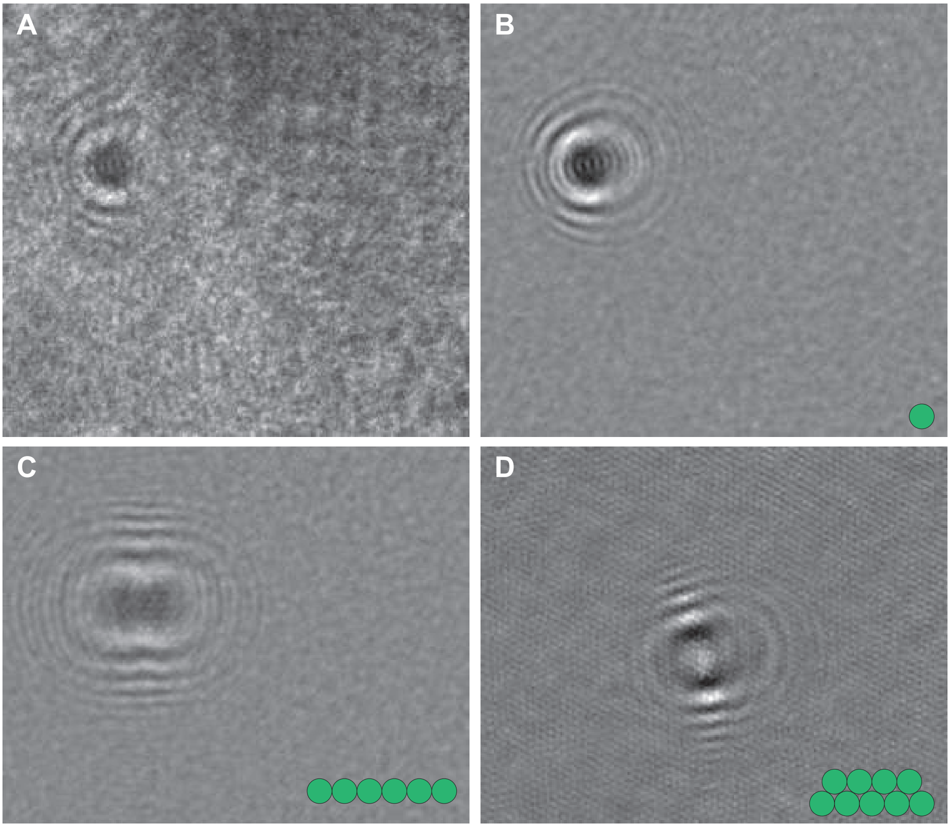

Figure 7.2: Digital holographic microscopy images. (a) Hologram obtained from DHM. (b) Image in (a) normalized to the median of all frames; a linear chain in a vertical, upright position. (c) A linear chain in a horizontal position. (d) A zigzag chain, horizontally oriented. Insets show models of the nature and orientation of the captured particles.

7.3.2 Digital Holographic Microscopy. Figure 7.2a shows a hologram recorded by DHM and Figure 7.2b displays the same hologram normalized to the mean of all frames to eliminate the non-moving background. Concentric rings with varying intensity, number and diameter can be observed. The interference pattern discloses the location and orientation of the particles. The centre of the rings contains information about the positions perpendicular to the optical axis (in x and y) whereas the spacing between the rings reveals the position along the optical axis (in z). The nearly symmetric concentric rings in Figure 7.2b, for example, indicate that a linear chain of spheres is positioned vertically, with a slight tilt. The elongated rings in Figure 7.2c, on the other hand, are of the same linear chain but in a horizontal orientation. A zipper chain can give rise to an intriguing hologram with curved wings, see Figure 7.2d.

Very dilute samples were prepared with one particle per visualized volume to avoid overlapping holograms. To extract the 3D dynamics, holographic reconstructions have to be numerically computed. This requires enormous processing power especially when analysing a collection of spheres. As a result, we were unable to recover quantitative data.

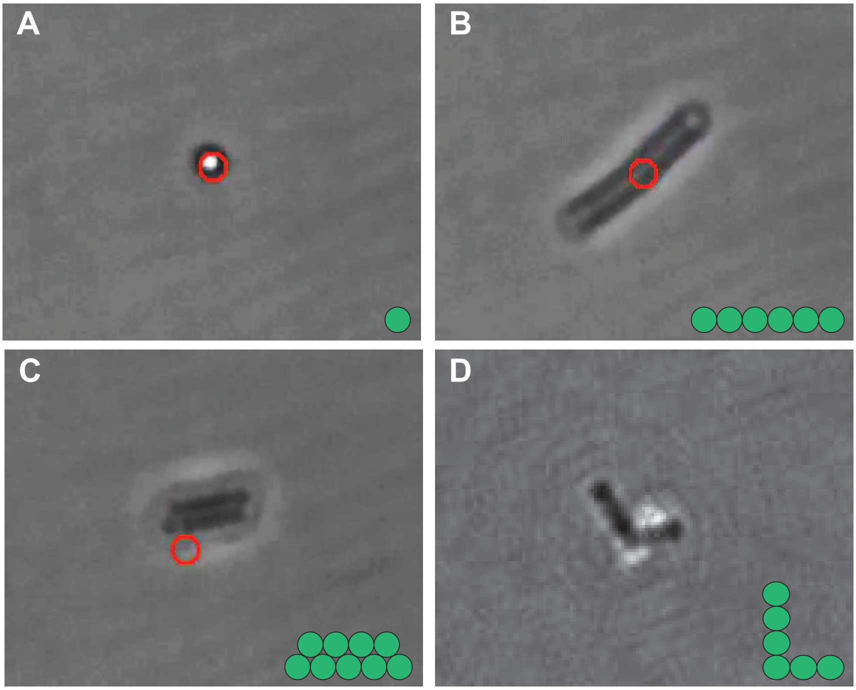

Figure 7.3: Sphere chains in an optical trap. (a) A linear chain in a vertical, upright position, aligned with the optical axis. (b) By introducing an aberration in the trap, the linear chain in (a) is forced in a horizontal position. (c) A trapped zigzag chain. (d) Hologram of an L-shaped particle in a trap. Insets show models of the nature and orientation of the chains. Red circles indicate the approximate position of the trap.

7.3.3 Optical Trapping. Optical traps facilitate the study of single particle dynamics as a particle can be held in place and moved around by a highly focused laser beam. The particle can then be dragged to another location, away from other particles. As the produced gradient forces trap any particle in a certain radius from the trap, the need for dilute suspensions remains.

A trapped chain of particles orients itself parallel to the optical axis of the trap, see Figure 7.3a. By introducing an aberration in the laser beam, a trap can be elongated to accommodate a horizontally oriented linear chain, effectively forcing a particle to change its orientation, see Figure 7.3b,c. In combination with DHM, see Figure 7.3d, holograms can be recorded for a longer time period by preventing particles from moving outside the field of view. Inside an optical trap, particles still exhibit Brownian motion.

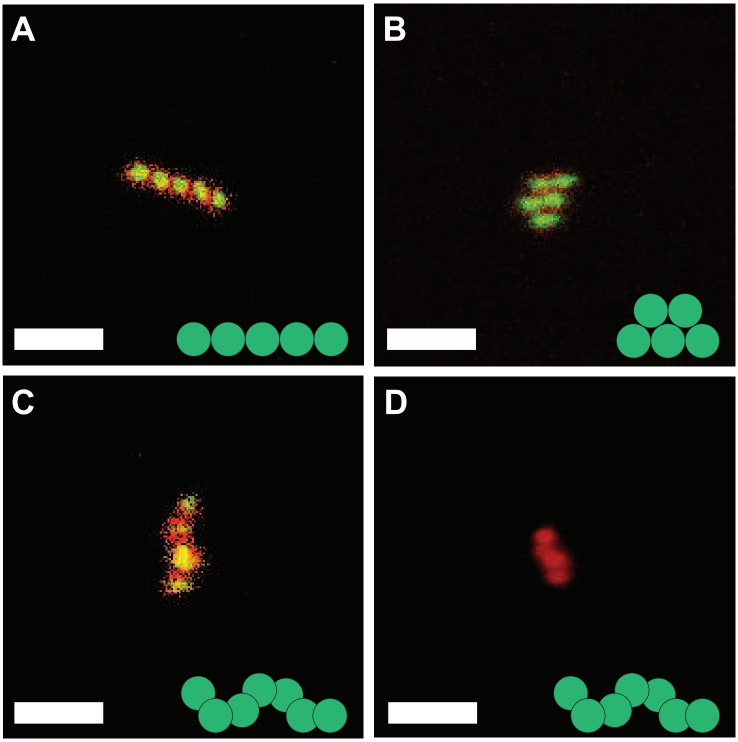

Figure 7.4: Confocal microscopy images. Z-projection of (a) a linear sphere chain, (b) a zipper chain and (c) a single helical chain. (d) 3D image stack of the chain in (c). Scale bars are 5 μm. Fluorescence intensity is indicated in red and scattered light in green. Insets show models of the chains.

7.3.4 Confocal Microscopy. Fluorescent polystyrene sphere chains were dispersed in glycerol/water mixtures to slow down the Brownian dynamics. Due to the relatively small size of the spheres, close to the resolution limit of microscopy, it was difficult to accurately image the chains for tracking the orientation of the chains. Furthermore, the resolution in z is smaller than in x or y, reducing the quality of the z-stacks.

Samples were very dilute to study the motion of single particles. As a result, it was difficult to find helical chains whose overall yield in a 1 wt% dispersion is less than 10% (see Chapter 5). Linear chains, on the other hand, were ubiquitously available. Characteristic confocal images can be found in Figure 7.4.

7.4 Conclusions and Outlook

The Brownian motion of non-spherical colloids that were synthesized in Chapter 5, was captured in 3D with digital holographic microscopy and confocal microscopy. Particles were labelled with fluorescent dye for confocal imaging. Unfortunately, the size of the spheres making up the observed chains was too close to the resolution limit to allow proper visualization and subsequent analysis. In theory, DHM is ideal for determining particle positions and orientations. In practice, however, the analysis of holograms is not trivial as it requires exceptional computational power. Further research will have to be conducted to extract particle positions and orientations from the confocal data. To determine shape-induced rotation-translation coupling in 3D, it might be sufficient to model the helical sphere chain with a rod.

Acknowledgements

Louis Cortes is acknowledged for help with confocal microscopy and analysis of the confocal data. Arran Curran is thanked for help with microscopes in general, optical trapping and DHM in particular. We thank Taiki Yanagishima for introducing us to Cy3 dye.

References

1. A. Einstein. Über die von der molekularkinetischen Theorie der Wärme geforderte Bewegung von in ruhenden Flüssigkeiten suspendierten Teilchen, *Ann. Phys.* **1905**, *322*, 549–560.
2. D. F. Evans & H. Wennerström. *The Colloidal Domain: Where Physics, Chemistry, Biology, and Technology Meet*, Wiley-VCH, **1999**.

3. A. P. Philipse. *Brownian Motion: Elements of Colloid Dynamics*, Springer Nature Switzerland AG, **2018**.
4. S. Schütter, J. Roller, A. Kick, J.-M. Meijer & A. Zumbusch. Real-space imaging of translational and rotational dynamics of hard spheres from the fluid to the crystal, *Soft Matter* **2017**, *13*, 8240–8249.
5. Y. Han, A. M. Alsayed, M. Nobili, J. Zhang, T. C. Lubensky & A. G. Yodh. Brownian motion of an ellipsoid, *Science* **2006**, *314*, 626–630.
6. D. J. Kraft, R. Wittkowski, B. ten Hagen, K. V. Edmond, D. J. Pine & H. Löwen. Brownian motion and the hydrodynamic friction tensor for colloidal particles of complex shape, *Phys. Rev. E* **2013**, *88*, 050301.
7. A. V. Butenko, E. Mogilko, L. Amitai, B. Pokroy & E. Sloutskin. Coiled to diffuse: Brownian motion of a helical bacterium, *Langmuir* **2012**, *28*, 12941–12947.
8. D. Schamel, M. Pfeifer, J. G. Gibbs, B. Miksch, A. G. Mark & P. Fischer. Chiral colloidal molecules and observation of the propeller effect, *J. Am. Chem. Soc.* **2013**, *135*, 12353–12359.
9. B. Liu & A. Böker. Measuring rotational diffusion of colloidal spheres with confocal microscopy, *Soft Matter* **2016**, *12*, 6033–6037.
10. V. Manoharan. 'Digital Holographic Microscopy for 3D Imaging of Complex Fluids and Biological Systems' in *Frontiers of Engineering: Reports on Leading-Edge Engineering from the 2009 Symposium*, The National Academies Press, **2010**.
11. J. Fung & V. N. Manoharan. Holographic measurements of anisotropic three-dimensional diffusion of colloidal clusters, *Phys. Rev. E* **2013**, *88*, 020302.
12. D. G. Grier. Optical tweezers in colloid and interface science, *Curr. Opin. Colloid Interface Sci.* **1997**, *2*, 264–270.
13. A. Curran, S. Tuohy, D. G.A. L. Aarts, M. J. Booth, T. Wilson & R. P. A. Dullens. Decoupled and simultaneous three-dimensional imaging and optical manipulation through a single objective, *Optica* **2014**, *1*, 223–226.
14. Q.-H. Liu, J. Liu, J.-C. Guo, X.-L. Yan, D.-H. Wang, L. Chen, F.-Y. Yan & L.-G. Chen. Preparation of polystyrene fluorescent microspheres based on some fluorescent labels, *J. Mater. Chem.* **2009**, *19*, 2018–2025.

PART IV

Active Matter

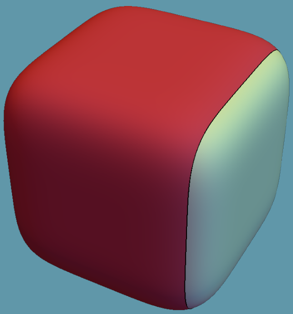

8

Self-Propelling Superballs

Abstract

Cubic microswimmers are realized by half coating superball shaped colloids with platinum that catalyses the decomposition of hydrogen peroxide into water and oxygen. Due to the asymmetric distribution of catalyst on the surface of the colloids, more products than reactants are present on one side of the particles propelling these through self diffusiophoresis. The motion of these self-propelling superballs is characterized experimentally as a function of fuel concentration and temperature; the speed of the active particles increases with both parameters. At short times the particles undergo directed motion, whereas at longer times a random walk with an enhanced diffusion coefficient is observed.

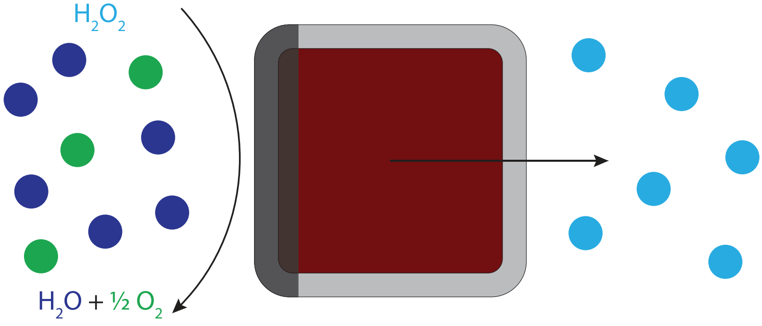

8.1 Introduction

Inspired by nature's microorganisms, such as bacteria and eukaryotic cells, artificial self-propelling particles have been investigated. Directional motion of objects in fluids on the micro- or nanoscale, however, is difficult to realize.[1] On this small scale, the Reynolds number is extremely low, indicating absence of inertial forces and presence of strongly pronounced viscous forces. On a macroscopic scale, swimming mechanisms rely on gliding,[2] whereas a swimmer on microscale will only move if a force is exerted on it. This is visualized by a single hinged miniature scallop[I] achieving no net progress by flapping its arms.[4] To obtain microscale or nanoscale swimmers that propel themselves in an environment with low Reynolds number, a different approach is needed.[1]

Nature uses rotating or wave propagating flagella to self-propel microscale bacteria and cells, but at present most artificial swimming devices require an external power source.[2] Self-phoresis is generally used to power artificial swimmers. Self-phoretic phenomena include self-electrophoresis, self-thermophoresis and self-diffusiophoresis where gradients of respectively electric fields, temperature and concentration lead to net propulsion.[1] One of the most commonly applied approaches is to take advantage of asymmetric chemical reactions; most notably the catalytic dissociation of hydrogen peroxide into water and oxygen.

Nowadays, extensive literature on self-propelling particles or microswimmers can be found. For instance, Howse and co-workers prepared spherical particles with an asymmetric distribution of catalyst on its surface.[1] The platinum cap of these polystyrene spheres generates a concentration gradient by catalytically decomposing hydrogen peroxide. The particles are propelled by the process of self-diffusiophoresis. Baraban et al. showed that polystyrene colloids with a platinum cap can transport a number of equally sized inert polystyrene colloids.[5] Self-propelling spherical platinum-silica particles have also been prepared.[6–8] Silica particles with a magnetically modified platinum cap were shown to be able to load, transport and deliver cargo, exhibiting directional motion under the influence of a magnetic field and self-propulsion.[9] Furthermore, Palacci et al. designed a system of photoactivated self-propelling polymer spheres.[10] Under blue light illumination, these particles catalyse the exothermic chemical decomposition of hydrogen peroxide, creating thermal and chemical gradients that lead to self-propulsion. Dreyfus and co-workers were the first to demonstrate synthetic micro swimming flagella.[11] These were prepared from

---

[I] Purcell's scallop theorem strictly holds only in Newtonian fluids such as water. In non-Newtonian fluids, *e.g.* blood, a microscale scallop could in fact swim by reciprocal motion at low Reynolds number.[3]

a linear chain of colloidal particles that were linked by DNA and attached to a red blood cell that can act as an artificial flexible flagellum. The motion of the artificial swimming devices was controlled by an external oscillatory magnetic field.

These are only a few examples of research that has been conducted in the rapidly expanding field of active colloids. Apart from extensive work on nanorods[12,13] and research conducted by Valadares and co-workers on sphere dimers,[14] most literature in the field of active colloids focuses on spheres (as illustrated by the examples above). In this Chapter the synthesis of novel self-propelling colloidal cubes is discussed. Haematite cubes coated with a tuneable silica layer were synthesized. One side of the cubes was coated with platinum that catalyses the dissociation of hydrogen peroxide. These superballs propagate through self-propulsion, demonstrating ballistic motion at short times and enhanced diffusion at longer time scales.

8.2 Experimental Methods

A schematic overview of the required steps to synthesize self-propelling superballs is given in Figure 8.1.

8.2.1 Materials. Iron(III)chloride hexahydrate ($FeCl_3 \cdot 6\,H_2O$, p.a.), polyvinylpyrrolidone (PVP, 40 kg mol^{-1}), tetraethyl orthosilicate (TEOS, ≥99%), tetramethylammonium hydroxide solution (TMAH, 25 wt% in water), platinum (Pt, evaporation slug, 99.99% trace metals basis) and hydrogen peroxide (H_2O_2, ≥35%) were obtained from Sigma Aldrich. Potassium hydroxide (KOH, powder for synthesis) and sodium hydroxide pellets (NaOH, 98%) were purchased from VWR. Ethanol (100%) was obtained from Interchema. All chemicals were used as received. Only small, unopened pots of iron(III)chloride were used for the synthesis. The water used for all syntheses and experiments was purified using a Milli-Q water purification system.

8.2.2 Synthesis of Silica Coated Haematite Cubes. The synthesis of silica coated haematite cubic colloids is based on the procedure described by Castillo,[15] which in turn derives from the sol-gel method of Sugimoto et al.[16] A 5.02 M sodium hydroxide stock solution was prepared by dissolving 20.08 g sodium hydroxide pellets in 100 mL water. The solution was left to cool to room temperature prior to filling the flask up to the 100 mL mark on the volumetric flask. 50.29 g of iron(III) chloride hexahydrate was weighed as quickly as possible into a 250 mL bottle while keeping the container under a nitrogen gas flow to prevent the highly hygroscopic salt to absorb (more)

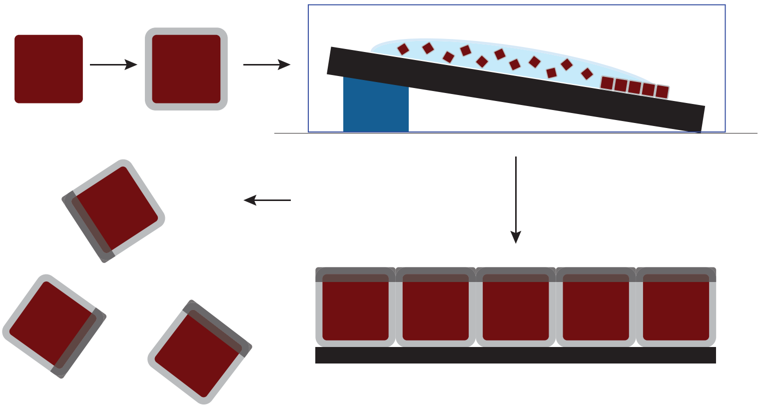

Figure 8.1: Synthesis of self-propelling superballs. Cubic haematite colloids (red) were coated with a silica layer (grey). Silica cubes in dispersion were deposited onto a substrate by means of horizontal deposition under a slight tilt to form a monolayer. Platinum (dark grey), a non-magnetic catalytic metal, was deposited on one face of the cubes. The cubes were detached from the substrate by ultrasonication in water.

water. 100 mL water was added to the salt solution and the solution was sonicated for 20 minutes. The sodium hydroxide solution was continuously added to the iron(III)chloride solution (1.86 M) in less than 30 seconds while stirring magnetically at 1100 rpm. The mixture was stirred for an additional 10 minutes and the resulting gel was placed in a pre-heated oven at 100 °C for 8 days. After the ageing period, the bottle was removed from the oven and left to cool to room temperature. The supernatant was removed and the sol was washed with water (at 800 g for 30 minutes) until the pH reached 5.

An aqueous solution of PVP (35 g/L) was prepared by dissolving 5.32 g of PVP in 150 mL water and sonicating for 20 minutes to ensure complete dissolution. The PVP solution was added to an aqueous dispersion of haematite particles (20 mL, 5.4 wt%) and stirred magnetically overnight. Excess PVP was washed away by centrifugation and redispersion in 20 mL ethanol (at 800 g for 30 minutes). Ethanol (380 mL) was brought into a 1 L round-bottom flask that was suspended in an oil bath and equipped with an overhead stirrer. Water (66 mL), an aqueous TMAH solution (10 mL, 1 wt%) and the ethanolic dispersion of PVP coated haematite colloids were consecutively added to the flask while stirring mechanically and sonicating. A mixture of ethanol (10 mL) and TEOS (10 mL) was added dropwise using a peristaltic pump over the duration of 45 minutes. Finally, 100 mL of an ethanolic PVP solution (200 g/L) was poured into the reaction mixture after sonication for 20 minutes to ensure complete dissolution. The mixture was stirred and sonicated for another 2 hours and only stirred overnight. The resulting dispersion was washed by centrifugation and redispersion in ethanol 3 times (at 800 g for 30 minutes).

8.2.3 Active Cubes. To deposit monolayers of particles on glass substrates, the method of Micheletto et al.[17] was applied. A glass cover slip (22×22×0.17 mm, Menzel-Gläser) was cleaned with water and ethanol and placed, slightly tilted (3°), under a crystallising dish. A 10 μL droplet of aqueous particle dispersion (0.5 wt%) was deposited on the glass surface. The solvent evaporated completely in about 2 hours' time. The monolayer of cubic particles was covered on one face with a 5 nm platinum layer using a sputter coater (Cressington 108). The platinum coated particles were removed from the substrate by sonication in water for approximately one hour.

8.2.4 Optical Microscopy. Optical microscopy was performed using a Nikon Eclipse Ti-E inverted microscope equipped with a Hamamatsu Orca Flash 4.0 V2 Digital Camera. A Nikon CFI Apo TIRF objective (40× magnification, N.A. 1.49 and intermediate magnification of 1.5×) was used. The 2D motion at low particle concentrations was recorded in bright field mode. Typically, a frame rate of 30 fps was used and videos were recorded for the duration of 1500-3000 frames.

Samples consisted of particle dispersion (5 μL, 0.005 wt%), hydrogen peroxide stock solution (195 μL) and TMAH to adjust the pH to 8. Samples were visualized in a home-made microscope sample cell, shown schematically in Figure 8.2a. A bottomless vial (0.5 mL) was glued on top of a microscope slide (76×26 mm, Menzel-Gläser) that was attached unto a glass cover slip (24×60×0.17 mm, Menzel-Gläser). A circular hole was drilled in the microscope slide so that only optical glass was present between the microscope objective and the sample. The vial fits precisely into an aluminium block connected to a Peltier element allowing for temperature control (within $\Delta T = \pm 0.1^\circ$C). Particles were tracked and analysed using a MATLAB script, implementing code written by Grier and Crocker,[18] providing particle trajectory and times.

8.2.5 Characterization. Transmission electron microscopy (TEM) images were taken with a Philips Tecnai10 electron microscope typically operating at 100 kV. Bright field images were recorded using a SIS Megaview II CCD camera. The samples

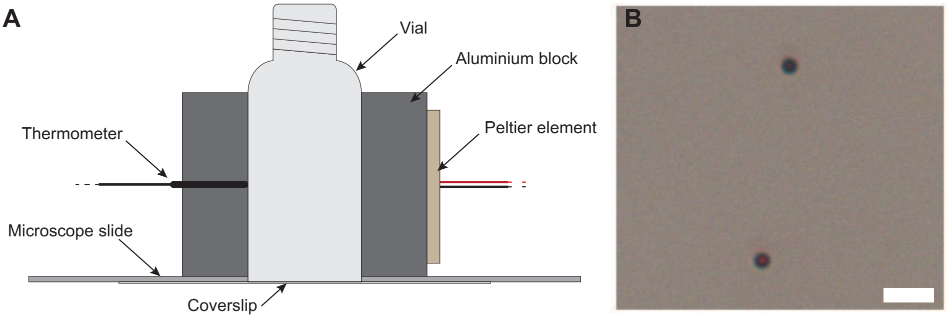

Figure 8.2: Optical microscopy. (a) Schematic of the microscope sample cell that was employed to observe the self-propelling superballs at different temperatures. (b) Representative light microscopy image of two self-propelling superballs; scale bar is 5 μm.

were prepared by drying a drop of diluted aqueous particle dispersion on top of polymer coated copper grids.

Scanning electron microscopy (SEM) images were taken with a Phenom FEI microscope. SEM samples were prepared by sticking a glass substrate with colloidal particles on a stub using a conductive carbon sticker, which was coated with a platinum layer of typically 6 nm.

8.3 Results and Discussion

8.3.1 Synthesis of Self-Propelling Superballs. Silica-coated cubic colloids were synthesized with an average edge length of 980 nm, size polydispersity of 3%, and m value of 3 (see Figure 8.3). A simple (cubic) lattice of the cubes was formed by means of a modified horizontal deposition technique. The slight tilt of the glass substrate ensured that evaporation commenced from the top of the droplet. A crystallising dish was employed to protect the surface from dust and to restrict external air flow thereby slowing down the evaporation process. Typically, different regions of particle deposition could be distinguished on the glass, see Figure 8.4. Apart from densely packed monolayers, dilute monolayers, multiple layers, and transition regions could be observed. The regions that did not exhibit monolayers were removed from the glass and platinum was deposited solely on monolayers of particles. One side of the cubes was thus covered with a catalytic metal that catalyses the decomposition of hydrogen peroxide into water and oxygen, transforming the cubes into active colloids.

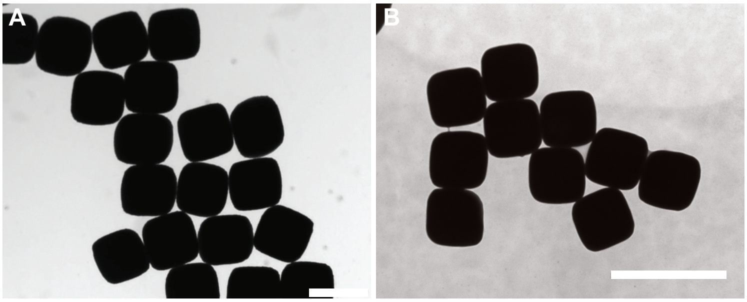

Figure 8.3: TEM images. Representative TEM images of (a) haematite and (b) silica coated haematite cubic colloids. Scale bars are 2 μm.

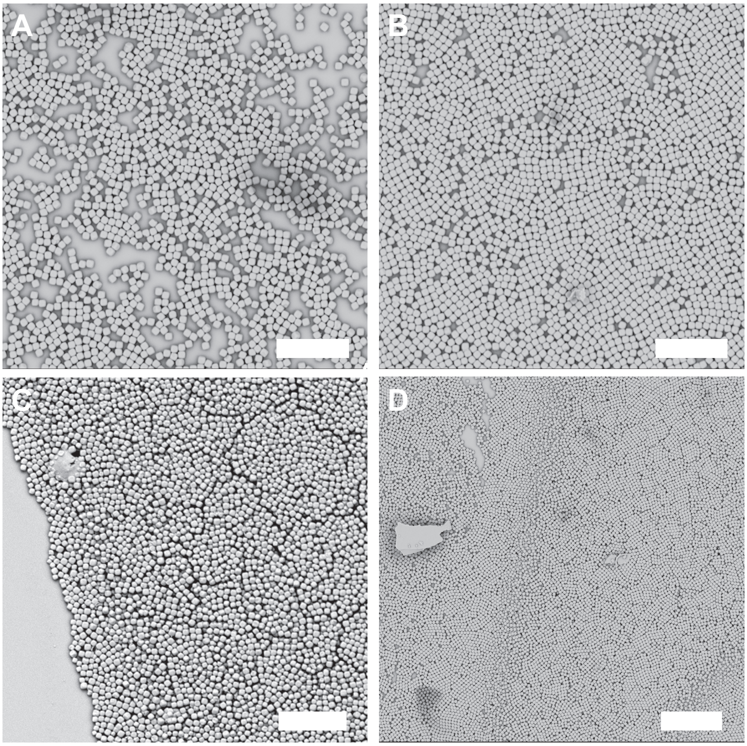

Figure 8.4: SEM images. Deposition of a monolayer typically results in the following areas. (a) A region with a dilute monolayer; scale bar is 10 μm. (b) Densely packed monolayer, where the cubes are locally organized in a simple cubic lattice; scale bar is 10 μm. (c) Multiple layers; scale bar is 10 μm. (d) Transition region from a single layer to multiple layers; scale bar is 20 μm.

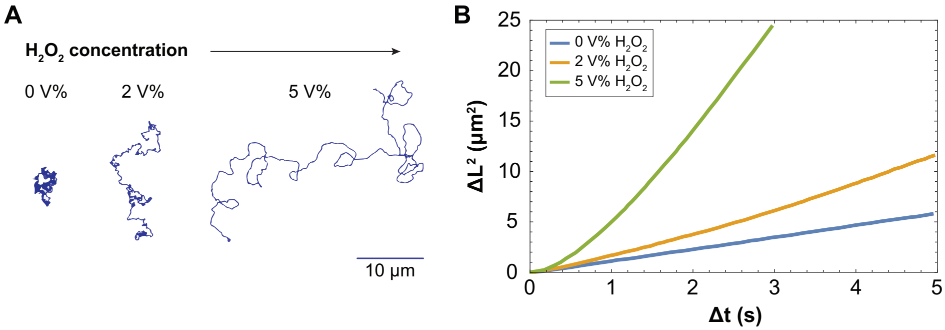

Figure 8.5: Self-propelling superballs. (a) Single-particle trajectories over 50 s of active superballs in 0V%, 2V% and 5V% H_2O_2 solutions in water at 24 °C. (b) Mean squared displacement ΔL^2 as a function of time for the trajectories in (a).

8.3.2 Single-Particle Behaviour. To study the active motion of cubic colloids, self-propelling superballs were dispersed in 2 or 5V% hydrogen peroxide solutions. Higher concentrations of H_2O_2 led to unwanted bubble formation. A very dilute concentration of cubes was utilized to study single-particle behaviour. The silica layer around the cubes effectively minimizes the dipole-dipole interactions between the haematite cores and further ensures that the behaviour we observe is that of single particles. A small amount of TMAH was necessary to prevent the cubes from sticking to the glass. The cubes are quite heavy due to the incorporated haematite core and resided close to the bottom of the microscope cell effectively exhibiting 2D motion. Representative image of self-propelling superballs recorded with optical microscopy is shown in Figure 8.2b. Control samples consisted of platinum-coated cubes in water or uncoated cubes in H_2O_2 undergoing Brownian motion.

Typical trajectories of self-propelling superballs as a function of H_2O_2 concentration are shown in Figure 8.5a. As the H_2O_2 concentration increases, a larger distance is covered. The mean squared displacement ΔL^2, Figure 8.5b, confirms the typical behaviour of active particles: short-time ballistic motion ($\propto t^2$) followed by long-time diffusive motion ($\propto t$). In the absence of fuel, a linear curve is obtained characteristic of Brownian diffusion. The diffusion coefficient D of Brownian superballs can be determined from the slope of the mean squared displacement as $\Delta L^2 = 4D\Delta t$. For $T = 24$°C, D is equal to $0.217\,\mu\text{m}^2\ \text{s}^{-1}$. This is smaller than the theoretical value of the diffusion coefficient calculated from the Stokes-Einstein relation, $D = \frac{k_B T}{6\pi\eta R} = 0.487\,\mu\text{m}^2\ \text{s}^{-1}$. The use of the Stokes friction coefficient for spheres is valid as both the

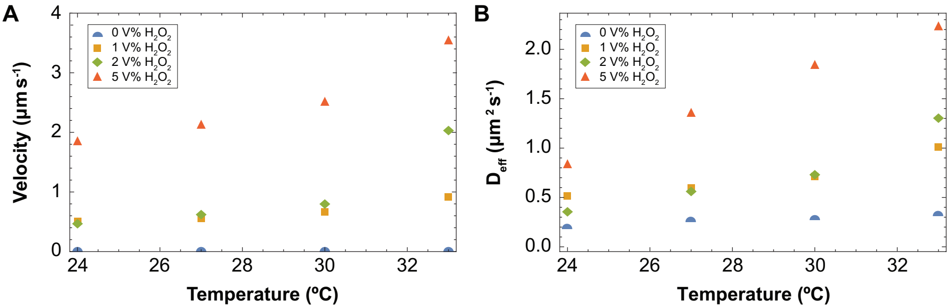

Figure 8.6: Single-particle behaviour of active colloids. (a) Speed determined in the limit of $t \ll \tau$ for active superballs at various H_2O_2 concentrations and as a function of temperature. Speed of the control particles has been set to zero. (b) Effective diffusion coefficients for Pt-coated superballs at various H_2O_2 concentrations in water and as a function of temperature.

translational and rotational diffusion of superballs do not deviate significantly from spheres especially in the limit of low m values, see Appendix 8.A. However, the Stokes friction factor $6\pi\eta R$ is only valid for a sphere in bulk, far away from a surface. A sphere, or a superball, close to a surface will experience enhanced friction resulting in a smaller diffusion coefficient, see Appendix 8.B.

Howse et al.[1] have shown that for a particle propelled with speed V, the 2D projection of mean squared displacement can be described by:

$$\Delta L^2 = 4D\Delta t + \frac{V^2\tau^2}{2}\left[\frac{2\Delta t}{\tau} + e^{\frac{-2\Delta t}{\tau}} - 1\right]. \tag{8.1}$$

Here, V is the propelled speed and τ^{-1} is the rotational diffusion coefficient. At short times, $\Delta t \ll \tau$, Equation 8.1 reduces to:

$$\Delta L^2 = 4D\Delta t + V^2\Delta t^2. \tag{8.2}$$

Fitting plots of ΔL^2 as a function of Δt to Equation 8.2 yields values for the propulsion speed V. Here, D can be employed as a fitting parameter or applied as a constant (value of which was determined for the Brownian superballs, see above). The swimming speed increases with H_2O_2 concentration and with temperature (see Figure 8.6a). At long times, $\Delta t \gg \tau$, randomization of the direction of self-propelling motion occurs due to rotational diffusion and the superball undergoes a random walk:

$$\Delta L^2 = (4D + V^2\tau)\Delta t \tag{8.3}$$

with $4D + V^2\tau$ equal to enhanced diffusion coefficient D_{eff}. From the slope of ΔL^2 of active superballs in the diffusive regime, the effective diffusion coefficient D_{eff} can hence be extracted. Figure 8.6b shows that D_{eff} increases with both fuel concentration and temperature. A higher fuel concentration is correlated with enhanced propulsion as more H_2O_2 is decomposed at the platinum surface, causing a growth in the local concentration gradient. An increase in temperature enhances the effective diffusion by decreasing the viscosity of the fluid.

8.4 Conclusions and Outlook

In this Chapter we have outlined the synthesis of self-propelling superballs. These cubic shaped colloids were obtained by coating a haematite core with silica. On one side of the cubes platinum was deposited, a metal that catalytically decomposes hydrogen peroxide into water and oxygen. The ensuing local concentration gradient propels the particle through self-diffusiophoresis. The self-propelling superballs exhibited typical active behaviour with short time ballistic motion and a random walk with enhanced diffusion coefficient at longer time scales. The rotational diffusion time dictates the crossover between these two regions. The effective or enhanced diffusion coefficient of the active superballs showed an increase as the temperature was raised or more fuel was added.

The haematite core of the silica-coated cubes can be removed by etching with hydrochloric acid yielding hollow silica colloids. The intrinsically porous Stöber silica layer allows for facile diffusion of molecules (cargo) into the hollow cubes which could be transported to and released at a specific location. This is an interesting feature with possible applications in the field of targeted drug delivery that has yet to be explored. In addition, these novel particles could be used to mimic the bacterial navigation of magnetotactic bacteria. Chains of cubic haematite colloids are then powered by an active end cap and these chains are able to swim along the magnetic field lines of the earth, similar to bacteria. By applying an externally applied magnetic field, it is possible to manipulate the trajectories of the artificial bacteria as the magnetic properties of the cubes would allow control over the autonomous motion of the colloids. Finally, at higher overall particle concentrations, the state behaviour of self-propelling superballs could be probed.

8.5 Acknowledgements

Pepijn Moerman is acknowledged for providing the tracking code and for useful discussions. Dennis van Eldik is thanked for performing some of the experiments described here. Dr. Tai-Hsi Fan and Remco Tuinier are acknowledged for the calculation and comparison of the translational and rotational diffusion of superballs and spheres.

Appendix 8.A Superballs vs. Spheres

Appendix Figure 8.1 shows the frictional force or Stokes' drag F of superballs relative to that of a sphere, $6\pi\eta RV$, where V is the velocity of the sphere and η the viscosity of the solvent.[19] The diffusion coefficient which is defined as $D = k_\mathrm{B}T/6\pi\eta R$ thus decreases with increasing m-value. The deviation, however, is even in the limit of large m, almost negligible. For superballs with $m = 3$, as used throughout this Chapter, the diffusion coefficient can thus be closely approximated using the friction factor of a perfect sphere.

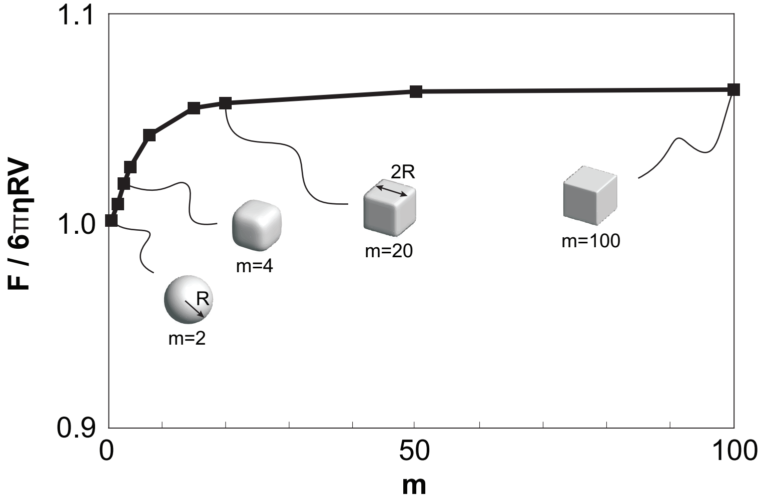

Appendix Figure 8.1: Stokes' drag as a function of the *m*-value of superballs. The Stokes' drag or frictional force of a superball does not differ significantly from that of a sphere. Even for $m = 100$, the deviation from a sphere is less than 7%. Figure adapted from Tuinier and Fan.[19]

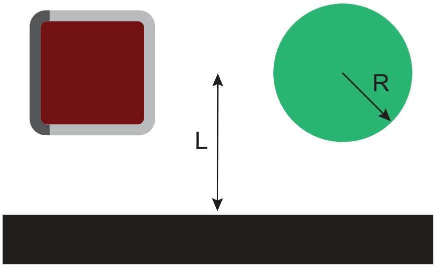

Appendix Figure 8.2: Schematic drawing of a self-propelling superball and a sphere close to a surface. The radius R of the sphere and the distance L from the surface have been indicated.

Appendix 8.B Friction Factor of a Sphere Near a Planar Wall

The experimentally determined and calculated diffusion coefficients for Brownian superballs are not in agreement. However, we have effectively studied the 2D motion of superballs confined to a surface by gravity. For a sphere moving relative to a wall, the friction factor can be approximated by:[20]

$$f \approx \frac{6\pi\eta R}{1-(9/16)(R/L)}. \tag{8.1}$$

Here, η is the viscosity of the solvent, R is the radius of the sphere and L is the distance between the sphere centre and the wall, see Figure 8.2. For a sphere that hovers one particle diameter above the surface, distance $L = 2R$, the friction reduces by a factor of:

$$f \approx \frac{6\pi\eta R}{1-(9/16)(R/2R)} = \frac{6\pi\eta R}{0.72}, \tag{8.2}$$

which corresponds to an increase in f with a factor of 1.4 and a concomitant decrease in D. The drag increase for a superball is expected to be more than that for a sphere due to the larger area that is in contact with the surface.

Appendix 8.C Temperature

The self-propelling superballs did not appear to exhibit active motion below room temperature. This led to the hypothesis that a critical temperature might exist below which self-propelling superballs do not swim (similar to isotropic swimmers).[21] To investigate the effect of temperature on the swimming behaviour, measurements were performed at temperatures below room temperature. To this end, the microscope was

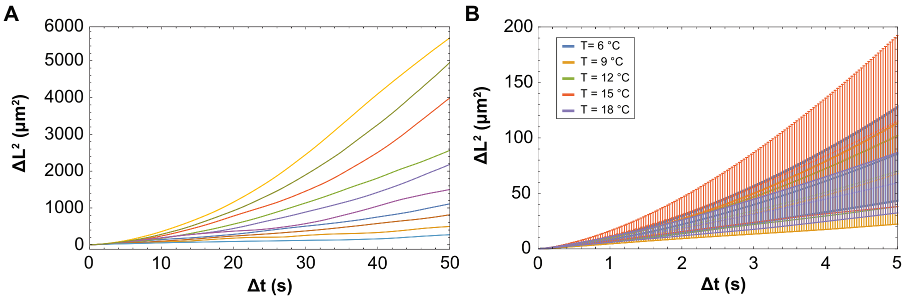

Appendix Figure 8.3: Distribution in mean squared displacement. (a) ΔL^2 as a function of time extracted from 10 single-particle trajectories over 100 s of active superballs in 2V% H_2O_2 solution in water at 9 °C. Each curve is averaged over 3000 frames. (b) Averaged ΔL^2 over maximum 20 particles per temperature for 5V% H_2O_2 concentration, including error bars.

temporarily moved to a temperature controlled room. Measurements were performed at temperatures ranging from 6 to 18 °C (in steps of 3 degrees) in 2 and 5 V% hydrogen peroxide solutions. Both Pt-coated (active) and non-Pt-coated (control) superballs were measured. The single particle behaviour of at least 10 particles per temperature and per concentration was recorded.

The mean squared displacement of the tracked particles shows a large distribution at each temperature and concentration, see Appendix Figure 8.3a. Possible reasons for the large fluctuations include the inherent polydispersities in size, shape, Pt-coating and concentration gradients. The error bars computed for the averaged mean squared displacement are extremely large, making it difficult to draw any conclusions regarding the data, see Appendix Figure 8.3b.

In Appendix Figure 8.4 an overview is given of the averaged ΔL^2 per temperature at the two different H_2O_2 concentrations. No explicit dependence on temperature is observed. The only conclusion that can be drawn is that the particles do seem to be active even at temperatures below room temperature. This statement is further strengthened upon comparison with Brownian particles, see Appendix Figure 8.5. It does seem as if the active particles are slowed down as the temperature increases. This might be because of the haematite core still incorporated inside the superballs. Haematite itself can catalyse the dissociation of hydrogen peroxide into water and oxygen, upon blue light illumination. However, blue light merely acts as a catalyst to accelerate this process. Considering that the silica layer around the haematite core is porous, it is not unlikely that the iron core is decomposing hydrogen peroxide as the particle moves. Perhaps this particular process does have a critical temperature and upon increasing the temperature, the speed of the haematite propulsion increases, counteracting the direction of the Pt propulsion effectively propelling the cubes against the Pt side and thus slowing the particles down. Therefore, at higher T we observe a smaller ΔL^2. However, more experiments are needed to confirm or refute this theory.

In Appendix Figure 8.6 the effective diffusion coefficient and speed of active superballs are shown as a function of temperature. No clear dependence on temperature can be determined for these parameters either. Moreover, the distribution in D_{eff} is remarkably broad, see Appendix Figure 8.7.

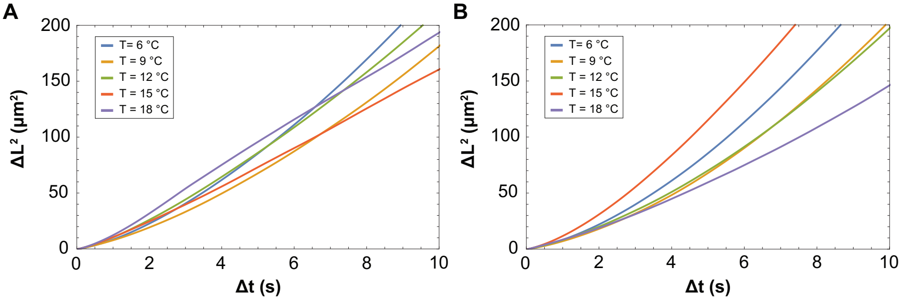

Appendix Figure 8.4: Averaged mean squared displacement of active superballs. Averaged ΔL^2 over maximum 20 particles per temperature for (a) 2V% and (b) 5V% H_2O_2 concentrations in water. Error bars have been omitted for the sake of clarity.

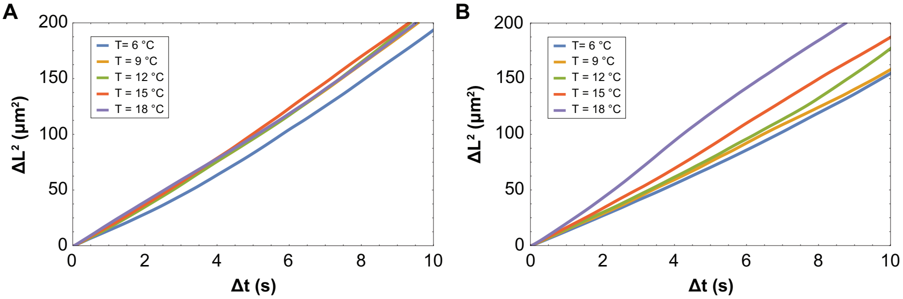

Appendix Figure 8.5: Averaged mean squared displacement of Brownian superballs. Averaged ΔL^2 over maximum 10 uncoated particles per temperature for (a) 2V% and (b) 5V% H_2O_2 concentrations in water. In the absence of Pt, the curves are linear in compliance with Brownian diffusion. Error bars have been omitted for the sake of clarity.

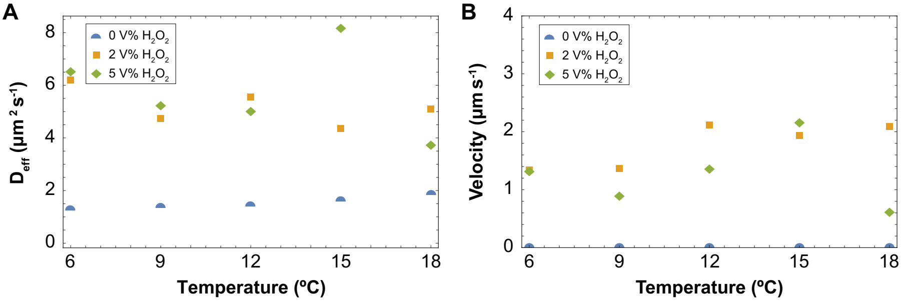

Appendix Figure 8.6: Single-particle behaviour of active superballs below room temperature. (a) Effective diffusion coefficient for Pt-coated cubic colloids at 0V%, 2V% and 5V% H_2O_2 concentrations in water and as a function of temperature. (b) Speed determined in the limit of $t \ll \tau$ for active superballs at 2V% and 5V% H_2O_2 concentrations in water and as a function of temperature. Speed in absence of H_2O_2 is set to 0.

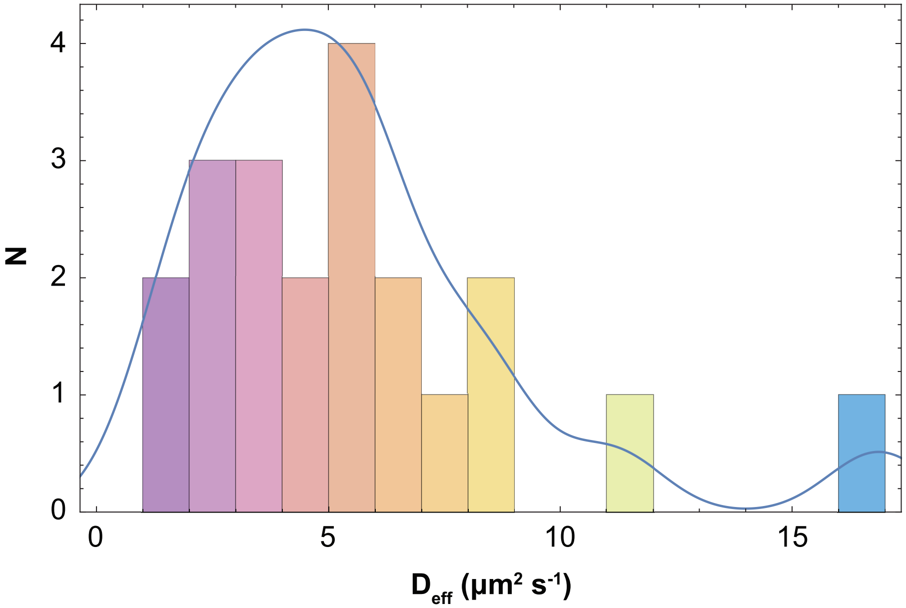

Appendix Figure 8.7: Distribution in effective diffusion coefficient. Histogram of D_{eff} at $T = 12°\text{C}$ and 2V% H_2O_2 concentration in water.

References

1. J. R. Howse, R. A. L. Jones, A. J. Ryan, T. Gough, R. Vafabakhsh & R. Golestanian. Self-motile colloidal particles: From directed propulsion to random walk, *Phys. Rev. Lett.* **2007**, *99*, 048102.
2. S. J. Ebbens & J. R. Howse. In pursuit of propulsion at the nanoscale, *Soft Matter* **2010**, *6*, 726–738.
3. T. Qiu, T. Lee, A. G. Mark, K. I. Morozov, R. Münster, O. Mierka, S. Turek, A. M. Leshansky & P. Fischer. Swimming by reciprocal motion at low Reynolds number, *Nat. Commun.* **2014**, *5*, 5119.
4. E. M. Purcell. Life at low Reynolds number, *Am. J. Phys.* **1977**, *45*, 3–11.
5. L. Baraban, M. Tasinkevych, M. N. Popescu, S. Sanchez, S. Dietrich & O. G. Schmidt. Transport of cargo by catalytic Janus micro-motors, *Soft Matter* **2012**, *8*, 48–52.
6. J. G. Gibbs & Y.-P. Zhao. Autonomously motile catalytic nanomotors by bubble propulsion, *Appl. Phys. Lett.* **2009**, *94*, 163104.
7. H. Ke, S. Ye, R. L. Carroll & K. Showalter. Motion analysis of self-propelled Pt-silica particles in hydrogen peroxide solutions, *J. Phys. Chem. A* **2010**, *114*, 5462–5467.
8. L. Baraban, D. Makarov, R. Streubel, I. Mönch, D. Grimm & O. G. Schmidt. Catalytic Janus motors on microfluidic chip: Deterministic motion for targeted cargo delivery, *ACS Nano* **2012**, *6*, 3383–3389.
9. L. Baraban, R. Streubel, D. Makarov, L. Han, D. Karnaushenko, O. G. Schmidt & G. Cuniberti. Fuel-free locomotion of Janus motors: Magnetically induced thermophoresis, *ACS Nano* **2013**, *7*, 1360–1367.
10. J. Palacci, S. Sacanna, A. P. Steinberg, D. J. Pine & P. M. Chaikin. Living crystals of light-activated colloidal surfers, *Science* **2013**, *339*, 936–940.
11. R. Dreyfus, J. Baudry, M. L. Roper, M. Fermigier, H. A. Stone & J. Bibette. Microscopic artificial swimmers, *Nature* **2005**, *437*, 862–865.
12. W. F. Paxton, K. C. Kistler, C. C. Olmeda, A. Sen, S. K. St. Angelo, Y. Cao, T. E. Mallouk, P. Lammert & V. H. Crespi. Catalytic nanomotors: Autonomous movement of striped nanorods, *J. Am. Chem. Soc.* **2004**, *126*, 13424–13431.
13. S. Fourier-Bidoz, A. C. Arsenault, I. Manners & G. A. Ozin. Synthetic self-propelled nanorotors, *Chem. Comm.* **2005**, 441–443.

14. L. F. Valadares, Y. Tao, N. S. Zacharia, V. Kitaev, F. Galembeck, R. Kapral & G. A. Ozin. Catalytic nanomotors: Self-propelled sphere dimers, *Small* **2010**, *6*, 565–572.
15. S. I. R. Castillo. *Cubic Colloids: Synthesis, Functionalization and Applications*, Utrecht University, **2015**.
16. T. Sugimoto & K. Sakata. Preparation of monodisperse pseudocubic α-Fe_2O_3 particles from condensed ferric hydroxide gel, *J. Colloid Interface Sci.* **1992**, *152*, 587–590.
17. R. Micheletto, H. Fukuda & M. Ohtsu. A simple method for the production of a two-dimensional, ordered array of small latex particles, *Langmuir* **1995**, *11*, 3333–3336.
18. J. C. Crocker & D. G. Grier. Methods of digital video microscopy for colloidal studies, *J. Colloid Interface Sci.* **1996**, *179*, 298–310.
19. R. Tuinier & T.-H. Fan. Unpublished results, **2018**.
20. J. Happel & H. Brenner. *Low Reynolds Number Hydrodynamics*, Springer Netherlands, **1983**.
21. S. Michelin, E. Lauga & D. Bartolo. Spontaneous autophoretic motion of isotropic particles, *Phys. of Fluids* **2013**, *25*, 061701.

Summary

Chirality is a geometric property of objects the mirror image of which cannot be brought to coincide with the original. Whereas some properties, such as evaporation temperature and colour, of left- and right-handed molecules are identical, other chemical, biological and optical properties are not. The absence of mirror symmetry leads to captivating effects such as the coupling of translational and rotational degrees of freedom and chiral liquid crystal formation. Unfortunately, it is not feasible to visualize the effects of chirality on the molecular level. Therefore, we investigated preparation routes for chiral colloids which, just as molecules, display thermal diffusion but with the crucial advantage that they can be imaged with optical microscopy.

Two methods were employed to synthesize chiral colloids from isotropic spheres. The first method relies on the confinement of colloidal spheres in hollow microtubes. Microtubes self-assemble from sugar and surfactant molecules as characterized *in situ* with high resolution small-angle x-ray scattering spanning more than three orders of magnitude of spatial scales (Chapter 2). The tubular microstructures consist of equally spaced curved bilayers forming a collection of concentric hollow cylinders with a pore diameter of roughly one micrometre. By adding colloidal spheres to the microtubes, colloid-in-tube assemblies are obtained. Depending on the colloid-to-tube diameter ratio, various structures are formed. Upon removing the microtubes these structures fall apart. Therefore, photo-responsive polystyrene colloids were developed that can photo-crosslink triggered by UV-light (Chapter 3). These coumarin-modified spheres form covalent bonds holding the spheres in place even after dissolution of the microtubes. Aqueous suspensions with bulk quantities of a library of ordered structures, including helical sphere chains, have eventually become available (Chapter 5). The colloidal equivalents of chiral molecules were used to study their Brownian dynamics (Chapter 7).

The second preparation route for chiral colloids combines dipolar hard spheres and depletion interaction. Superparamagnetic silica spheres were grafted with polymer

hairs and end-functionalized with coumarin molecules. In an external magnetic field, these spheres align while forming linear sphere chains. Upon UV-irradiation, permanent magnetisable sphere chains in bulk are obtained (Chapter 4). When a magnetic field is applied in the presence of depletion polymer, the linear sphere chains wind around each other transforming into helical chains (Chapter 6). The number of neighbours is maximized in a helical configuration compared to a linear one, lowering the energy of the system. The application of a homogeneous field appeared to be crucial leading to the development of a Helmholtz cube.

The final Part of this Thesis describes the realization of cubic microswimmers (Chapter 8). Superball-shaped colloids were coated with platinum that catalyses the decomposition of hydrogen peroxide into water and oxygen propelling the colloids via self-diffusiophoresis. The speed of the active particles increases with both fuel concentration and temperature. At short times the particles undergo directed motion, whereas at longer times a random walk with an enhanced diffusion coefficient is observed.

Samenvatting

Het doel van het leeuwendeel van dit Proefschrift (Deel I, II en III) is de ontwikkeling van een modelsysteem van chirale colloïden, dat geschikt is voor het bestuderen van de effecten van microscopische chiraliteit.

Colloïden

Colloïden zijn deeltjes tussen atomische en macroscopische dimensies in, met karakteristieke groottes van ongeveer 0.000001 tot 0.001 millimeter. De colloïden die in dit Proefschrift aan de orde komen, hebben een grootte van 0.5 micrometer (0.0005 millimeter) en zijn daarmee ongeveer honderd keer kleiner dan een haar of een korrel zand (zie Figuur A). Voorbeelden van colloïdale systemen zijn melk, inkt en ijs. Het grote voordeel van colloïden is dat ze zich gedragen als moleculen. Maar in tegenstelling tot moleculen zijn ze groot genoeg om te kunnen observeren met microscopen. Het zijn dus ideale modelsystemen om de moleculaire wereld na te bootsen. Colloïden vertonen, net als moleculen, zogenaamde Brownse beweging; de onregelmatige, thermische beweging van microscopische deeltjes. Wanneer je een colloïdaal systeem onder de microscoop bekijkt, zie je deze microscopische deeltjes heen en weer dansen, maar ze leven niet.

Chiraliteit

Een object is chiraal wanneer het spiegelbeeld niet in overeenstemming met het origineel gebracht kan worden. Het woord chiraliteit is afgeleid van het Griekse woord χειρ wat ‘hand’ betekent en dat is, samen met de DNA-helix, het meest bekende voorbeeld van een chiraal object (zie Figuur B). Sommige eigenschappen van onze linker- en rechterhand zijn gelijk, terwijl andere verschillen. Zo past een rechterhand niet in een linkerhandschoen en kan een linkshandige niet goed overweg met een rechtshandige schaar. Daarentegen kunnen we met beide handen objecten optillen of zwaaien naar iemand. Dit geldt ook voor atomen of moleculen, de bouwstenen van

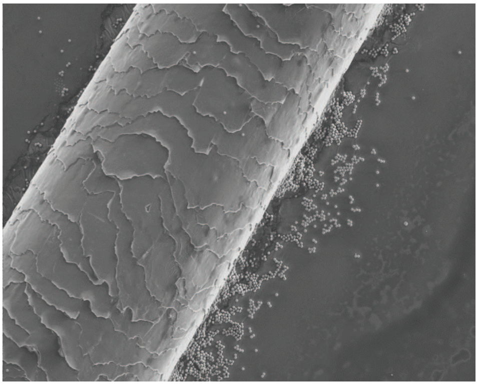

Figuur A: Een microscopie foto van een haar naast enkele colloïden. De colloïdale deeltjes zijn vele malen kleiner dan de dikte van een haar. Met dank aan dr. Ben Erné voor de haar en Hans Meeldijk voor het nemen van de foto.

alle materie, die chiraal zijn. Hoewel de fysische eigenschappen zoals het kookpunt en de kleur van links- en rechtshandige moleculen identiek zijn, heeft de links- of rechtshandigheid van een molecuul invloed op de geur, sterkte en giftigheid. Een voorbeeld: de linkshandige variant van het molecuul limoneen is verantwoordelijk voor de karakteristieke geur van sinaasappels, terwijl de rechtshandige variant naar citroenen ruikt. Helaas is het niet mogelijk om de effecten van chiraliteit op de moleculaire schaal te visualiseren omdat moleculen en atomen te klein zijn om te kunnen observeren. Daarom hebben we methoden onderzocht om chirale colloïden te maken, die, net als moleculen, thermische beweging laten zien maar het cruciale voordeel hebben dat ze met microscopie gevolgd kunnen worden.

Twee methoden zijn toegepast om chirale colloïden te maken van bolvormige deeltjes. De eerste methode maakt gebruik van het feit dat dichtgepakte bollen helische structuren kunnen vormen wanneer deze zich in een cilindrische omgeving bevinden. Dit kan in de praktijk makkelijk worden gevisualiseerd door een lang glas of een maatcilinder te vullen met knikkers van de juiste grootte. Op microscopische schaal hebben wij dit gerealiseerd door colloïden in holle microbuisjes te assembleren. Microbuisjes worden spontaan gevormd door een mengsel van suiker- en zeepmoleculen in water te verwarmen en vervolgens af te koelen tot kamertemperatuur. De buisjes bestaan uit meerdere gekromde lagen op evenredige afstand van elkaar die een collectie van evenwijdige cilinders vormen met een diameter van ongeveer een micrometer (Hoofdstuk 2). Door colloïdale bollen toe te voegen aan de buisjes

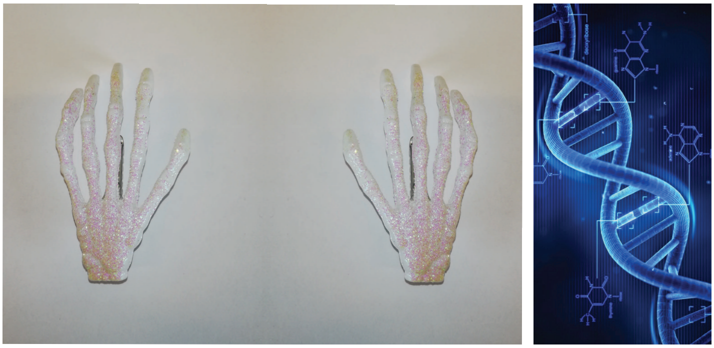

Figuur B: Links: handen zijn chiraal want een linker- en een rechterhand zijn spiegelbeelden van elkaar. Op de foto zijn twee haarclips in de vorm van de handen van een skelet te zien. Met dank aan Sandrine Heijnen. Rechts: de DNA-helix, een chiraal molecuul.

worden de colloïden in de buisjes opgesloten. Afhankelijk van de grootte van de colloïden worden verschillende structuren verkregen. Zo vormen bollen die even groot zijn als de diameter van de buisjes lineaire ketens. Maar de interessantste structuren worden gevormd door deeltjes die ongeveer half zo groot zijn als de diameter van de buisjes; deze vormen namelijk, onder andere, helische structuren. Zodra de buisjes worden verwijderd (door ze op te lossen in een overmaat water), vallen de gevormde structuren echter uit elkaar. Daarom hebben wij een soort chemische lijm aangebracht op het oppervlak van de deeltjes (Hoofdstuk 3). Na belichting met UV-licht wordt de lijm hard en blijven de bollen aan elkaar geplakt. Wanneer we de buisjes dan weghalen, blijven de gevormde structuren behouden en blijft er een scala aan verschillende structuren over in water (zie Figuur C). Op deze manier zijn grote hoeveelheden geordende structuren, waaronder helische ketens van bollen, beschikbaar geworden (Hoofdstuk 5). Deze colloïdale equivalenten van chirale moleculen zijn gebruikt om hun Brownse beweging te bestuderen (Hoofdstuk 7).

De tweede methode voor de bereiding van chirale colloïden maakt gebruik van magnetische bolvormige deeltjes in een magneetveld. Magnetische deeltjes lijnen zich uit in de richting van een extern magneetveld, dit kan bijvoorbeeld door permanente magneten in de buurt te plaatsen. Op het moment dat de magneten worden verwijderd, vallen de lineaire ketens uit elkaar. Ook deze magnetische bollen hebben wij dus met chemische lijm uitgerust, om permanente magnetische ketens van bollen te krijgen, zodra deze ketens met UV-licht worden beschenen (Hoofdstuk 4). Wanneer kleinere (niet-magnetische) deeltjes worden toegevoegd aan de magnetische

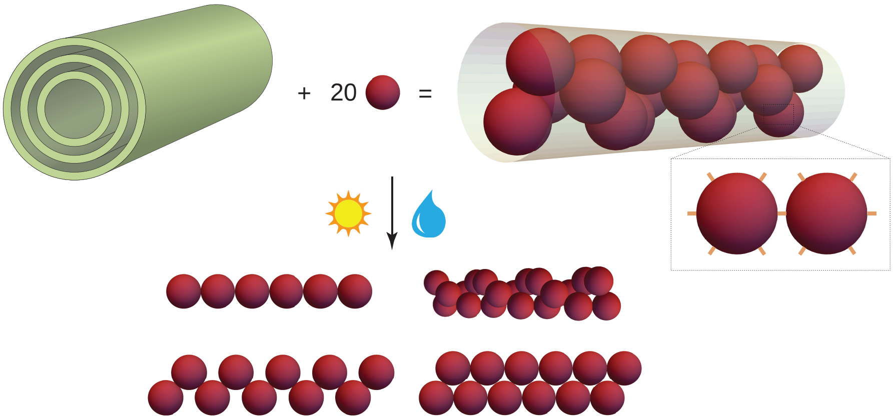

Figuur C: Microbuisjes bestaan uit meerdere cilinders op evenwijdige afstand van elkaar. In de holte/porie van de microbuisjes kunnen colloïdale bollen plaatsnemen. De colloïden zijn gefunctionaliseerd met een soort lijm (oranje rechthoeken). Wanneer de bollen in de microbuisjes met UV-licht worden beschenen, blijven de bollen aan elkaar plakken nadat de buisjes zijn verwijderd. Afhankelijk van de grootte van de bollen, kunnen verschillende structuren worden gevormd waaronder helische ketens.

bollen arrangeren de bolvormige deeltjes zich in chirale ketens. Dit is gunstig omdat de kleinere deeltjes zo meer bewegingsruimte krijgen. Een analoog voorbeeld is een feest in een restaurant. Wanneer er een zittend diner wordt gehouden in een restaurant, staan de tafels op een bepaalde manier opgesteld en kunnen 25 mensen dineren, zie Figuur D. Wanneer er echter een walking dinner of een feest plaatsvindt, dan passen er meer mensen in de dinerruimte wanneer de tafels tegen elkaar en naar de wand worden geschoven. De gasten hebben dan meer bewegingsruimte en hoeven niet te dicht op elkaar te staan. Ditzelfde gebeurt in ons systeem met grotere magnetische deeltjes en kleinere deeltjes. De kleinere deeltjes (de mensen in het restaurantvoorbeeld) duwen de grotere deeltjes (de tafels) dichter tegen elkaar aan opdat de kleinere deeltjes meer bewegingsvrijheid hebben. Wanneer er voldoende kleinere deeltjes aanwezig zijn, zullen de grotere deeltjes zich dus liever in een helixvorm organiseren dan in een lineaire keten. Hiervan hebben wij gebruik gemaakt om chirale colloïden te maken (Hoofdstuk 6). Wanneer er dus een magneetveld wordt aangelegd in de aanwezigheid van kleinere niet-magnetische deeltjes, winden de lineaire ketens zich om elkaar heen en transformeren zo in helische ketens (zie Figuur E).

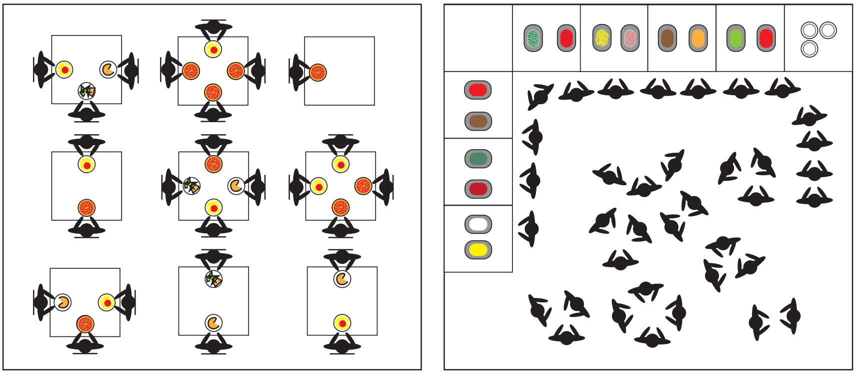

Figuur D: 25 gasten kunnen plaatsnemen in een restaurant op een doordeweekse dag (links). In het weekend houdt het restaurant feestjes waarbij ze de tafels aan de kant schuiven opdat meer gasten aanwezig kunnen zijn en ze nog voldoende bewegingsruimte houden (rechts). Met dank aan Sandrine Heijnen voor het maken van deze tekening. Naar: Remco Tuinier en Henk Lekkerkerker in *Colloids and the Depletion Interaction*, Springer Nederland, 2011.

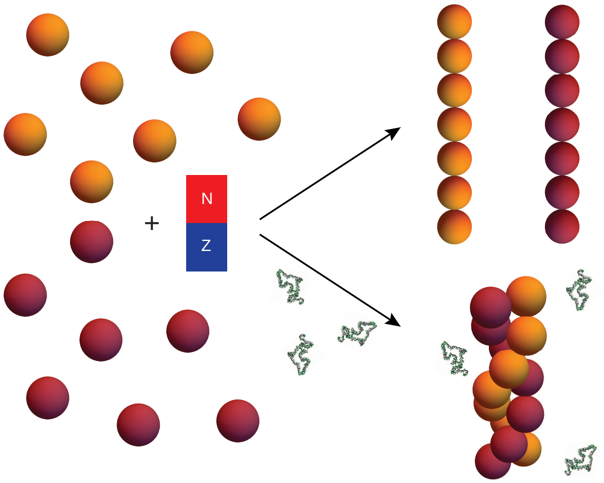

Figuur E: Magnetische bollen vormen lineaire ketens wanneer een magneetveld wordt aangelegd. Hier wordt een magneetveld gecreëerd door een permanente magneet. In de aanwezigheid van kleinere deeltjes (polymeerketens in dit geval) wordt juist een helische keten gevormd.

Actieve Materie

Tot slot hebben we de realisatie van kubische microzwemmers beschreven (Deel IV, Hoofdstuk 8). Alhoewel colloïden vanuit zichzelf bewegen vanwege thermische fluctuaties, blijft Brownse beweging een vorm van passieve beweging aangezien de deeltjes zelf geen actieve rol in hun beweging hebben. Auto's, vogels en mensen vertonen daarentegen actieve beweging; energie wordt verbruikt uit de omgeving (voedsel voor mensen en vogels of benzine voor auto's) en deze wordt omgezet in bewegingsenergie (lopen, vliegen of rijden). Actieve deeltjes op microscopische schaal hebben wij gerealiseerd door colloïden in de vorm van een kubus (superballs genaamd) aan één kant met platina te bedekken. Platina is een katalysator die de afbraak van het molecuul waterstofperoxide in water en zuurstof versnelt. Twee moleculen waterstofperoxide worden omgezet in drie moleculen water en zuurstof. De grotere hoeveelheid moleculen die door deze chemische reactie aan het oppervlak wordt geproduceerd, stuwt de kubus voort waarna deze actieve beweging laat zien. Deze kubusvormige deeltjes kunnen hol gemaakt worden en in de holte kan een of andere vracht geplaatst worden. Op deze manier kan een microscopische variant van een auto gemaakt worden, die vracht kan transporteren van de ene naar de andere plek (zie Figuur F).

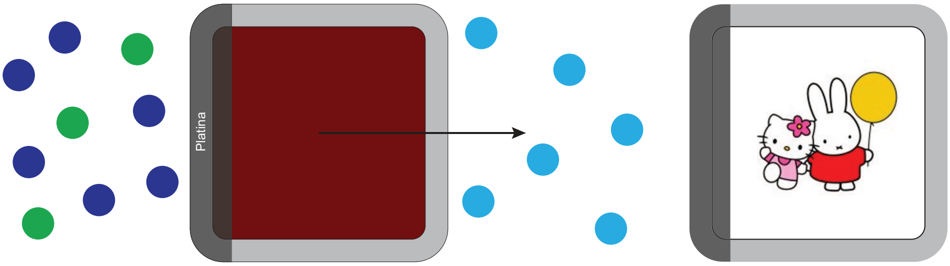

Figuur F: Een kubusvormig colloïdaal deeltje is deels bedekt met platina. Platina zet de 6 lichtblauwe bollen (waterstofperoxide) om in 6 blauwpaarse bollen (water) en 3 groene bollen (zuurstof). Doordat er nu meer bollen aan de platinakant aanwezig zijn, wordt het deeltje vooruit gestuwd. De donkerrode kern (ijzeroxide, roest) kan uit de kubus verwijderd en in plaats daarvan kan vracht vervoerd worden (in dit geval Nijntje en Hello Kitty).

Dankwoord / Acknowledgements

Het is een cliché, maar die zijn vaak waar. Dit Proefschrift zou niet tot stand zijn gekomen zonder de steun en hulp van veel mensen. Daarom wil ik de tijd nemen om iedereen die een bijdrage heeft geleverd, op een wetenschappelijk of persoonlijk vlak, te bedanken. Te beginnen met mijn begeleiders.

Andrei, bedankt voor je interesse, je betrokkenheid, je kinderlijke enthousiasme en je oneindige nieuwsgierigheid. Je bent altijd vrolijk, zit vol anekdotes ('Moeder Natuur' is een gouwe ouwe), gezelligheid en snoepjes. Op de ESRF in Grenoble ben je helemaal in je element en het is geweldig om te zien hoeveel jij weet over SAXS; je bent niet voor niets de SAXS-man. Ook wil ik jou en Anna bedanken voor jullie gastvrijheid en het verwelkomen van mij in jullie huis in Oxford.

Albert, ik heb jou in mijn eerste jaar als student al ontmoet aangezien jij mijn gewezen tutor was. Was je dat niet geweest, dan was ik waarschijnlijk gestopt met de studie scheikunde en nooit gepromoveerd. Bedankt voor je vertrouwen in mij, je steun en je oprechte interesse. Je nam mij altijd serieus zelfs als ik een situatie misschien iets te hoog opnam en hielp mij met het oplossen van problemen die mij soms te groot leken.

Ik had mij werkelijk geen betere begeleiders kunnen wensen. Bedankt voor alles. Voor de vrijheid die jullie mij gegeven hebben om te onderzoeken wat ik leuk en belangrijk vond, voor de vele conferenties die ik heb mogen bezoeken (zelfs in Singapore) en voor de periode dat ik in Oxford heb mogen verblijven. Het feit dat jullie deur altijd open staat voor mij en dat jullie de tijd voor me nemen.

Merci beaucoup pour tout, Kanvaly! Bedankt voor het synthetiseren van coumarin, voor de samenwerking op meerdere (uitdagende) projecten, voor het altijd klaarstaan met hulp en advies en voor je kennis van het lab waardoor je altijd antwoord had op de vraag 'waar vind ik ...?' Ook bedankt voor de vele leuke gesprekken, pauzes en lunches samen, kortom de gezelligheid. Ik wil ook Miriam bedanken voor haar prachtige briefje over haarzelf. Bas, bedankt dat je me hebt geïntroduceerd tot de wondere wereld van ATRP. Helaas werkte je met polystyreen en niet met silica, maar daar heb ik op een later moment verandering in kunnen brengen. Ik ben je misschien wel het meest dankbaar voor het prachtige huisje in Bunnik waar ik jaren met plezier heb gewoond. Bonny, hartelijk dank voor het creëren van de Helmholtz-kubus en dat je altijd bereid was om er weer eens iets aan te veranderen. En voor alle andere, vele verzoeken die je over de jaren hebt ingewilligd.

Chrisje, hartelijk dank voor het LaTeX template van je proefschrift. Deze was veel te ingewikkeld voor mij, maar ik heb eruit gehaald wat ik begreep en nodig had. Zonder jouw template zou mijn Thesis er niet zo mooi uit zien. Ook bedankt voor alle hulp met de optische microscopen. Álvaro, thanks for patiently helping me with any questions regarding Mathematica or LaTeX and discussions about theory and whatever came to mind. I really enjoyed the conferences that we attended together. Every day you spent at FCC was a fun day, even with your scary goat sounds. Jasper, bedankt voor de illustratie van de microtubes en voor je hulp met Illustrator en Mathematica. Met jouw hulp is het gelukt om de vijfde kleur aan het kleurenschema van mijn Proefschrift toe te voegen. Heb je de panda al gevonden?

Bedankt voor de interesse die je hebt getoond in mij en mijn onderzoek, Remco. Het was erg leuk om met je samen te werken naast mijn promotieonderzoek. Ben, bedankt voor alle advies, zowel gevraagd als ongevraagd, aanmoediging en voor de leuke anekdotes. Ik wil mijn dorpsgenote Marina bedanken voor alle hulp met administratieve zaken en alle andere zaken waarvoor ik bij je heb aangeklopt. Op de labopruimdagen werd ik standaard als enige ingedeeld voor het schoonmaken van drie ruimten en daar wil jou hartelijk voor bedanken, Dominique. Maar serieus, het is verbazingwekkend hoe goed georganiseerd ons lab is en dat is grotendeels aan jou te danken.

Yong, thank you for all the gossip, the dinners, activities and more. Thank you also for starting a running club and making me run ('being tired is no excuse!') especially during my writing period. I still hate running but I enjoyed (almost) every run with you and the other members of the club (which still needs a name). Antara, thank you for keeping in touch and for all the advice you have given me. I hope we will manage to go on a beam trip together some day! Rumen/Rumi, thank you for the bike rides to Bunnik late at night after the pub quiz at the Basket, for help with Mathematica and for useful discussions.

I spend most of my time either in the lab or in my office. Therefore, I would like to thank my office mates for sharing N701 during my PhD: Sonja, Ping, Joeri, Nina and Neshat. Toen mij verteld werd dat ik mijn kantoor met een student moest delen (omdat de studentcoördinator van die tijd -dat was ikzelf- iets te enthousiast was met het aannemen van studenten), was ik daar in eerste instantie niet heel blij mee. Maar ik had mij geen leukere kantoorgenoot kunnen wensen Joeri, het was supergezellig! Het was heel fijn dat ik lab N729 met jou deelde, Pepijn, of misschien: juist niet deelde. Aangezien jij altijd de hort op was, had ik het lab vaak voor mijzelf. Bedankt voor de tracking code en (soms) nuttige discussies.

During my PhD I had the chance to supervise multiple students. Dennis, mijn eerste student en de enige die gewerkt heeft aan de zwemmende kubusjes oftewel het actieve gedeelte van mijn Proefschrift. Next was Carla who worked tirelessly on the synthesis of polystyrene with coumarin which gave us quite some headaches but some wonderful results in the end. Patrick heeft enthousiast gewerkt aan de magnetische silicabollen en heeft zelfs zijn eigen magneetjes gebruikt voor zijn onderzoek. Ik ben nog steeds onder de indruk van het prachtige essay dat je hebt geschreven, Florian, na afloop van je onderzoeksproject bij mij; maar misschien nog wel indrukwekkender is de hoeveelheid yoghurt die je elke dag at. Rebecca, thank you for the density gradient centrifugation experiments that you performed. Sandrine, jij hebt zowel je Bachelor als je Master Thesis bij mij volbracht en dit heeft geleid tot twee mooie hoofdstukken in mijn Proefschrift. Ik wil je ook bedanken voor het steeds opmerken van een fout aan het coumarin molecuul totdat ik dit eindelijk veranderde. Ook bedankt voor het suggereren van de kleur geel voor Hoofdstuk 1, waar ik in eerste instantie op tegen was. I would like to thank all of you for the contributions that you have made to this Thesis and for contributing to a nice atmosphere in the group.

I would like to thank all other former and current members of FCC for contributing to the nice atmosphere, coffee breaks, Tricolore Thursdays, New Year's dinners, etc. etc.: Alex, Burak, Faranaaz, Frans, Gert Jan, Hans, Henk, Jan, Janne-Mieke, Joost, Joren, Mark, Michele, prof. Vrij, Regina (bedankt voor de Milo!), Riande, Roel, Willem, Xiuhang and all the students including Alice, Charlie, Ellen, Hedera, Jolijn, Karina, Myrthe, Nathalie and Noah. I would like to thank the ~~Crystal~~ Candy Club and its members for useful discussions and for the very welcome candies on Tuesdays and later Fridays. Hans en Chris, heel erg bedankt voor jullie ondersteuning met de elektronenmicroscopen. Ik heb jullie nog nooit betrapt op een slecht humeur en jullie waren altijd bereid om mij te hulp te schieten.

I have had the pleasure of visiting the ESRF multiple times for SAXS measurements and I am very grateful to all the beamline scientists and staff in Grenoble who helped me in any way. In particular, I would like to thank Sylvain for the excellent support during my own beamtime at the beautiful ID02 beamline. I would like to thank Sankyo

Denki Co., Ltd. and especially Shin Matsumoto, for sending us a replacement UV lamp free of charge after ours broke. Almost four months of my PhD project were spent in the beautiful city of Oxford. I would like to thank the members of the Physical and Theoretical Chemistry Laboratory for making my stay worthwhile and enjoyable. In particular I would like to thank Balkis (dank je wel!), Louis, Han Sol, Josh, Muhammad, Taiki, Siyu, Ruth and Caitlin.

Nastasia, het ontwerp dat je hebt gemaakt voor mijn voorkant heeft al mijn verwachtingen overtroffen, ontzettend bedankt! Mijn Thesis ziet er in ieder geval mooi uit! Veel succes met je eigen promotie. Bedankt voor de pianolessen, Paul, en de leuke gesprekken. Ik had het erg naar mijn zin de avonden waar ik even iets heel anders deed en het over heel andere dingen had; het was een welkome afleiding.

It was a pleasure to meet you over the years at conferences, Tommy. Thank you so much for introducing me to so many people at conferences (as your former boss even!) and for helping me find the next step. I met you at my very first conference, Chiho, and again at many conferences after that. I hope to see you more in the future. My friends from Sweden and not Sweden any more: talking to and meeting with you always feels like coming home. I am very happy with such great friends even if you are a bit far away at the moment. Dat, Tiny, Jessie, Weimin, let's meet more often! I would also like to thank Marta for gifting me the iconic mug of Winnie the Pooh years ago when I left Lund; it really has become a symbol of me. Anna, thank you for all the dinners, movie nights and advice. Your realistic outlook on life and down to earth mentality was very helpful and necessary from time to time.

Many thanks to my paranymphs and dear friends Fuqiang and Nina. Thank you for immediately accepting the role of my paranymph and in Fuqiang's case also for offering to be my paranymph (lol). Fuqiang, we started our PhD more or less at the same time and we will finish more or less at the same time. I am very happy to have had you as my companion during these past four years. You were always there for me whether it was with help on scientific related topics or listening to me complain about the colours of my Thesis or the writing of the summary which according to you should not have taken me more than two days. Your childish enthusiasm and always positive attitude have helped me through many a rough patch. Good luck with your defence and I am honoured to be your paranymph. Nina, it is a pity that we did not overlap more at FCC and that you were only part-time at FCC. But I am happy that we have become such great friends and that I can talk to you about anything. Thank you for all the fun activities, especially our movie nights. Even though you have a weird taste in movies, I simply enjoy the time we spent together. I am very happy to see that you have found the job you love. To many more years together, even if I decide to move to a 'too cold' country.

Helaas heb ik afscheid moeten nemen van mijn oma en mijn opa in de afgelopen jaren. Lieve oma, ik vind het erg jammer dat je niet in persoon aanwezig kan zijn op mijn verdediging. Ik mis je telefoontjes, je geruststellende stem en je glimlach. Lieve opa, ik mis je verhalen en je grapjes; je bijnaam was ook niet voor niets *Bouhilaat*.

Dank je wel grote, kleine zus Majda voor het corrigeren van alle Nederlandse teksten in dit Proefschrift (fouten zijn dus ook aan jou voorbehouden). Ook erg bedankt voor het onbehulpzaam zijn wanneer ik weer op zoek was naar een nieuwe show op Netflix om te kijken. Dank je voor de geweldige gifjes die je me stuurde wanneer ik weer even in paniek raakte zo aan het einde van mijn promotie en voor je nuttige advies (soms...). Maar het meest dankbaar ben ik misschien nog wel voor Hello Kittymeisje.

Tot slot wil ik mijn ouders bedanken. Ongetwijfeld de belangrijkste personen in mijn leven en aan wie ik alles te danken heb. Mama en papa, papa en mama, zonder jullie ben ik nergens. Jullie hebben mij altijd gesteund, gemotiveerd en in mij geloofd. Het is onmogelijk om in woorden uit te drukken wat jullie voor mij betekenen en hoeveel jullie voor mij hebben gedaan. Jullie volgen mij overal, want wie heeft er nou ooit van Lund gehoord, hè mama? Papa, jij weet mij altijd aan het lachen te maken hoe slecht mijn dag of humeur ook was. Met name de laatste maanden waren niet makkelijk, voor geen van allen, maar met jullie aan mijn zijde weet ik dat ik alles aankan en dat alles goedkomt. Ik weet dat, waar ik ook terecht kom na mijn promotie, ik altijd op jullie kan rekenen. Het beste in mijn leven is dat ik jullie als mijn ouders heb en ik prijs mijzelf daarmee gelukkig.

Samia
November 2018

List of Publications

This Thesis is based on the following publications:

- S. Ouhajji, J. Landman, S. Prévost, L. Jiang, A. P. Philipse & A. V. Petukhov. *In situ* observation of self-assembly of sugars and surfactants from nanometres to microns. *Soft Matter* **2017**, *13*, 2421-2425 (Chapter 2).
- J. Landman, S. Ouhajji, S. Prévost, T. Narayanan, J. Groenewold, A. P. Philipse, W. K. Kegel & A. V. Petukhov. Inward growth by nucleation: Multiscale self-assembly of ordered membranes. *Science Advances* **2018**, *4*, eaat1817 (Chapter 2).
- S. Ouhajji, B. G. P. van Ravensteijn, C. Fernàndez-Rico, K. S. Lacina, A. P. Philipse & A. V. Petukhov. Wet-chemical synthesis of chiral colloids. *ACS Nano* accepted, DOI:10.1021/acsnano.8b05065 (Chapters 3 and 5).
- S. Heijnen, P. van Vliet, B. Kuipers, A. V. Petukhov, A. P. Philipse & S. Ouhajji. Rodlike and chiral chain formation of magnetic spheres. *In preparation* (Chapters 4 and 6).
- S. Ouhajji, L. Cortes, A. P. Philipse & A. V. Petukhov. Brownian motion of a colloidal helix. *In preparation* (Chapter 7).
- S. Ouhajji, D. van Eldik, R. Tuinier, T.-H. Fan, A. V. Petukhov & A. P. Philipse. Self-propelling superballs for cargo transport. *In preparation* (Chapter 8).

Other publications by the author:

- S. I. R. Castillo, S. Ouhajji, S. Fokker, B. H. Erné, C. T. W. M. Schneijdenberg, D. M. E. Thies-Weesie & A. P. Philipse. Silica cubes with tunable coating thickness and porosity: From hematite filled silica boxes to hollow silica bubbles. *Microporous and Mesoporous Materials* **2014**, *195*, 75-86.

- S. Ouhajji, T. Nylander, L. Piculell, R. Tuinier, P. Linse & A. P. Philipse. Depletion controlled surface deposition of uncharged colloidal spheres from stable bulk dispersions. *Soft Matter* **2016**, *12*, 3963-3971.
- R. Tuinier, S. Ouhajji & P. Linse. Phase behaviour of colloids plus weakly adhesive polymers. *The European Physical Journal E* **2016**, *39*, 115.
- J. M. Meijer, A. Pal, S. Ouhajji, H. N. W. Lekkerkerker, A. P. Philipse & A. V. Petukhov. Observation of solid–solid transitions in 3D crystals of colloidal superballs. *Nature Communications* **2017**, *8*, 14352.

About the Author

Samia Ouhajji was born on February 12th 1991 in Gorinchem, the Netherlands. In 2009 she graduated *cum laude* from the Gymnasium Camphusianum in Gorinchem. In the same year she started her Bachelor's Degree of Chemistry at the University of Utrecht which she obtained *cum laude* in 2012. During her Bachelor, she followed the Honours Minor Descartes College and wrote her Bachelor Thesis on magnetic inverted photonic crystals under supervision of Janne-Mieke Meijer and Dr. Andrei Petukhov at the Van 't Hoff Laboratory for Physical and Colloid Chemistry. The year of 2012-2013 she spent at the University of Lund in the Physical Chemistry group as part of her Master's research project, which was supervised by Prof. Albert Philipse (UU), Prof. Lennart Piculell and Prof. Tommy Nylander. Her Master Thesis was awarded the 2nd prize of the Graduate School of Natural Sciences Thesis Award. She obtained her Honours Master's Degree in Nanomaterials: Chemistry and Physics *cum laude* after a five-month research internship in the Computational Chemistry group at the University of Amsterdam under the supervision of Arthur Newton and Prof. Peter Bolhuis.

In 2014, she started her PhD project at the Van 't Hoff Laboratory for Physical and Colloid Chemistry, the results of which were described here. Her PhD project was supervised by Prof. Albert Philipse and Dr. Andrei Petukhov. During her PhD, she spent four months as a visiting scholar in the Physical and Theoretical Chemistry Laboratory at the University of Oxford. Furthermore, the author represented her group as the student coordinator, emergency response officer and Debye PhD committee member. Parts of this Thesis have been published in peer-reviewed scientific journals and have been presented at both national and international conferences. Conferences where the author has presented her work include the ECIS in Bordeaux (2015), Soft Matter in Grenoble (2016), UKColloids in Manchester (2017) and Designer Soft Matter in Singapore (2018).